

## CHARACTERIZING THE CIRCUMGALACTIC MEDIUM OF NEARBY GALAXIES WITH *HST*/COS AND *HST*/STIS ABSORPTION-LINE SPECTROSCOPY: II. METHODS AND MODELS<sup>1</sup>

BRIAN A. KEENEY<sup>2</sup>, JOHN T. STOCKE<sup>2</sup>, CHARLES W. DANFORTH<sup>2</sup>, J. MICHAEL SHULL<sup>2</sup>, CAMERON T. PRATT<sup>2</sup>, CYNTHIA S. FRONING<sup>3</sup>, JAMES C. GREEN<sup>2</sup>, STEVEN V. PENTON<sup>4</sup>, BLAIR D. SAVAGE<sup>5</sup>

<sup>1</sup>Based on observations with the NASA/ESA *Hubble Space Telescope*, obtained at the Space Telescope Science Institute, which is operated by AURA, Inc., under NASA contract NAS 5-26555.

<sup>2</sup>Center for Astrophysics and Space Astronomy, Department of Astrophysical and Planetary Sciences, University of Colorado, 389 UCB, Boulder, CO 80309, USA

<sup>3</sup>Department of Astronomy, University of Texas at Austin, Austin, TX 78712, USA

<sup>4</sup>Space Telescope Science Institute, Baltimore, MD 21218, USA

<sup>5</sup>Department of Astronomy, University of Wisconsin, Madison, WI 53706, USA

### ABSTRACT

We present basic data and modeling for a survey of the cool, photo-ionized Circum-Galactic Medium (CGM) of low-redshift galaxies using far-UV QSO absorption line probes. This survey consists of “targeted” and “serendipitous” CGM subsamples, originally described in [Stocke et al. \(2013, Paper 1\)](#). The targeted subsample probes low-luminosity, late-type galaxies at  $z < 0.02$  with small impact parameters ( $\langle \rho \rangle = 71$  kpc), and the serendipitous subsample probes higher luminosity galaxies at  $z \lesssim 0.2$  with larger impact parameters ( $\langle \rho \rangle = 222$  kpc). *HST* and *FUSE* UV spectroscopy of the absorbers and basic data for the associated galaxies, derived from ground-based imaging and spectroscopy, are presented. We find broad agreement with the COS-Halos results, but our sample shows no evidence for changing ionization parameter or hydrogen density with distance from the CGM host galaxy, probably because the COS-Halos survey probes the CGM at smaller impact parameters. We find at least two passive galaxies with H I and metal-line absorption, confirming the intriguing COS-Halos result that galaxies sometimes have cool gas halos despite no on-going star formation. Using a new methodology for fitting H I absorption complexes, we confirm the CGM cool gas mass of Paper 1, but this value is significantly smaller than found by the COS-Halos survey. We trace much of this difference to the specific values of the low- $z$  meta-galactic ionization rate assumed. After accounting for this difference, a best-value for the CGM cool gas mass is found by combining the results of both surveys to obtain  $\log(M/M_{\odot}) = 10.5 \pm 0.3$ , or  $\sim 30\%$  of the total baryon reservoir of an  $L \geq L^*$ , star-forming galaxy.

**Keywords:** galaxies: dwarf — galaxies: groups: general — galaxies: halos — galaxies: spiral — intergalactic medium — quasars: absorption lines

### 1. INTRODUCTION

A detailed knowledge of the Circumgalactic Medium (CGM; a.k.a gaseous galaxy halo) is necessary for any detailed understanding of galaxy formation and evolution. While significant advances have been made to detect and characterize the CGM at high- $z$  (e.g., [Steidel 1995](#); [Adelberger et al. 2005](#); [Rudie et al. 2013](#)), the advent of low redshift studies using the ultraviolet spectrographs of the *Hubble Space Telescope* (*HST*) has proven critical to recent advances in the field ([Tripp, Lu, & Savage 1998](#); [Penton, Stocke, & Shull 2004](#); [Tumlinson et al. 2011](#); [Prochaska et al. 2011a](#); [Stocke et al. 2013](#); [Werk et al. 2013](#); [Lehner et al. 2015](#); [Bowen et al. 2016](#); [Werk et al. 2016](#)), including the recognition that the CGM likely contains a comparable number of baryons as found in all the stars and gas in the disks of late-type galaxies ([Tumlinson et al. 2011](#); [Stocke et al. 2013](#); [Werk et al. 2014](#)). The theoretical case for the importance of a massive CGM is demonstrated by the continuing high star formation rate (SFR) in spiral galaxies ([Binney & Tremaine](#)

[1987](#); [Chomiuk & Povich 2011](#)), the detailed metallicity history of galaxies (e.g., the “G dwarf problem”; [Larson 1972](#); [Binney & Tremaine 1987](#); [Chiappini, Matteucci & Romano 2001](#)), and the substantial deficiency of detected baryons in spiral galaxies relative to the cosmic ratio of baryons to dark matter (e.g., [McGaugh et al. 2000](#); [Klypin et al. 2001](#)). Each of these observational problems requires a CGM baryonic mass at least as great as the total amount in the galaxy’s disk.

While the emission measure of this gas is too low to provide direct imaging detections at the present time (although see [Donahue, Aldering, & Stocke 1995](#); [Martin et al. 2015](#); [Fumagalli et al. 2017](#)), it is possible to use background, UV-bright AGN to detect and probe the full extent of the CGM in absorption in both the Milky Way and in other galaxies. In our own Galaxy’s halo, the discovery of highly-ionized high-velocity-clouds (HVCs) ([Sembach et al. 1995, 2003](#); [Collins, Shull, & Giroux 2004](#)) using UV spectroscopy of metal ions such as Si III, C IV, and O VI has revealed a much larger reservoir of infalling gas ([Shull et al. 2009](#); [Collins, Shull, & Giroux 2009](#)) than the H I 21-cm HVCs. But only

in some cases (Lehner & Howk 2011) can the distance to these highly-ionized HVCs be determined, allowing their total mass to be estimated. Nevertheless, the mass infall rate ( $\sim 1 M_{\odot} \text{ yr}^{-1}$ ) estimated by Shull et al. (2009) is sufficient to fuel much of the on-going Milky Way SFR ( $2\text{-}4 M_{\odot} \text{ yr}^{-1}$ ; Diehl et al. 2006; Robitaille & Whitney 2010; Shull et al. 2011). The detection of high-covering-factor, photo-ionized gas clouds in the CGM of low- $z$  star-forming galaxies (Werk et al. 2014; Stocke et al. 2013) suggests that galactic “fountains” of recycling gas (i.e., what has come to be called the “baryon cycle”), together with lower metallicity gas from extra-galactic sources (e.g., dwarf galaxy satellites; Stocke et al. 2013, or the Inter-Galactic Medium; IGM; Bowen et al. 2016), is essential for the continued high star formation rate in late-type galaxies. The possibility that these cool<sup>1</sup>, photo-ionized clouds are embedded in a hotter ( $T \sim 10^6$  K), more massive diffuse gas also has been postulated based on high signal-to-noise (S/N) O VI and Ly $\alpha$  absorption-line detections (Stocke et al. 2014; Pachat et al. 2016).

In this paper we present the basic data used for a recent CGM study (Stocke et al. 2013, Paper 1 hereafter). These data include far-UV spectroscopy obtained with *HST*’s Space Telescope Imaging Spectrograph (STIS) and Cosmic Origins Spectrograph (COS), which were used to probe the CGM of low redshift galaxies using both “serendipitous” and “targeted” observations. While we measure and catalog high ionization lines like the N V and O VI doublets, these absorptions are not used in our analysis herein; detailed discussion of O VI in particular can be found in Savage et al. (2014), Stocke et al. (2014), and Werk et al. (2016).

Deep H $\alpha$  imaging and/or long-slit spectroscopy of the targeted and serendipitous galaxies is also presented, and used to obtain the on-going ( $\leq 10^7$  yr) star formation rates (SFR). Near-UV photometry of these same galaxies using the *Galaxy Evolution Explorer* (GALEX) satellite provides a more comprehensive, recent SFR over a longer time frame ( $\sim 10^8$  yr), and is presented where available. Galaxy metallicities have been estimated using H II region emission lines and/or Lick absorption-line indices.

The ultraviolet spectroscopy presented herein forms the basis for many of the conclusions drawn by Paper 1, including the Ly $\alpha$  covering factors (approaching 100% inside the nearest galaxy’s virial radius) as well as cloud thicknesses (0.1 to 30 kpc) and masses ( $10\text{-}10^8 M_{\odot}$  range). A more recent study (Davis et al. 2015) of common absorptions along adjacent sight lines through a foreground galaxy halo confirms large sizes and masses for at least some CGM absorbing clouds. The size, mass and pressure results presented in Paper 1 were obtained using homogeneous, single-phase CLOUDY photo-ionization models (Ferland et al. 1998); these models are also presented and updated herein.

<sup>1</sup> The temperature nomenclature followed in this paper is that routinely used in recent observational and theoretical papers on the CGM; i.e., “cool” refers to  $T \sim 10^4$  K absorbers in photo-ionization equilibrium, “warm” refers to collisionally ionized absorbers at  $T \sim 10^5\text{-}10^{6.5}$  K and “hot” gas is at  $T > 10^{6.5}$  K. Thus, the warm gas referenced in Galactic studies of the interstellar medium is termed “cool” herein.

Section 2 contains a brief rediscussion of the target selection and the data analysis procedure for the COS, STIS and *FUSE* spectra. Since both these topics have been covered in depth in Paper 1, Danforth et al. (2016), Tilton et al. (2012) and Keeney et al. (2014), the discussion herein will be largely a summary of the description in those previous papers. Section 3 presents the COS spectroscopy of the absorption systems used in this study. Section 4 presents the basic galaxy data obtained for both samples using ground-based imaging and spectroscopy, primarily obtained at the Apache Point Observatory’s 3.5m telescope (APO hereafter) operated by the Astrophysical Research Corporation (ARC), as well as SDSS galaxy survey data obtained publicly through DR12 (Alam et al. 2015). Our photo-ionization models are presented in Section 5, and Section 6 presents an updated cool CGM gas mass calculation that confirms the results of Paper 1, along with a comparison to similar calculations made using the COS-Halos results (Werk et al. 2014; Stern et al. 2016; Prochaska et al. 2017). The discussion of results in Section 7 includes absorber/galaxy correlations based on basic observables, including statistics of metal-bearing and metal-free absorbers, absorber kinematics relative to the associated galaxy, and absorber/galaxy metallicity and star formation rate comparisons. Section 7 also includes investigations into the robustness of the galaxy associations and whether early-type galaxies are associated with low- $z$  Ly $\alpha$  absorption. Section 8 summarizes the findings of this paper. The Appendices contain comments on individual absorption-line fits, galaxy measurements, and photo-ionization models (Appendix A), as well as the ground-based images of targeted and serendipitous galaxies (Appendix B).

Throughout this paper, we assume WMAP9 values (Hinshaw et al. 2013) of the standard cosmological parameters:  $H_0 = 69.7 \text{ km s}^{-1} \text{ Mpc}^{-1}$ ,  $\Omega_{\Lambda} = 0.718$ , and  $\Omega_{\text{m}} = 0.282$ .

## 2. SAMPLE SELECTION

The philosophy behind the sample selection for the COS Science Team (hereafter called Guaranteed Time Observers, or GTOs) QSO/galaxy pairs program was to select very low-redshift ( $z \leq 0.02$ ), low-luminosity spiral and irregular foreground galaxies at low impact parameters ( $\rho \leq 1.5 R_{\text{vir}}$ ) to bright ( $V \leq 17.5$ ) background QSOs, chosen from a large list of potential targets. The COS GTO Team then conducted a modest-sized COS survey of the CGM of these very nearby, late-type galaxies (10 sight lines and 12 foreground galaxy CGMs probed) by observing these bright QSOs across the full *HST* far-UV band (1150–1700Å). Target QSOs were selected so that a peak signal-to-noise ratio (S/N)  $\sim 15\text{-}20$  per resolution element of  $17 \text{ km s}^{-1}$  could be obtained in 5 or fewer orbits. For each target, both G130M and G160M exposures were obtained (see Table 1 in Paper 1 for the observing log).

For this targeted sample, we have intentionally chosen galaxies with a range of luminosities ( $< 0.01 L^*$  to  $L^*$ ) and morphologies (massive spirals to dwarf irregulars, including star-bursting systems, passive dwarfs and low-surface-brightness galaxies) in order to probe the CGM of a variety of late-type galaxies. Although the sample has limited

size, it was nevertheless constructed with the goal of characterizing the CGM of a wide range of late-type galaxies for input into models of galactic evolution. Most targeted QSO/galaxy pairs are single-QSO sight lines probing single-galaxy CGMs. However, one galaxy is probed by three sight lines (Keeney et al. 2013), and one of these three QSO sight lines probes two different galaxies at two distinct redshifts. Furthermore, two adjacent sight lines (1ES 1028+511 and 1SAX J1032.3+5051) were chosen to probe transverse cloud sizes in the CGM of two low-luminosity galaxies. All of these constraints provide a unique, although modest-sized sample for CGM studies. The expansion of the COS-Halos effort to target QSO/dwarf galaxy pairs (“COS-Dwarfs”; Bordoloi et al. 2014) now provides CGM data for a second sample with a similar range of galaxy luminosities but different selection methods to this sample.

Table 1 presents the targeted sample with the following basic information by column: (1) the QSO sight line name; (2) the associated galaxy name; (3) the absorber velocity or velocities associated with the tabulated galaxy, in  $\text{km s}^{-1}$ ; (4) the instrument(s) used for the absorber detections; (5) the galaxy’s recession velocity ( $cz_{\text{gal}}$ ), in  $\text{km s}^{-1}$ ; (6) the rest-frame  $g$ -band galaxy luminosity in  $L^*$  units (we adopt  $M_g^* = -20.3$ , the value of Montero-Dorta & Prada (2009) at  $h = 0.7$ ); (7) the impact parameter ( $\rho$ ), in kpc; (8) the virial radius ( $R_{\text{vir}}$ ), in kpc; (9) the ratio of impact parameter to  $R_{\text{vir}}$ ; (10) the ratio of the impact parameter of the tabulated galaxy to that of the next-nearest galaxy ( $\eta_\rho \equiv \rho_{\text{ng}}/\rho_{\text{nnng}}$ ); (11) the ratio of the normalized impact parameter (in virial radii) of the tabulated galaxy to that of the next-nearest galaxy ( $\eta_{\text{vir}} \equiv (\rho/R_{\text{vir}})_{\text{ng}}/(\rho/R_{\text{vir}})_{\text{nnng}}$ ); and (12) the ratio of normalized galaxy-absorber velocity difference of the tabulated galaxy to that of the next-nearest galaxy ( $\eta_{\Delta v} \equiv (|\Delta v|/v_{\text{esc}})_{\text{ng}}/(|\Delta v|/v_{\text{esc}})_{\text{nnng}}$ ). The absorption velocity used in the  $\Delta v$  calculation for column 12 is the weighted mean of the measured  $\text{Ly}\alpha$  component velocities, where the weights are set equal to the H I column density of each component. Furthermore, a minimum  $|\Delta v|$  of  $15 \text{ km s}^{-1}$  is assumed when calculating  $\eta_{\Delta v}$ ; this value is the uncertainty in the absolute wavelength calibration of the *HST*/COS G130M and G160M gratings (Green et al. 2012).

An entry in columns 10, 11 or 12 that is significantly  $> 1.0$  suggests that an alternative association with another nearby galaxy is possible. See Section A.2 of the Appendix for discussion of individual cases, and Section 7.2 for a general discussion of the question of association.

The derivation of virial radius (column 8) from the optical luminosity (column 6) is based on the abundance-matching process of Paper 1 (see their Section 3.1 for a detailed discussion); while Paper 1 explored several possible derivations of halo mass from galaxy luminosity, in this paper the “hybrid” prescription was adopted. Because the galaxy luminosities in column 6 are derived from rest-frame  $g$ -band magnitudes (or estimates) rather than  $B$ -band they differ slightly from those in Paper 1, as do the correspondingly updated halo masses and virial radii.

To enlarge the sample over a wider range of galaxy properties, we utilized serendipitous foreground galaxies along

archival STIS sight lines to provide information on more luminous galaxies out to  $z \leq 0.2$  over similar impact parameters to the targeted sample. Out of the entire suite of STIS medium-resolution echelle spectroscopy, there are 16 sight lines that probe the extended CGM of 35 low- $z$  galaxies, each with a detected system of absorption lines (see Danforth et al. 2016, for a definition of “systems of absorbers”). Many of these STIS targets are among the brightest QSOs, so that *FUSE* far-UV spectroscopy is available for many of them. At these low redshifts, *FUSE* data probes O VI and C III metal lines and  $\text{Ly}\beta$ , and often higher Lyman lines, that are used to determine more accurate  $N_{\text{HI}}$  values for partially-saturated  $\text{Ly}\alpha$  lines (see Section 3). Many of these same bright targets were also re-observed with COS as part of the GTO program (see Savage et al. 2014).

For the serendipitous sample, we set a limit on the impact parameter in units of the virial radius of  $\rho/R_{\text{vir}} < 2.0$  and a limit on the relative velocity of the absorber to the galaxy of  $|\Delta v| < 400 \text{ km s}^{-1}$ . Note that Paper 1 defined both “serendipitous” and “alternate” samples of galaxies that were within  $|\Delta v| < 400 \text{ km s}^{-1}$  of an absorber and  $\rho/R_{\text{vir}} < 1.5$  of the QSO sight line using different virial radius definitions (see Section 4 and Tables 3 and 4 of Paper 1). A slightly larger range of impact parameters is adopted here to explore more thoroughly whether the absorbers can be associated with individual galaxies (see Section 7.2). We have merged objects from both of these samples into a single “serendipitous” sample with a larger virial radius cut-off to accommodate the updated galaxy luminosities, virial radii, etc. This allows us to keep all but four of the absorber-galaxy associations initially listed in the combined “serendipitous”+“alternate” samples of Paper 1. The QSO/galaxy systems that are no longer included in our analysis are PKS 0405–123 / 2MASX J04080654–1212494 (the only one from the original serendipitous sample now excluded), PKS 2155–304 / ESO 466–32, PKS 2155–304 / J215846.5–301738, and Ton 28 / UGCA 201; none of these systems have associated metal lines. The exclusion of these QSO/galaxy pairs from this study does not preclude their potential physical association since the CGM/IGM boundary doesn’t appear to be identifiable observationally (see Figure 7 of Paper 1).

The sight lines used to define our serendipitous absorber sample are presented in Danforth & Shull (2008, see also Tilton et al. 2012), which includes very bright FUV targets possessing both high resolution  $7 \text{ km s}^{-1}$ , moderate  $S/N \sim 5$ –15 STIS E140M spectra and also *FUSE*  $\sim 20 \text{ km s}^{-1}$  FUV spectra. Serendipitous absorbers have higher Lyman-series lines as well as the O VI doublet lines falling within the higher sensitivity regions of the *FUSE* detector, providing detections at  $\log N_{\text{O VI}} \geq 13.2$  (Danforth & Shull 2005; Stocke et al. 2006) when there are no obscuring Galactic absorption lines. In the current study we have used only those  $\sim 500$   $\text{Ly}\alpha$  absorbers with  $\log N_{\text{HI}} \geq 13.0$  ( $W_\lambda \geq 54 \text{ m}\text{\AA}$ ) — an equivalent width detectable in all STIS spectra (Danforth & Shull 2008). The basic data for these “absorber-selected” galaxies are given in Table 2, which duplicates the information given for the targeted sample in Table 1.

Table 1. Targeted Sample Summary

Sight Line	Galaxy	$cz_{\text{abs}}$ ( $\text{km s}^{-1}$ )	Instrument	$cz_{\text{gal}}$ ( $\text{km s}^{-1}$ )	$L$ ( $L^*$ )	$\rho$ (kpc)	$R_{\text{vir}}$ (kpc)	$\rho/R_{\text{vir}}$	$\eta_p^a$	$\eta_{\text{vir}}^b$	$\eta_{\Delta v}^c$
(1)	(2)	(3)	(4)	(5)	(6)	(7)	(8)	(9)	(10)	(11)	(12)
IES 1028+511	UGC 5740	728	COS	649	0.007	110	54	2.04	4.23	4.00	0.71
IES 1028+511	SDSS J103108.88+504708.7	967	COS	934	0.005	26	51	0.51	0.25	0.25	0.06
ISAX J1032.3+5051	UGC 5740	704	COS	649	0.007	79	54	1.46	1.80	1.69	0.33
FBQS J1010+3003	UGC 5478	1264, 1380	COS	1378	0.059	57	78	0.73	0.26	0.18	0.01
HE 0435-5304	ESO 157-49	1514, 1647, 1719	COS	1673	0.12	172	93	1.85	1.28	0.54	1.41
HE 0439-5254	ESO 157-49	1581, 1653, 1763, 1805	COS	1673	0.12	93	93	1.00	0.93	0.41	0.17
HE 0439-5254	ESO 157-50	3861	COS	3874	0.43	89	137	0.65	0.73	0.29	0.22
PG 0832+251	NGC 2611	5221, 5337, 5396, 5444	COS, FUSE	5226	0.42	53	136	0.39	4.08	1.95	0.27
PMN J1103-2329	NGC 3511	1113, 1194	COS	1114	0.58	97	151	0.64	2.02	1.31	6.72
RX J0439.6-5311	ESO 157-49	1638, 1674, 1734	COS	1673	0.12	74	93	0.80	1.19	0.60	0.13
SBS 1108+560	M 108	654, 715, 778	COS	696	0.68	22	161	0.14	0.11	0.03	0.01
SBS 1122+594	IC 691	1221	COS	1199	0.095	45	87	0.52	1.07	0.60	0.41
VII Zw 244	UGC 4527	715	COS	721	0.003	7	47	0.15	0.02	0.02	0.04

<sup>a</sup> The ratio of the impact parameter (in kpc) of the tabulated galaxy to that of the next-nearest galaxy:  $\eta_p = p_{\text{ng}}/p_{\text{nnng}}$ .

<sup>b</sup> The ratio of the normalized impact parameter of the tabulated galaxy to that of the next-nearest galaxy:  $\eta_{\text{vir}} = (\rho/R_{\text{vir}})_{\text{ng}}/(\rho/R_{\text{vir}})_{\text{nnng}}$ .

<sup>c</sup> The ratio of the normalized absorber-galaxy velocity difference of the tabulated galaxy to that of the next-nearest galaxy:  $\eta_{\Delta v} = (|\Delta v|/v_{\text{esc}})_{\text{ng}}/(|\Delta v|/v_{\text{esc}})_{\text{nnng}}$ .

**Table 2.** Serendipitous Sample Summary

Sight Line	Galaxy	$cz_{\text{abs}}$ ( $\text{km s}^{-1}$ )	Instrument	$cz_{\text{gal}}$ ( $\text{km s}^{-1}$ )	$L$ ( $L^*$ )	$\rho$ (kpc)	$R_{\text{vir}}$ (kpc)	$\rho/R_{\text{vir}}$	$\eta_{\rho}^a$	$\eta_{\text{vir}}^b$	$\eta_{\Delta v}^c$
(1)	(2)	(3)	(4)	(5)	(6)	(7)	(8)	(9)	(10)	(11)	(12)
3C 273	SDSS J122815.96+014944.1	1019	COS, FUSE	911	0.004	70	50	1.40	0.41	0.51	1.54
3C 273	SDSS J122950.57+020153.7	1585	COS, FUSE	1775	0.006	81	53	1.53	0.31	0.70	4.55
3C 351	Mrk 892	3465, 3597	STIS	3581	0.15	173	98	1.77	0.63	0.81	0.46
H 1821+643	SDSS J182202.70+642138.8	36139, 36307, 36339, 36439, 36631	COS	36436	1.1	157	189	0.83	< 0.16	...	...
Mrk 335	SDSS J000529.16+201335.9	1961, 2281	COS, FUSE	1950	0.008	97	55	1.76	0.22	0.81	0.85
Mrk 876	NGC 6140	923, 978	COS, FUSE	908	0.72	257	163	1.58	0.41	0.25	0.12
PG 0953+414	SDSS J095638.90+411646.1	42512, 42664, 42759, 42907	COS, FUSE	42759	3.1	438	265	1.65	1.08	0.53	0.88
PG 1116+215	SDSS J111905.51+211733.0	17614, 17676, 17786, 18202	COS, FUSE	17993	0.10	133	89	1.49	0.52	1.05	3.89
PG 1116+215	SDSS J111906.68+211828.7	41522, 41522	COS, FUSE	41428	1.2	139	192	0.72	0.22	0.19	0.16
PG 1211+143	IC 3061	2114	STIS, FUSE	2316	0.32	138	125	1.10	0.39	0.62	1.83
PG 1211+143	SDSS J121409.55+140420.9	15170, 15321, 15357, 15431, 15574	STIS, FUSE	15309	0.92	137	177	0.77	0.75	0.48	0.69
PG 1211+143	SDSS J121413.94+140330.4	19305, 19424, 19481, 19557	STIS, FUSE	19334	0.12	72	93	0.77	0.48	0.94	0.91
PG 1216+069	SDSS J121930.86+064334.4	23880, 24059, 24141	COS, FUSE	24116	3.5	505	275	1.84	0.98	0.36	0.22
PG 1216+069	SDSS J121923.43+063819.7	37049, 37138, 37363, 37455	COS, FUSE	37204	0.74	93	164	0.57	0.13	0.19	0.05
PG 1259+593	UGC 8146	702	COS, FUSE	668	0.046	114	74	1.54	0.17	0.11	0.65
PG 1259+593	SDSS J130101.05+590007.1	13825, 13914, 14014	COS, FUSE	13862	0.47	138	141	0.98	1.55	0.86	0.53
PHL 1811	SDSS J215456.65-091808.6	15418, 15444	COS, FUSE	15453	1.5	269	207	1.30	0.89	0.29	0.02
PHL 1811	SDSS J215517.30-091752.0	21998, 22042	COS, FUSE	21951	2.7	502	253	1.98	1.47	0.77	0.53
PHL 1811	J215447.5-092254	23313	COS, FUSE	23278	0.74	309	164	1.88	0.57	0.65	0.49
PHL 1811	J215450.8-092235	23652, 23710	COS, FUSE	23623	0.26	237	116	2.04	0.74	0.82	0.95
PHL 1811	2MASX J21545996-092224.9	24226	COS, FUSE	24223	0.56	35	150	0.23	0.39	0.42	0.21
PHL 1811	J215506.5-092326	39658, 39795	COS, FUSE	39758	2.3	228	239	0.95	< 0.23	...	...
PHL 1811	J215454.9-092331	52914, 52933	COS	52873	1.4	354	204	1.74	< 0.35	...	...
PKS 0312-770	J031201.7-765517	17824	STIS	17792	0.34	239	127	1.88	< 0.24	...	...
PKS 0312-770	J03158.5-764855	35466, 35813	STIS	35732	2.1	381	231	1.65	< 0.38	...	...
PKS 0405-123	2MASX J04075411-1214493	28947, 28958	COS, FUSE	29050	1.2	378	192	1.97	1.41	0.70	4.39
PKS 0405-123	J040743.9-121209	45617, 45783, 45871	COS	45989	0.89	197	175	1.13	< 0.20	...	...
PKS 1302-102	J040751.2-121137	49910, 49946, 50001, 50059, 50104, 50158	COS	50127	1.8	117	222	0.53	< 0.12	...	...
PKS 1302-102	NGC 4939	3455	COS, FUSE	3112	3.2	261	267	0.98	0.33	0.23	0.84
PKS 1302-102	2MASX J13052026-1036311	12573, 12655, 12703	COS, FUSE	12755	2.8	227	256	0.89	0.72	0.41	0.52
PKS 1302-102	2MASX J13052094-1034521	28179, 28439	COS, FUSE	28304	3.4	353	273	1.29	0.91	0.39	0.08
PKS 2155-304	2MASX J21584077-3019271	16965, 17113, 17340	COS, FUSE	17005	1.7	425	217	1.96	0.59	0.43	0.11
PKS 2155-304	J215845.1-301637	31635, 31697, 31754	COS, FUSE	31887	2.2	403	238	1.69	< 0.40	...	...
Q 1230+0115	CGCG 014-054	1497	COS, FUSE	1105	0.004	70	50	1.40	0.32	0.75	3.34
Q 1230+0115	SDSS J123047.60+011518.6	23294, 23404	COS, FUSE	23327	0.19	55	105	0.52	0.10	0.14	0.07

<sup>a</sup>The ratio of the impact parameter (in kpc) of the tabulated galaxy to that of the next-nearest galaxy:  $\eta_{\rho} = \rho_{\text{ng}}/\rho_{\text{nnng}}$ .

<sup>b</sup>The ratio of the normalized impact parameter of the tabulated galaxy to that of the next-nearest galaxy:  $\eta_{\text{vir}} = (\rho/R_{\text{vir}})_{\text{ng}}/(\rho/R_{\text{vir}})_{\text{nnng}}$ .

<sup>c</sup>The ratio of the normalized absorber-galaxy velocity difference of the tabulated galaxy to that of the next-nearest galaxy:  $\eta_{\Delta v} = (|\Delta v|/v_{\text{esc}})_{\text{ng}}/(|\Delta v|/v_{\text{esc}})_{\text{nnng}}$ .

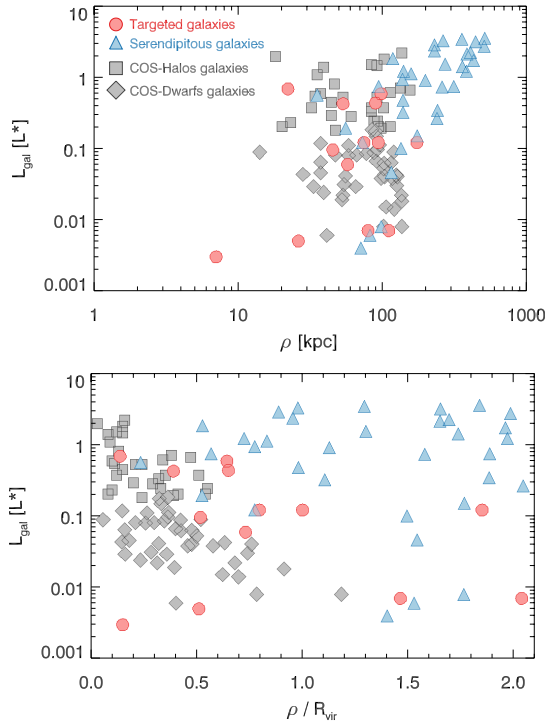


**Figure 1.** *Top:* The distribution of targeted and serendipitous galaxies in impact parameter to the QSO sight line ( $\rho$ ) and rest-frame  $g$ -band luminosity ( $L_{\text{gal}}$ ). The targeted galaxies tend to have lower luminosities and smaller impact parameters. Gray squares show the distribution of COS-Halos galaxies, and gray diamonds show the distribution of COS-Dwarfs galaxies. *Bottom:* Same as the top panel, except the impact parameter has been normalized by the virial radius of the nearest galaxy. The targeted and serendipitous galaxies are probed by the QSO sight lines over a similar range of virial radii, but the targeted galaxies are probed primarily at  $\rho < R_{\text{vir}}$ .

### 2.1. Comparison with COS-Halos and COS-Dwarfs

The CGM sample in the present study has many similarities with the COS-Halos (Tumlinson et al. 2011, 2013) and COS-Dwarfs (Bordoloi et al. 2014) surveys, but also important differences. Here, we compare the general properties of our targeted and serendipitous subsamples with those of COS-Halos and COS-Dwarfs. However, comparisons of specific measurements and derivations can also be found throughout the manuscript when appropriate, particularly in Sections 5.4 and 6.1.

The survey design for COS-Halos and COS-Dwarfs is similar to that for our targeted subsample. All examine close QSO-galaxy associations ( $\rho \lesssim 160$  kpc; see top panel of Figure 1), with COS-Halos focusing on  $L \gtrsim 0.1 L^*$  galaxies and COS-Dwarfs focusing on  $L \lesssim 0.1 L^*$  galaxies. Our targeted subsample probes galaxies at similar impact parameters over nearly the full range of luminosity of the combined COS-Halos and COS-Dwarfs samples. However, the similarity in the distribution of basic observables breaks down when the impact parameter is normalized by the virial radius of the nearest galaxy, as shown in the bottom panel of Figure 1. In this view it is clear that the COS-Halos galaxies are all probed at  $\rho \lesssim 1/2 R_{\text{vir}}$  and the COS-Dwarfs galaxies are generally probed at  $\rho \lesssim R_{\text{vir}}$ , whereas our targeted galaxies are probed at  $1/2 R_{\text{vir}} \lesssim \rho \lesssim 2 R_{\text{vir}}$ . Further, even though our

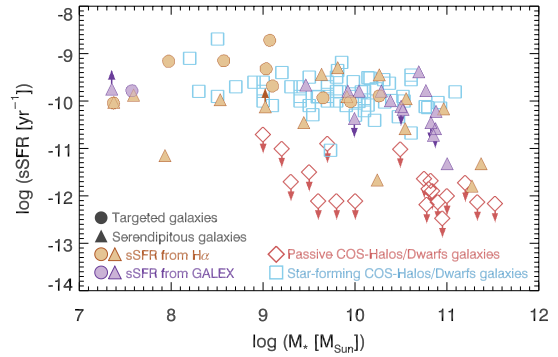


**Figure 2.** A comparison of the stellar mass ( $M_*$ ) and specific star formation rate (sSFR) of the targeted and serendipitous galaxies with those of the COS-Halos and COS-Dwarfs. Our sample includes several galaxies (both targeted and serendipitous) that are less massive than any COS-Dwarfs galaxy.

serendipitous galaxies were not targeted in the same way as the other surveys, when combined with our targeted galaxies they form a rather complementary sample to the COS-Halos and COS-Dwarfs galaxies in this parameter space.

However, despite these similarities in targeted survey design, the COS-Halos galaxies in particular were chosen to be rather isolated so that, in standard theoretical terminology, they would be classified as dominant or “central” halos. Our targeted and serendipitous samples are much more heterogeneous, with QSOs probing the CGM of spirals and irregular galaxies spanning a wide range in luminosity. None of the targeted or nearest serendipitous galaxies were chosen specifically to be isolated or to be “central” halos.

Figure 2 compares the stellar masses and specific star formation rates of the targeted and serendipitous galaxies with the galaxies studied by COS-Halos and COS-Dwarfs. We discuss our methods for deriving stellar masses and specific star formation rates for the targeted and serendipitous galaxies in Section 4, but present Figure 2 now to demonstrate that the targeted and serendipitous samples include a few associated galaxies an order of magnitude less massive than any studied with COS-Dwarfs. However, only a few passive galaxies are included in this sample, compared to the substantial number targeted by COS-Halos. Disregarding the passive galaxies for the moment, both this sample and the COS-Halos and COS-Dwarfs samples show a remarkable constancy of sSFR over 4 decades of stellar mass. While most of the targeted and serendipitous galaxies in Figure 2 align well with the star-forming galaxies studied by COS-Halos and COS-Dwarfs, there are only four early-type serendipitous galaxies that overlap with the passive COS-Halos and COS-Dwarfs galaxies. We did not target passive galaxies specifically; this is another difference between the current survey and the COS-Halos/Dwarfs studies. However, there could be late-type galaxies that are good alternative identifications for galaxies associated with these absorbers (as postulated in Paper 1); this situation will be reviewed in detail in Section 7.2.1. As shown in Paper 1 (see their Figure 6), the position angle distribution of absorber locations relative to the associated galaxy’s disk is reasonably isotropic (see Section 7.1), although we did not specifically select our

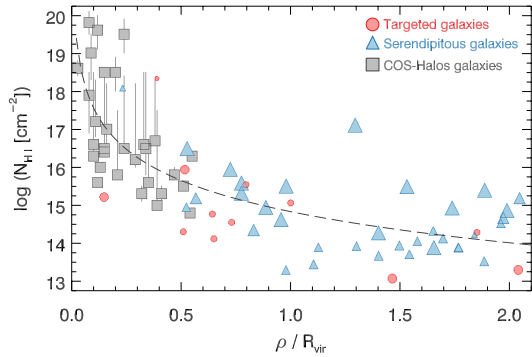


**Figure 3.** Total H I column density,  $N_{\text{HI}}$ , in the CGM as a function of normalized impact parameter for the targeted and serendipitous galaxies, compared with measurements from COS-Halos (Werk et al. 2014). All of the measurements are consistent with a single power-law fit (dashed line), which is described in detail in Section 5.4.

sample using that as a criterion.

While the current sample does not lack in close QSO/galaxy pairs (see Figure 1), COS-Halos has many more probes through the close-in CGM where most of the cool gas mass is concentrated (Werk et al. 2014, and Paper 1), allowing the COS-Halos studies to better determine physical conditions in the region at  $\rho \leq 1/2 R_{\text{vir}}$ . Remarkably, however, when the COS-Halos measurements of total CGM H I column density,  $N_{\text{HI}}$ , are plotted next to the values measured for this sample as a function of  $\rho/R_{\text{vir}}$  as in Figure 3, they are found to be consistent with a common power-law distribution (dashed line in Figure 3)<sup>2</sup>. Thus, there seems to be broad agreement between our measurements and those of COS-Halos on basic observables despite the different ranges of galaxy luminosity and impact parameter probed by these samples.

Unfortunately, this agreement does not generally extend to derived quantities. The difference in the range of impact parameters probed by this study compared to COS-Halos can be at least partially responsible for different trends with radius; e.g., whereas the photo-ionization modeling of Werk et al. (2014) found correlations of ionization parameter and pressure with normalized impact parameter, this study does not find such correlations in the current dataset (see Sections 5 and 7.1). It is possible that the more diverse galaxy selection is a factor in this difference; i.e., the targeted and serendipitous galaxies in this study are often not the gravitational center of their circumgalactic environment, whereas the COS-Halos galaxies have a much better claim to being “central” halos, at the gravitational center of the region. Operationally, this means that the impact parameters in this study may not be the most appropriate indicator of distance from the local gravitational center to which the CGM clouds find themselves responding. For example, if the internal cloud pressures are at least partially due to the external pressure of a surrounding hot medium, it is distance from the physical cen-

troid of that surrounding medium that should be the reference point from which to determine physical quantities. Given their luminous and isolated selection criteria, the COS-Halos galaxies are likely to be a much closer match to that “local” physical centroid than the targeted and serendipitous galaxies in the present sample.

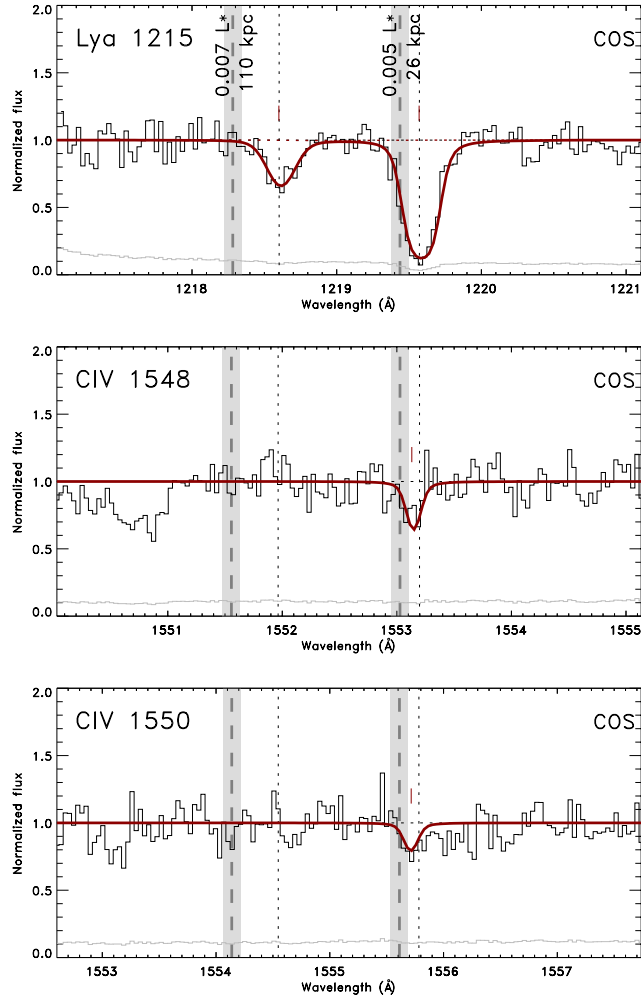
A major difference in inferred CGM properties between our analysis and that of the COS-Halos team is in the total mass of the cool CGM (see Werk et al. 2014; Stern et al. 2016; Prochaska et al. 2017, and Section 6.1); our total mass estimate is a factor of  $\sim 6$  lower than the latest estimate from Prochaska et al. (2017). While there are significant differences in associated galaxy properties and absorber impact parameters as detailed above, a large portion of the difference between these values is attributable to the different choice of meta-galactic ionizing UV radiation field employed in the photo-ionization modeling. COS-Halos uses the higher intensity Haardt & Madau (2001) radiation field, while we use the lower Haardt & Madau (2012) spectrum. We quantify the difference this makes on the CGM cool mass calculation in Section 6.1, and use both surveys to derive a new, best estimate for the CGM cool gas mass somewhat higher than found in Paper 1 and lower than the COS-Halos values.

### 3. HST AND FUSE UV SPECTROSCOPY

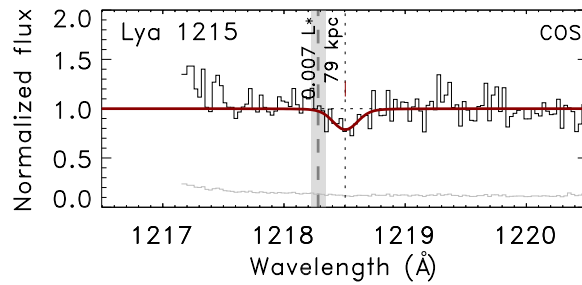
In this Section we present the COS, STIS and FUSE spectra of the absorbers associated with both the targeted and the serendipitously detected galaxy halos. The COS spectroscopy of many of these targets was described in detail in Danforth et al. (2016), including specifics of the data handling (e.g., flux and wavelength calibrations, absorber identifications) and basic observables such as equivalent widths. A detailed discussion of the error analysis of these measurements can be found in Keeney et al. (2013). The STIS (E140M data only) and FUSE spectroscopy were described in detail in Tilton et al. (2012). Only one of the targeted sight lines (PG 0832+251) was observed with FUSE, but many of the serendipitous sight lines were. Because the COS spectra have significantly higher S/N compared to the STIS data for these serendipitous sight lines, we have used the COS spectra where they exist. Since most of the STIS targets are among the brightest QSOs in the sky, several have been reobserved using COS, including in the GTO program of bright targets reported in Savage et al. (2014) and Danforth et al. (2016).

#### Fig. Set 4. Absorption Line Fits

<sup>2</sup> The H I column density measurements for the targeted and serendipitous samples are described in Section 3 and the power-law fit in Section 7.1.



4.1: 1ES 1028+511 absorbers at  $cz_{\text{abs}} = 728$  &  $967 \text{ km s}^{-1}$  (Systems 1 & 2).



4.2: 1SAX J1032.3+5051 absorber at  $cz_{\text{abs}} = 704 \text{ km s}^{-1}$  (System 3).

**Figure 4.** Absorption line fits for H I and associated metal lines detected by COS, STIS or *FUSE* for all absorbers listed in Table 3. The species name and the provenance of the spectrum are labeled in each individual panel. Dotted vertical lines show  $\text{Ly}\alpha$  component velocities and dashed vertical lines with gray shaded areas show the nearest galaxy velocity and  $1\sigma$  uncertainty; the luminosity of this nearest galaxy and its impact parameter from the QSO sight line are also labeled. The horizontal dotted line shows the continuum fit, dotted red lines show Voigt profile fits to individual velocity components, and the solid red line shows the total fit to all components. When absorption is confused by the presence of gas at another redshift, the relevant portion of the spectrum is still shown but not fit by a Voigt profile. The complete figure set (45 images) is available in the online journal.



**Table 3.** Multi-Component Absorption Line Fits

System #	Sight Line	Ion	$cz_{\text{abs}}$ ( $\text{km s}^{-1}$ )	$b$ ( $\text{km s}^{-1}$ )	$\log N$ ( $N$ in $\text{cm}^{-2}$ )	Comments
(1)	(2)	(3)	(4)	(5)	(6)	(7)
1	IES 1028+511	H I	728	$27.3 \pm 5.9$	$13.30 \pm 0.06$	Voigt profile fit to $\text{Ly}\alpha$
2	IES 1028+511	H I	967	$21.8 \pm 2.5$	$14.30 \pm 0.15$	Voigt profile fit to $\text{Ly}\alpha$
		C IV	954	$12.3 \pm 6.6$	$13.34 \pm 0.10$	Simultaneous fit to doublet
3	1SAX J1032.3+5051	H I	704	$29.6 \pm 13.1$	$13.08 \pm 0.27$	Voigt profile fit to $\text{Ly}\alpha$
4	FBQS J1010+3003	H I	1264	$36.9 \pm 11.9$	$13.27 \pm 0.09$	Voigt profile fit to $\text{Ly}\alpha$
5	FBQS J1010+3003	H I	1380	$36.8 \pm 2.9$	$14.47 \pm 0.08$	Voigt profile fit to $\text{Ly}\alpha$
6	HE 0435–5304	H I	1514	$29.4 \pm 3.7$	$13.80 \pm 0.04$	Voigt profile fit to $\text{Ly}\alpha$
7	HE 0435–5304	H I	1647	$67.5 \pm 15.9$	$14.00 \pm 0.11$	BLA; Voigt profile fit to $\text{Ly}\alpha$
8	HE 0435–5304	H I	1719	$25.3 \pm 11.8$	$13.49 \pm 0.30$	Voigt profile fit to $\text{Ly}\alpha$
9	HE 0439–5254	H I	1581	$5.6 \pm 14.3$	$12.76 \pm 0.24$	Voigt profile fit to $\text{Ly}\alpha$

NOTE—Table 3 is published in its entirety in machine-readable format. A portion is shown here for guidance regarding its form and content.

In Figure 4 we show the associated H I and metal lines for all the targeted and serendipitous absorbers in our sample. The origin of the spectrum (COS, STIS or *FUSE*) for each particular ion is indicated on the individual plots. The sight lines and adopted  $\text{Ly}\alpha$  velocity components are given in the caption for each plot and the vertical dotted line shows the adopted velocities. The horizontal dotted line shows the continuum fit (see Danforth et al. 2016). Voigt profile fits to individual velocity components are shown as dotted red lines, and the total ensemble fit is shown as a solid red line; the best-fit Voigt profile parameters are tabulated in Table 3. The associated galaxy redshifts are indicated on the  $\text{Ly}\alpha$  plots as vertical dashed lines with a grey shaded area indicating the  $1\sigma$  uncertainties on the galaxy’s redshift. The nearest galaxy luminosity and its impact parameter to the QSO sight line are also indicated. Ions in spectral regions not covered by the FUV spectrographs due to the redshift of the absorber are not shown. When the line is obscured or confused by the presence of a Galactic absorption line (e.g., the Galactic DLA) or a strong absorption from gas at another redshift, the relevant portion of the spectrum is still shown but not fit by a Voigt profile. In some cases the associated metal lines do not line up precisely with the H I lines (particularly the O VI doublet) but the velocity offsets are quite small ( $< 30 \text{ km s}^{-1}$ ) once uncertainties in the absolute wavelength calibration of the COS, STIS and *FUSE* data are accounted for. While the higher ions, particularly the N V and O VI doublets, are measured and tabulated here, they are not used in this study of the cool CGM.

Table 3 contains the following information about each absorber as follows by columns: (1) A running system ID number, with absorption associated with our targeted sample having numbers  $< 100$  and absorption associated with our serendipitous sample having numbers  $> 100$ ; (2) sight

line target name; (3) the ion being fit; (4) absorber velocity ( $\text{km s}^{-1}$ ); (5) Doppler  $b$ -value in  $\text{km s}^{-1}$  and  $1\sigma$  errors; (6)  $\log N$  and  $1\sigma$  errors; and (7) comments pertaining to the fits to these absorptions. The presence of non-Poisson noise in COS data requires assuming a  $b$ -value to set a rigorous upper limit on equivalent width or column density (Keeney et al. 2012);  $b$ -values with no uncertainties are those assumed when calculating upper limits from COS data.

Since most of the serendipitous absorbers are found in the spectra of very bright QSOs, there have been analyses made of these same absorbers by other authors (see Section A.1 of the Appendix for details). In general, these analyses are either identical to within the quoted velocity and column density errors with what we show in Figure 4 and Table 3 or the previous analyses suggest a more complicated set of components to the more complex H I absorbers. These differences are to be expected when the lines ( $\text{Ly}\alpha$  specifically) are saturated. In general, these differences are not important for the results we present here and those presented in Paper 1 but do enter the CGM ensemble mass calculation through a “shadowing” factor as well as the individual cloud masses of the components (see Paper 1 and Section 6). In some cases, whether the multiple-component fits to  $\text{Ly}\alpha$  allow a very broad ( $b > 40 \text{ km s}^{-1}$ ), probably collisionally-ionized component (a broad  $\text{Ly}\alpha$  absorber or BLA; Savage et al. 2014) or not is an important detail (see also Stocke et al. 2014). The 28 BLAs in Table 3 are indicated with a comment in column 7 and reproduced in Table 4 for convenience.

**Table 4.** BLA Absorbers

System #	Sight Line	Ion	$cz_{\text{abs}}$ ( $\text{km s}^{-1}$ )	$b$ ( $\text{km s}^{-1}$ )	$\log N$ ( $N$ in $\text{cm}^{-2}$ )	Comments
(1)	(2)	(3)	(4)	(5)	(6)	(7)
7	HE 0435–5304	H I	1647	$67.5 \pm 15.9$	$14.00 \pm 0.11$	BLA; Voigt profile fit to $\text{Ly}\alpha$
11	HE 0439–5254	H I	1763	$105.3 \pm 56.7$	$13.49 \pm 0.20$	BLA; Voigt profile fit to $\text{Ly}\alpha$
15	PG 0832+251	H I	5337	48.0 :	14.96 :	BLA; Voigt profile fit to $\text{Ly}\alpha$ , $cz$ fixed
		C I		10	< 13.16	
		C II	5346	$12.5 \pm 4.5$	$13.59 \pm 0.07$	1334 Å line only
		C IV	5327	$20.5 \pm 2.7$	$14.41 \pm 0.07$	Simultaneous fit to doublet
		Si II			< 12.71	
		Si III	5346	$30.1 \pm 11.0$	$12.98 \pm 0.14$	
		Si IV	5327	$60.4 \pm 43.9$	$13.24 \pm 0.27$	Simultaneous fit to doublet
		O I		10	< 13.73	
		N V			< 13.77	Upper limit from intervening line
		Fe II		10	< 13.65	
		Fe III		10	< 14.17	
19	PMN J1103–2329	H I	1194	$48.6 \pm 7.0$	$14.76 \pm 0.16$	BLA; Voigt profile fit to $\text{Ly}\alpha$
		C I		20	< 13.33	
		C II		20	< 13.22	
		C IV	1189	$23.6 \pm 1.8$	$14.27 \pm 0.04$	Simultaneous fit to doublet
		Si II		20	< 12.26	
		Si III	1195	$28.9 \pm 0.5$	$12.95 \pm 0.01$	
		Si IV	1191	$25.1 \pm 4.8$	$13.01 \pm 0.05$	Simultaneous fit to doublet
		N V	1201	$52.5 \pm 10.3$	$13.66 \pm 0.06$	Simultaneous fit to doublet
		Fe II		20	< 13.84	
20	RX J0439.6–5311	H I	1638	$44.4 \pm 30.7$	$13.87 \pm 0.81$	BLA; Voigt profile fit to $\text{Ly}\alpha$
26	SBS 1122+594	H I	1221	$44.8 \pm 5.2$	$15.94 \pm 0.47$	BLA; Voigt profile fit to $\text{Ly}\alpha$
		C I		30	< 13.36	
		C II	1198	$34.6 \pm 7.1$	$13.80 \pm 0.06$	1334 Å line only
		C IV	1194	$39.6 \pm 1.5$	$14.74 \pm 0.03$	Simultaneous fit to doublet
		Si II		30	< 12.83	
		Si III	1215	$46.3 \pm 3.3$	$13.39 \pm 0.03$	
		Si IV	1208	$39.9 \pm 3.6$	$13.54 \pm 0.03$	Simultaneous fit to doublet
		O I		30	< 13.88	
		N V		45	< 13.64	
		Fe II		30	< 13.82	
103	3C 351	H I	3465	$41.1 \pm 4.8$	$13.47 \pm 0.05$	BLA; Voigt profile fit to $\text{Ly}\alpha$
107	H 1821+643	H I	36339	$46.5 \pm 1.9$	$14.12 \pm 0.03$	BLA; simultaneous fit to $\text{Ly}\alpha$ + $\text{Ly}\beta$
108	H 1821+643	H I	36439	$74.0 \pm 10.9$	$13.60 \pm 0.10$	BLA; simultaneous fit to $\text{Ly}\alpha$ + $\text{Ly}\beta$
		O VI	36415	$50.3 \pm 8.6$	$13.68 \pm 0.13$	1032 Å line only
112	Mrk 876	H I	923	$48.1 \pm 4.2$	$13.90 \pm 0.10$	BLA; Voigt profile fit to $\text{Ly}\alpha$
		O VI	932	$25.0 \pm 6.0$	$13.55 \pm 0.08$	<a href="#">Tilton et al. (2012)</a>
117	PG 0953+414	H I	42907	$53.1 \pm 6.1$	$13.15 \pm 0.04$	BLA; simultaneous fit to $\text{Ly}\alpha$ - $\text{Ly}\gamma$
		O VI	42873	$11.8 \pm 6.8$	$13.08 \pm 0.09$	Simultaneous fit to doublet
122	PG 1116+215	H I	41522	$59.8 \pm 5.7$	$13.78 \pm 0.10$	BLA; simultaneous fit to $\text{Ly}\alpha$ - $\text{Ly}\beta$
124	PG 1211+143	H I	2114	$65.2 \pm 3.9$	$13.45 \pm 0.03$	BLA; Voigt profile fit to $\text{Ly}\alpha$

Table 4 continued

Table 4 (*continued*)

System #	Sight Line	Ion	$cz_{\text{abs}}$ ( $\text{km s}^{-1}$ )	$b$ ( $\text{km s}^{-1}$ )	$\log N$ ( $N$ in $\text{cm}^{-2}$ )	Comments
(1)	(2)	(3)	(4)	(5)	(6)	(7)
		O VI			< 13.87	Upper limit from intervening line
127	PG 1211+143	H I	15357	$127.8 \pm 9.0$	$14.18 \pm 0.06$	BLA; simultaneous fit to Ly $\alpha$ -Ly $\delta$
134	PG 1216+069	H I	23880	$63.3 \pm 14.0$	$13.14 \pm 0.07$	BLA; Voigt profile fit to Ly $\alpha$
136	PG 1216+069	H I	24141	$42.3 \pm 2.8$	$14.15 \pm 0.02$	BLA; Voigt profile fit to Ly $\alpha$
145	PHL 1811	H I	15418	$72.8 \pm 5.1$	$13.65 \pm 0.03$	BLA; Voigt profile fit to Ly $\alpha$
154	PHL 1811	H I	39795	$60.9 \pm 8.0$	$13.19 \pm 0.04$	BLA; simultaneous fit to Ly $\alpha$ -Ly $\delta$
		O VI	39826	$22.4 \pm 3.6$	$13.59 \pm 0.04$	Simultaneous fit to doublet
156	PHL 1811	H I	52914	$41.7 \pm 0.9$	$14.22 \pm 0.03$	BLA; simultaneous fit to Ly $\alpha$ -Ly $\delta$
		O VI	52922	$18.1 \pm 2.2$	$14.11 \pm 0.03$	1038 Å line only
160	PKS 0312-770	H I	35813	$41.0 \pm 2.0$	$13.79 \pm 0.02$	BLA; <a href="#">Tilton et al. (2012)</a>
162	PKS 0405-123	H I	28958	$69.0 \pm 3.0$	$13.93 \pm 0.04$	BLA; <a href="#">Savage et al. (2014)</a>
		O VI	28955	$23.0 \pm 6.0$	$13.70 \pm 0.07$	<a href="#">Savage et al. (2014)</a>
165	PKS 0405-123	H I	45871	$47.6 \pm 0.8$	$13.72 \pm 0.01$	BLA; Voigt profile fit to Ly $\alpha$
		O VI		48	< 13.02	
167	PKS 0405-123	H I	49910	$54.0 \pm 13.0$	$13.11 \pm 0.16$	BLA; <a href="#">Savage et al. (2014)</a>
172	PKS 0405-123	H I	50158	$41.0 \pm 3.0$	$13.90 \pm 0.08$	BLA; <a href="#">Savage et al. (2014)</a>
179	PKS 2155-304	H I	16965	$52.3 \pm 0.9$	$14.34 \pm 0.01$	BLA; Voigt profile fit to Ly $\alpha$
180	PKS 2155-304	H I	17113	$67.9 \pm 1.7$	$14.08 \pm 0.01$	BLA; Voigt profile fit to Ly $\alpha$
		O VI	17149	$24.3 \pm 7.1$	$13.60 \pm 0.09$	1032 Å line only
182	PKS 2155-304	H I	31635	$47.1 \pm 2.3$	$13.98 \pm 0.03$	BLA; Voigt profile fit to Ly $\alpha$
		O VI		47	< 13.50	
184	PKS 2155-304	H I	31754	$43.2 \pm 8.6$	$13.28 \pm 0.12$	BLA; Voigt profile fit to Ly $\alpha$
		O VI		43	< 13.48	

Table 5. O VI Absorbers with No Associated H I

System #	Sight Line	Ion	$cz_{\text{abs}}$ ( $\text{km s}^{-1}$ )	$b$ ( $\text{km s}^{-1}$ )	$\log N$ ( $N$ in $\text{cm}^{-2}$ )	Comments
(1)	(2)	(3)	(4)	(5)	(6)	(7)
155	PHL 1811	O VI	39930	$33.2 \pm 4.6$	$13.61 \pm 0.04$	No associated H I; simultaneous fit to doublet
166	PKS 0405-123	O VI	49780	$56.0 \pm 2.0$	$13.85 \pm 0.01$	No associated H I; <a href="#">Savage et al. (2014)</a>

Additionally, there are two O VI-only absorbers (i.e., no associated H I) that are demonstrably collisionally-ionized gas ([Savage et al. 2010, 2014](#); [Stočke et al. 2014](#)). These were not included in the discussions in Paper 1 and it is not clear what associations these absorbers may or may not have with the individual, associated galaxies in this study. Regardless, given the likely high temperature ( $T > 10^5$  K) of these clouds, we do not consider them further in this study of the cool, photo-ionized CGM. Speculation as to the physical conditions and association of these absorbers to individ-

ual galaxies and galaxy groups can be found in [Savage et al. \(2014\)](#) and [Stočke et al. \(2014\)](#). The Voigt profile fits for these two absorbers are detailed in Table 5. All column densities, including those in logarithms, have units of  $\text{cm}^{-2}$ .

All absorption from H I and associated metal lines are fit with the minimum number of velocity components necessary to obtain an acceptable fit (characterized by a reduced- $\chi^2 \approx 1$ ), and all lines of a particular ion with significant absorption are fit simultaneously (i.e., all available Ly-series lines or both lines in the Si IV, C IV, or O VI doublets).

During these simultaneous fits between different instruments, the data are aligned in velocity space prior to the fit. During the fit, we preserve the relative spacing between velocity components but allow the absolute velocities to shift by  $< 30 \text{ km s}^{-1}$  to account for uncertainties in velocity registration between instruments. The velocities reported in Table 3 are those of the strongest line being fit (e.g.,  $\text{Ly}\alpha$  or  $\text{O VI } \lambda 1032$ ). All Voigt profiles are convolved with the instrumental line spread functions as part of the fitting procedure: we assume Gaussian line spread functions with  $\mathcal{R} = 17, 500$  and  $45,800$  for *FUSE* and STIS data, respectively, and the empirical line spread functions of Kriss (2011) for COS data.

Generally speaking, the serendipitous absorbers have higher-order Ly-series lines available to inform the H I fits, either in the COS or STIS data themselves when  $z_{\text{abs}} \gtrsim 0.1$ , or from *FUSE* at lower redshifts. These higher-order lines are crucial for assessing the component structure and Voigt profile parameters of H I systems with saturated, or even partially saturated,  $\text{Ly}\alpha$  absorption. When  $\text{Ly}\alpha$  absorption is present and saturated and no other H I lines are available (as is typical for the targeted absorbers) choosing the number of velocity components to include in the fit is quite subjective and can have significant effects on the derived Voigt profile parameters. Furthermore, since these saturated  $\text{Ly}\alpha$  absorbers reside on the flat part of the curve of growth, it is often true that a high  $b$ -value, low column density fit and a low  $b$ -value, high column density fit have very similar  $\chi^2$  values. Due to low-S/N or severe blending, the difference between the low and high column density solutions can span orders of magnitude; we adopt the lower column density solution whenever possible as a consequence of our minimum-component fitting philosophy.

These systematic uncertainties imply that the component structure, and inferred  $b$ -values and column densities, are much more reliable for absorbers with multiple Ly-series lines informing the H I fits. Uncertainties in Tables 3-5 are formal fitting uncertainties only and do not attempt to quantify the systematic issues described above. We characterize the amount of subjectivity in individual measurements qualitatively using absorber grades as described in Sections 5 and 6.

In the Appendix, Section A.1, we briefly discuss previous work done on the absorbers in the targeted and serendipitous samples. Since publication in Paper 1, all of the targeted and serendipitous absorbers have been re-fit after updating our data reduction pipeline. Updates were necessary to fix errors in parsing data quality flags at the exposure level, and to re-bin the data by 3 pixels so it is approximately Nyquist sampled after all exposures have been co-added (see Danforth et al. 2016 for details). Consequently, some of the component-level fits have changed from our earlier papers (Paper 1 and Danforth et al. 2016). A discussion on the impact that these multiple absorber fits have on the CGM absorber properties we have derived is found in Section 6.

#### 4. GALAXIES ASSOCIATED WITH THESE ABSORBERS

In this Section we describe the ground-based observations and analysis of the targeted and serendipitous galaxies associated with the absorbers as listed in Tables 1 and 2. The basic information obtained on these galaxies from our ground-based observations are listed in Tables 6 and 7 for the targeted and serendipitous samples, respectively. The following information is provided in these tables by column: (1) the QSO target sight line name; (2) the galaxy name; (3) the galaxy’s recession velocity ( $cz_{\text{gal}}$ ) in  $\text{km s}^{-1}$ ; (4) the galaxy luminosity in  $L^*$  units derived from rest-frame  $g$ -band magnitudes (excepting as discussed below); (5) the galaxy impact parameter ( $\rho$ ) in kpc; (6) the galaxy’s virial radius in kpc; (7) and (8) the logarithms of the galaxy halo and stellar masses in  $M_{\odot}$  units; (9) the galaxy’s metallicity relative to the solar value, with  $2\sigma$  (95% confidence level) uncertainties; (10) the galaxy’s inclination angle on the sky where well-defined; (11) and (12) the SFR in  $M_{\odot} \text{ yr}^{-1}$  as given by the galaxy’s  $\text{H}\alpha$  and *GALEX* FUV luminosities; and (13) and (14) the specific SFR (sSFR) in units of  $\text{yr}^{-1}$ , as derived from the  $\text{H}\alpha$  and FUV SFRs, respectively, and the galaxy stellar mass from column 8.

Many of the quantities in Tables 6 and 7 were either derived directly from the SDSS galaxy redshift survey database (DR12; Alam et al. 2015) or from our own observations. Most redshifts are derived from the SDSS galaxy redshift survey and have associated errors of  $\sim 30 \text{ km s}^{-1}$ ; other sources of galaxy redshifts and associated errors, including H I 21-cm emission redshifts, are described with the individual galaxy descriptions in Section A.2 of the Appendix where applicable. Tabulated stellar masses (column 8) use Equation 8 of Taylor et al. (2011), which needs only rest-frame ( $g - i$ ) color and  $i$ -band absolute magnitude, so it can be applied uniformly to our whole sample. We correct to rest-frame colors and magnitudes using the  $K$ -corrections of Chilingarian et al. (2010) and Chilingarian & Zolotukhin (2012). The virial radius (column 6) and halo mass (column 7) are derived from the galaxy luminosity (column 4) as described in Section 2 and Paper 1.

The galaxy metallicity (column 9) is derived using the O3N2 index of Pettini & Pagel (2004) unless otherwise noted below, with the exception of values that have no listed uncertainty; these metallicity estimates are derived from the galaxy’s stellar mass using the mass-metallicity relations of Tremonti et al. (2004) when  $\log M_* > 10.2$  or Lee et al. (2006) when  $\log M_* < 10.2$ . Figure 5 shows the measured galaxy metallicity as a function of stellar mass for our targeted and serendipitous galaxies. The mass-metallicity relations of Tremonti et al. (2004, dashed line) and Lee et al. (2006, dotted line) are overlaid, and are clearly a good match to our measurements. Thus, we feel that they provide reasonable estimates of the galaxy metallicity in cases where no direct measurements are available.

**Table 6.** Targeted Galaxy Properties

Sight Line	Galaxy	$c_{\text{zgal}}$ ( $\text{km s}^{-1}$ )	$L$ ( $L^*$ )	$\rho$ (kpc)	$R_{\text{vir}}$ (kpc)	$\log M_{\text{H}}$	$\log M_*$	$[\text{O}/\text{H}]^a$	$i$ (deg)	SFR( $\text{H}\alpha$ ) ( $M_{\odot} \text{ yr}^{-1}$ )	SFR(FUV) ( $M_{\odot} \text{ yr}^{-1}$ )	$\log \text{sSFR}$ ( $\text{H}\alpha$ )	$\log \text{sSFR}$ (FUV)
(1)	(2)	(3)	(4)	(5)	(6)	(7)	(8)	(9)	(10)	(11)	(12)	(13)	(14)
IES 1028+511	UGC 5740	649	0.007	110	54	9.94	7.97	$-0.57 \pm 0.59$	47	0.052-0.063	...	-9.17	
ISAX J1032.3+5051				79									
IES 1028+511	SDSS J103108.88+504708.7	934	0.005	26	51	9.87	7.57	$-0.26 \pm 0.72$	...	$> 0.00004$	0.006	$> -11.97$	-9.79
FBQS J1010+3003	UGC 5478	1378	0.059	57	78	10.42	8.57	$-0.24 \pm 0.67$	...	0.067-0.26	...	-9.16	
HE 0435-5304	ESO 157-49	1673	0.12	172	93	10.65	9.03	$-0.30 \pm 0.43$	80	0.23-0.50	0.02-0.08	-9.33	-10.12
HE 0439-5254				93									
RX J0439.6-5311				74									
HE 0439-5254	ESO 157-50	3874	0.43	89	137	11.16	9.07	$-0.41 \pm 0.43$	83	0.79-2.2	...	-8.73	
PG 0832+251	NGC 2611	5226	0.42	53	136	11.15	10.26	$+0.07 \pm 0.36$	74	0.99-2.3	0.11-0.49	-9.90	-10.57
PMN J1103-2329	NGC 3511	1114	0.58	97	151	11.29	9.65	$-0.22 \pm 0.46$	73	0.28-0.52	...	-9.94	
SBS 1108+560	M 108	696	0.68	22	161	11.37	9.95	$-0.03 \pm 0.26$	77	0.42-0.85	0.58-0.89	-10.02	-10.00
SBS 1122+594	IC 691	1199	0.095	45	87	10.57	9.10	$-0.32 \pm 0.28$	...	0.13-0.26	0.09-0.30	-9.69	-9.62
VII Zw 244	UGC 4527	721	0.003	7	47	9.76	7.37	$-0.33 \pm 0.95$	...	0.002	0.004	-10.05	-9.77

 NOTE—All masses are in units of  $M_{\odot}$  and specific star formation rate (sSFR) has units of  $\text{yr}^{-1}$ .

<sup>a</sup> Logarithm of the galaxy's oxygen abundance relative to solar, with  $2\sigma$  (95% confidence) error bars.

Table 7. Serendipitous Galaxy Properties

Sight Line	Galaxy	$cz_{gal}$ ( $\text{km s}^{-1}$ )	$L$ ( $L^*$ )	$\rho$ (kpc)	$R_{vir}$ (kpc)	$\log M_h$	$\log M_*$	[O/H] <sup>a</sup>	$i$ (deg)	SFR(H $\alpha$ ) ( $M_\odot \text{ yr}^{-1}$ )	SFR(FUV) ( $M_\odot \text{ yr}^{-1}$ )	$\log sSFR$ (H $\alpha$ )	$\log sSFR$ (FUV)
(1)	(2)	(3)	(4)	(5)	(6)	(7)	(8)	(9)	(10)	(11)	(12)	(13)	(14)
3C 273	SDSS J122815.96+014944.1	911	0.004	70	50	9.83	7.37	-0.43 $\pm$ 0.27	63	0.001-0.002	0.003-0.006	-10.03	-9.58
3C 273	SDSS J122950.57+020153.7	1775	0.006	81	53	9.92	7.93	-0.82 $\pm$ 0.98 <sup>b</sup>	...	0.0006	> 0.0005	-11.15	> -11.23
3C 351	Mrk 892	3581	0.15	173	98	10.72	9.25	-0.16 $\pm$ 0.27	65	0.02-0.25	0.03-0.05	-9.85	-10.56
H 1821+643	SDSS J182202.70+642138.8	36436	1.1	157	189	11.58	10.04	-0.04	43	0.58-1.4	1.3-1.7	-9.89	-9.80
Mrk 335	SDSS J000529.16+201335.9	1950	0.008	97	55	9.98	7.59	-0.48 $\pm$ 0.85	...	0.005	...	-9.88	...
Mrk 876	NGC 6140	908	0.72	257	163	11.39	9.81	-0.07 $\pm$ 0.44	44	3.1	...	-9.31	...
PG 0953+414	SDSS J095638.90+411646.1	42759	3.1	438	265	12.02	10.96	+0.09 $\pm$ 0.42	41	0.93-6.1	...	-10.17	...
PG 1116+215	SDSS J111905.51+211733.0	17993	0.10	133	89	10.60	9.44	-0.23	28	0.03-0.09	0.06-0.09	-10.46	-10.48
PG 1116+215	SDSS J111906.68+211828.7	41428	1.2	139	192	11.60	11.27	+0.25 $\pm$ 0.46	40	0.05-0.29	...	-11.80	...
PG 1211+143	IC 3061	2316	0.32	138	125	11.04	9.91	+0.05 $\pm$ 0.31	87	0.33-1.0	0.58-3.9	-9.91	-9.32
PG 1211+143	SDSS J121409.55+140420.9	15309	0.92	137	177	11.50	10.28	-0.07 $\pm$ 0.28	35	0.06-0.77	0.84-3.0	-10.39	-9.80
PG 1216+069	SDSS J121930.86+064334.4	24116	3.5	505	275	12.05	9.02	-0.44 $\pm$ 0.87	47	> 0.08	...	-10.13	> -9.39
PG 1216+069	SDSS J121923.43+063819.7	37204	0.74	93	164	11.40	10.26	+0.09 $\pm$ 0.27	31	7.0-27	10-20	-9.26	-9.39
PG 1259+593	UGC 8146	668	0.046	114	74	10.35	8.53	+0.01	46	1.6-6.3	...	-9.46	...
PG 1259+593	SDSS J130101.05+590007.1	13862	0.47	138	141	11.20	10.24	-0.33 $\pm$ 0.27	89	0.011-0.035	0.09-0.56	-9.98	-8.78
PHL 1811	SDSS J215456.65-091808.	15453	1.5	269	207	11.70	10.52	-0.02 $\pm$ 0.72	54	0.008-0.04	...	-11.67	...
PHL 1811	SDSS J215517.30-091752.	21951	2.7	502	253	11.96	11.37	+0.12 $\pm$ 0.406	48	> 0.08	1.2-2.2	> -11.62	-10.18
PHL 1811	J215447.5-092254	23278	0.74	309	164	11.40	9.92	-0.01 $\pm$ 0.480	22	0.07-1.1	< 0.11	-11.32	< -12.33
PHL 1811	J215450.8-092235	23623	0.26	237	116	10.95	9.46	+0.09 $\pm$ 0.30	26	0.94-4.0	1.0-1.3	-9.32	-9.80
PHL 1811	2MASX J21545996-0922249	24223	0.56	35	150	11.28	10.24	-0.41 $\pm$ 0.42	50	0.37-3.3	0.39-0.62	-8.94	-9.67
PHL 1811	J215506.5-092326	39758	2.3	228	239	11.89	10.88	+0.01	53	...	...	-9.56	-10.22
PHL 1811	J215454.9-092331	52873	1.4	354	204	11.68	10.77	-0.03 $\pm$ 0.30	43	1.9-21	2.4-4.6	-9.54	-9.79
PKS 0312-770	J031201.7-765517	17792	0.34	239	127	11.06	9.99	-0.08 $\pm$ 0.30	30	3.2-17	4.4-9.5	-9.54	-9.79
PKS 0312-770	J031158.5-764855	35732	2.1	381	231	11.84	10.87	-0.06	...	...	< 0.41	< -10.37	< -10.59
PKS 0405-123	2MASX J04075411-1214493	29050	1.2	378	192	11.60	10.55	+0.10	...	...	< 1.9	< -10.59	< -10.59
PKS 0405-123	J040743.9-121209	45989	0.89	197	175	11.48	10.50	+0.16 $\pm$ 0.52	75	0.31-3.9	0.44-2.1	-9.96	-10.23
PKS 0405-123	J040751.2-121137	50127	1.8	117	222	11.79	10.82	+0.05 $\pm$ 1.10	44	...	< 2.4	< -10.12	< -10.12
PKS 1302-102	NGC 4939	3112	3.2	261	267	12.03	10.54	+0.05	34	...	< 2.3	< -10.46	< -10.46
PKS 1302-102	2MASX J13052026-1036311	12755	2.8	227	256	11.98	10.85	+0.06	61	0.57-0.88	...	-10.59	...
PKS 1302-102	2MASX J13052094-1034521	28304	3.4	353	273	12.06	11.00	+0.11	34	...	0.72-1.3	-10.73	-10.73
PKS 2155-304	2MASX J21584077-3019271	17005	1.7	425	217	11.76	10.38	+0.03	32	< 0.65	0.26-0.47	-11.33	-11.33
PKS 2155-304	J215845.1-301637	31887	2.2	403	238	11.88	10.77	+0.09	65	...	0.93-2.4	-10.00	-10.00
Q 1230+0115	CGCG 014-054	1105	0.004	70	50	9.84	7.35	-0.16 $\pm$ 0.80	...	...	...	> -12.21	> -9.75
Q 1230+0115	SDSS J123047.60+011518.6	23327	0.19	55	105	10.81	9.63	-0.17	67	> 0.00001	> 0.004	-12.21	-9.44
										0.63-1.5	...	-9.44	...

NOTE—All masses are in units of  $M_\odot$  and specific star formation rate (sSFR) has units of  $\text{yr}^{-1}$ .

<sup>a</sup> Logarithm of the galaxy's oxygen abundance relative to solar, with  $2\sigma$  (95% confidence) error bars.

<sup>b</sup> This galaxy has no optical emission lines, but Keeney et al. (2014) estimated its [Fe/H] metallicity using SED modelling of its GALEX+SDSS photometry.

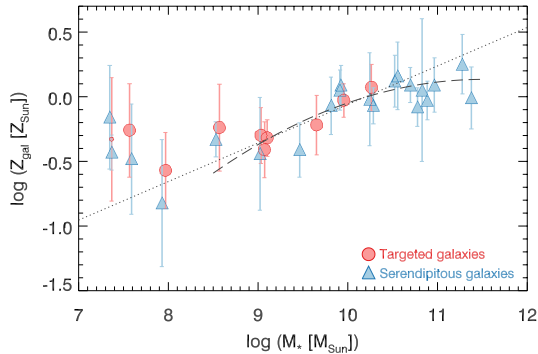


**Figure 5.** Relationship between the metallicity and stellar mass of targeted and serendipitous absorbers, with the relationships of Tremonti et al. (2004, dashed line) and Lee et al. (2006, dotted line) overlaid. These are a reasonable match to our data.

A range of  $H\alpha$  and FUV SFR is listed for each galaxy. The lower value comes from using the observed  $H\alpha$  and FUV luminosity, corrected for Galactic foreground extinction, to derive the corresponding SFR using the calibration of Hunter et al. (2010). The extinction correction uses  $E(B - V)$  from Schlafly & Finkbeiner (2011) and a Fitzpatrick (1999) reddening law with  $R_V = 3.1$ . The upper value attempts to correct for two additional systematic effects, and is used where possible to derive the sSFR values in columns 13 and 14. The first systematic effect we correct for is extinction internal to the galaxy. The attenuation at  $H\alpha$  is estimated using the galaxy inclination (derived from the galaxy’s observed axial ratio using the intrinsic axial ratios for different morphological types of Masters et al. 2010) and the attenuation relations of Driver et al. (2008). The FUV attenuation is estimated from the  $H\alpha$  attenuation using the prescription of Calzetti (2001). The second systematic effect is an aperture correction for galaxies whose  $H\alpha$  SFR is determined spectroscopically. In this case we use the  $H\alpha$  curve of growth for CALIFA galaxies (Iglesias-Páramo et al. 2013) to estimate the amount of  $H\alpha$  emission outside the spectroscopic aperture. When measurements of the galaxy’s half-light radius are not available we compare the galaxy’s  $r$ -band magnitude internal to the spectroscopic aperture with its total  $r$ -band magnitude to derive the aperture correction. Comparisons of the two aperture correction procedures for the subset of galaxies for which both can be derived show that they agree within 10–20%, and the aperture corrections of Iglesias-Páramo et al. (2013) have  $1\sigma$  uncertainties of 5–15%.

There are some cases where the spectroscopic aperture covers such a small fraction of the galaxy that the aperture correction is very large ( $> 10$ ); for these galaxies we do not attempt to perform an aperture correction and quote only a lower limit to the galaxy SFR that is equal to the SFR within the spectroscopic aperture. Fortunately,  $H\alpha$  imaging is available for most of the galaxies in our sample with recession velocities  $\leq 10000 \text{ km s}^{-1}$ , eliminating the problematical spectroscopic aperture corrections in these cases.

Where two sight lines are listed for the same galaxy, those sight lines probe the same galaxy at different impact parameters and position angles relative to the galaxy’s disk; e.g., three targets (HE 0435–5304, HE 0439–5254

and RX J0439.6–5311) all probe the nearly edge-on spiral ESO 157–49. Where a single target is listed more than once, that sight line probes multiple galaxies; e.g., HE 0439–5254 probes both ESO 157–49 and ESO 157–50.

Unless otherwise noted, narrow-band, redshifted  $H\alpha$  and broad-band images of each galaxy were obtained using the SPIcam optical imaging camera at the Apache Point Observatory (APO). Typically SDSS  $r$ -band images were used as the “off-band” to produce the pure  $H\alpha$  images even when  $H\alpha$  was present in the  $r$ -band (see Keeney et al. 2013, for detailed procedure). Broad-band and pure  $H\alpha$  images of both the targeted and serendipitous galaxies are presented in Appendix B along with observing details (e.g., epoch, exposure time, filters, “seeing”). Additionally (unless otherwise indicated below), we obtained major-axis, long-slit optical spectra of all galaxies using the Dual-channel Imaging Spectrograph (DIS) at APO. These APO observations include both low- and high-dispersion spectra unless adequate low-dispersion spectra were available through the SDSS spectroscopic database. Some of the serendipitously probed galaxies are at a distance great enough that the slit spectroscopy provides an adequate measurement of the total  $H\alpha$  flux. In all other cases the total  $H\alpha$  flux is determined from the images.

In the Appendix, Section A.2, the individual targeted and serendipitous galaxies are described in some detail both to illustrate the breadth in galaxy properties probed using the COS, STIS and FUSE observations and to make the connection between galaxies and absorbers.

## 5. CLOUDY PHOTO-IONIZATION MODELS

In Paper I we performed CLOUDY photo-ionization models (Ferland et al. 1998) of any absorber that had metal-line absorption from multiple ionization states of the same element (e.g., Si II/Si III/Si IV). Here we model all absorbers in Table 3 that meet this criterion, which leads to a slightly different list of modeled absorbers than that presented in Paper I. There are five absorbers that we model here but did not model in Paper I; these absorbers all have multi-ion absorption from the same element in Table 3 but not in Danforth & Shull (2008), which provided the serendipitous absorption line fits for Paper I. There are also four absorbers that we modeled in Paper I but do not model here due to uncertain H I column densities. Specifically, unlike Paper I we do not model the two low- $z$  absorbers found in the SBS 1108+560 sight line due to very low S/N in that spectrum at the wavelengths of redshifted  $Ly\alpha$ ; the poor quality of the bluest portion of the COS/G130M spectrum is due to the presence of an unexpected Lyman limit system at higher redshift that absorbs the UV continuum. We do not model the  $5444 \text{ km s}^{-1}$  absorber in the PG 0832+251 sight line because the extremely broad, saturated  $Ly\alpha$  profile (Figure 4) does not allow us to reliably deconvolve individual H I components without higher-order Lyman-series lines (see Section A.1.4 for details). Finally, the  $22042 \text{ km s}^{-1}$  absorber in the PHL 1811 sight line is not modeled because we find evidence for only  $Ly\alpha$  and possible Si III absorption at this redshift in the high-S/N COS spectrum (Figure 4), leaving us with too few metal lines to meet our modeling criteria.

**Table 8.** UVB Model Comparison

Model Reference (1)	$\Gamma_0$ (2)	$J_0$ (3)	$\gamma$ (4)	$\delta$ (5)
Haardt & Madau (1996)	4.1	1.6	3.3	-0.8
Shull et al. (1999)	6.3	2.5	3.9	-0.4
Haardt & Madau (2001)	10.3	3.9	3.1	-0.9
Haardt & Madau (2005)	13.5	5.2	3.4	-0.7
Faucher-Giguère et al. (2009)	3.8	1.4	2.9	-1.1
Haardt & Madau (2012)	2.3	0.9	4.3	-0.1
Kollmeier et al. (2014)	11.5	4.4	4.3	-0.1
Shull et al. (2015)	4.6	1.7	4.4	-0.1
Khaire & Srianand (2015)	4.1	1.5	4.6	+0.1
Gaikwad et al. (2016)	3.9	1.4	5.0	+0.3

### 5.1. Effect of Ionizing Background

Before delving into the specifics of our photo-ionization models, a brief aside is warranted regarding the systematic effects that are coupled to the choice of ionizing radiation field. There has been considerable recent debate about the strength of the metagalactic UV ionizing background (UVB) at  $z \sim 0$  due to various theoretical models whose H I photo-ionization rates vary by a factor of  $\sim 6$  at  $z = 0$  (Haardt & Madau 1996, 2001, 2005, 2012; Shull et al. 1999, 2015; Faucher-Giguère et al. 2009; Kollmeier et al. 2014; Khaire & Srianand 2015; Madau & Haardt 2015; Gaikwad et al. 2016). We examine the nature of these models in Table 8, whose first four columns list: (1) the model reference; (2) the H I photo-ionization rate,  $\Gamma_{-14}$ , at  $z = 0$  in units of  $10^{-14} \text{ s}^{-1}$ ; (3) the specific intensity of Lyman continuum radiation,  $J_{-23}$ , at  $z = 0$  in units of  $10^{-23} \text{ erg cm}^{-2} \text{ s}^{-1} \text{ Hz}^{-1} \text{ sr}^{-1}$ ; and (4) a power-law index that describes how  $\Gamma_{-14}$  and  $J_{-23}$  evolve with redshift at  $z < 0.5$  (i.e.,  $\Gamma_{-14} = \Gamma_0(1+z)^\gamma$  and  $J_{-23} = J_0(1+z)^\gamma$ ).

All of these models, with the exceptions of Haardt & Madau (2001, 2005) and Kollmeier et al. (2014), are below observational limits on the UVB intensity at  $z = 0$  (Donahue et al. 1995; Adams et al. 2011, and see especially Figure 11 of Fumagalli et al. 2017). Additionally, all of these models evolve strongly at low redshift ( $\gamma \approx 3$ -5); however, there is variation in both normalization ( $\Gamma_0 \propto J_0$ ; see Equation 3) and power-law slope from model to model, which makes it non-trivial to compare quantities derived from CLOUDY photo-ionization models that assume different underlying UVB prescriptions.

Here we investigate the differences between these models using the cosmological simulations of Shull et al. (2015), which use a  $768^3$  grid that is  $50h^{-1} \text{ Mpc}$  on a side. This grid is then irradiated with the Haardt & Madau (2001, 2005, 2012) UVBs to study the relationship between baryon overdensity,  $\Delta_b$ , and H I column density for simulated absorbers with  $12.5 < \log N_{\text{HI}} < 15.5$ . This exercise has been performed by several groups using several different types of simulations (Davé et al. 2010; Tepper-García et al. 2012; Shull et al. 2015). While different groups find somewhat differ-

ent relationships between H I column and overdensity, the overall normalizations and power-law indices derived for a given ionizing background and redshift are remarkably robust given the other differences between the simulations (see discussion in Shull et al. 2015).

While Shull et al. (2015) were primarily interested in comparing the  $\Delta_b$ - $N_{\text{HI}}$  relationship for a given choice of UVB and redshift, here we attempt to quantify how different UVB intensities and power-law indices will affect the relation. We do so by measuring the overdensity in four different redshift bins from  $0 < z < 0.4$  for each choice of UVB (Haardt & Madau 2001, 2005, 2012). We expect the baryon overdensity to vary as

$$\Delta_b(z) \equiv \frac{\rho_b}{\langle \rho_b(z) \rangle} = \Delta_0(1+z)^{-3}\Gamma_{-14}^\beta N_{14}^\beta, \quad (1)$$

where  $\rho_b$  is the mass density of baryons,  $\langle \rho_b(z) \rangle \propto (1+z)^3$  is the mean baryon density at redshift  $z$ , and  $N_{14} = N_{\text{HI}}/(10^{14} \text{ cm}^{-2})$ . We expect  $\Gamma_{-14}$  and  $N_{\text{HI}}$  to scale with the same power-law index,  $\beta$ , so that an increase in H I photo-ionization rate will require a corresponding decrease in H I column to yield a constant overdensity value. The  $(1+z)^{-3}$  scaling implies that absorbers of a given column density exposed to a given photo-ionization rate exist at a constant physical density ( $\rho_b$ ) at all redshifts.

Adding in the redshift dependence of  $\Gamma_{-14}$ , we find

$$\Delta_b(z) = \Delta_0 \Gamma_0^\beta N_{14}^\beta (1+z)^{\beta\gamma-3}, \quad (2)$$

where  $\Gamma_0 \equiv \Gamma_{-14}(z=0)$  and  $\gamma$  are properties of the individual UVB model from Table 8, and  $\Delta_0$  and  $\beta$  are free parameters that hold for all choices of UVB in these simulations. We find that  $\Delta_0 \approx 10$  and  $\beta \approx 2/3$  yield values of  $\Delta_b$  that are within 5% of the measured values for the UVB specified by Haardt & Madau (2001, 2005) and within 20% of the measured values for the Haardt & Madau (2012) UVB. The final column of Table 8 lists  $\delta = \beta\gamma - 3 \approx (2\gamma - 9)/3$ , the power-law index that describes the evolution of  $\Delta_b$  with redshift, for each UVB model. Note that some of the UVBs predict very little evolution of  $\Delta_b$  with redshift because they are very close to the  $\gamma = 9/2$  value that corresponds to  $\delta = 0$  when  $\beta = 2/3$ .

We can now quantify the effects of the choice of UVB on the outputs and derived quantities from our CLOUDY photo-ionization models. The H I photo-ionization rate and the specific intensity of Lyman continuum radiation (columns 2 and 3 of Table 8) are related by

$$\Gamma_{\text{H}} = 4\pi \int_{\nu_0}^{\infty} \frac{J_\nu \sigma_\nu}{h\nu} d\nu \quad (3)$$

$$\Gamma_{-14} \approx 2.71 \left( \frac{4.4}{\alpha + 3} \right) J_{-23},$$

where  $\alpha$  is the power-law slope that characterizes the frequency dependence of the UVB. Recent measurements from *HST*/COS find  $\alpha \approx 1.4$  for AGN (Shull, Stevans, & Danforth 2012; Stevans et al. 2014), but the assumed value of  $\alpha$  varies somewhat for the models in Table 8 (from  $\alpha \approx 1.4$ -1.8).

The baryon overdensity is related to the total number den-



sity of hydrogen atoms,  $n_{\text{H}}$ :

$$\begin{aligned} n_{\text{H}} &= \frac{\rho_{\text{cr}}\Omega_{\text{b}}(1 - Y_{\text{p}})}{m_{\text{H}}}(1 + z)^3 \\ &= (1.89 \times 10^{-7} \text{ cm}^{-3})(1 + z)^3 \Delta_{\text{b}}(z), \end{aligned} \quad (4)$$

where the product  $\rho_{\text{cr}}\Omega_{\text{b}}$  is the baryon mass density at  $z = 0$  and  $Y_{\text{p}} = 0.2477$  is the primordial helium abundance (Peimbert, Luridiana, & Peimbert 2007). The ionization parameter,  $U$ , can then be derived once the number density of photons,  $n_{\gamma}$ , is known:

$$\begin{aligned} n_{\gamma} &= \frac{4\pi J_{\nu}}{hc\alpha} \\ &= (5.31 \times 10^{-8} \text{ cm}^{-3}) \left( \frac{\alpha + 3}{\alpha} \right) \Gamma_{-14} \end{aligned} \quad (5)$$

$$\begin{aligned} U &\equiv \frac{n_{\gamma}}{n_{\text{H}}} \\ &= 0.28 \left( \frac{\alpha + 3}{\alpha} \right) (1 + z)^{-3} \frac{\Gamma_{-14}}{\Delta_{\text{b}}(z)} \\ &= \frac{0.28}{\Delta_0} \left( \frac{\alpha + 3}{\alpha} \right) \Gamma_{-14}^{1-\beta} N_{14}^{-\beta}. \end{aligned} \quad (6)$$

The ratio  $(\alpha + 3)/\alpha \approx 3$  for all of the models in Table 8. Using this approximation and substituting the estimated values of  $\Delta_0 \approx 10$  and  $\beta \approx 2/3$  from above, we find

$$\begin{aligned} \log U &\approx 8.26 + 1/3 \log \Gamma_{-14} \\ &\quad - 2/3 \log (N_{\text{HI}} [\text{cm}^{-2}]). \end{aligned} \quad (7)$$

There are large uncertainties in the normalization of the UVB at  $z \approx 0$  (see Table 8). The most recent UVB models in Table 8 suggest that  $\Gamma_0 \approx 4$ . However, Figure 2 of Shull et al. (2015) indicates that a somewhat lower value, consistent with the Haardt & Madau (2012) UVB, is a better match to the column density distribution function of absorbers with  $N_{\text{HI}} > 10^{14} \text{ cm}^{-2}$  than the UVB models of Haardt & Madau (2001) or Haardt & Madau (2005)<sup>3</sup>. Since all but two of the cool CGM absorbers that we model have  $N_{\text{HI}} > 10^{14} \text{ cm}^{-2}$  (see Table 9), we choose to normalize the H I photo-ionization rate in our models to  $\Gamma_{-14} = 2.3$ , which is equivalent to the Haardt & Madau (2012) UVB at  $z = 0$ , and lower than any of the other UVB models in Table 8.

Below, we explicitly state the dependence on  $\Gamma_{-14}$  for all quantities derived from the ionization parameter to facilitate different choices in normalization.

## 5.2. Model Description and Results

In addition to the above differences in the specific absorbers modeled, we have also updated our modeling procedure. In Paper 1 we performed a strict maximum likelihood analysis comparing observed and modeled metal-line ratios (i.e., the ratio of the observed metal-line column densities to the H I column density), adopting the ionization pa-

rameter,  $U \equiv n_{\gamma}/n_{\text{H}}$ , and metallicity,  $Z_{\text{abs}}$ , that maximized the likelihood of simultaneously observing all of the modeled metal-line ratios as our ‘‘modeled’’ value. However, it is usually the case that the metal-line column densities are far better constrained than the H I column density, even if the formal uncertainty on  $N_{\text{HI}}$  is relatively small. This unhappy circumstance is primarily a consequence of the uncertainties inherent in deconvolving the component structure of saturated Ly $\alpha$  profiles when the only H I line available is Ly $\alpha$ . In Paper 1 we confronted this problem by restricting the ‘‘plausible’’ range of  $N_{\text{HI}}$  values for a given absorber to those which accommodated a single-phase photo-ionization solution with a line-of-sight thickness  $D_{\text{cl}} < \rho$  and metallicity  $Z_{\text{abs}} \lesssim Z_{\text{gal}}$  (this procedure is detailed in Keeney et al. 2013 and Davis et al. 2015).

Here we utilize a more principled tactic by assuming a Bayesian prior for the absorber ionization parameter and metallicity and adopting the unaltered H I column density from the Voigt profile fits<sup>4</sup>. Our prior on the absorber ionization parameter uses Equation 7 above, normalized to  $\Gamma_{-14} = 2.3$  (the H I photo-ionization rate at  $z = 0$  for the Haardt & Madau (2012) UVB; see Table 8). There is typically a factor of  $\sim 2$  scatter in the  $\Delta_{\text{b}}-N_{\text{HI}}$  relation at  $z \approx 0$  (e.g., see Figure 9 of Davé et al. 2010). We propagate this uncertainty along with the uncertainty on  $N_{\text{HI}}$  when determining the uncertainty on our prior for  $\log U$ . As in Paper 1, our prior on the absorber metallicity is that it is less than or equal to the galaxy metallicity; if the galaxy metallicity was estimated from the mass-metallicity relations of Tremonti et al. (2004) or Lee et al. (2006), our metallicity prior assumes a  $1\sigma$  uncertainty of 0.5 dex.

As in Keeney et al. (2013) and Davis et al. (2015), we model the absorbers using a plane-parallel grid of CLOUDY models (Ferland et al. 1998) irradiated by the Haardt & Madau (2012) UVB at  $z = 0$ . Our models assume solar abundance ratios (Grevesse et al. 2010) and vary the absorber metallicity in the range  $\log Z_{\text{abs}} = -3$  to 1 in solar units by steps of 0.2 dex, and the ionization parameter in the range  $\log U = -5$  to 1 by steps of 0.2 dex.

Column densities of H I and all metal lines commonly seen in low- $z$  FUV quasar absorption line systems are calculated at each grid point, from which model metal-line ratios are calculated. Before comparing these ratios with the observed metal-line ratios of our absorption line systems, we linearly interpolate the model values to a finer resolution of 0.01 dex in both  $\log U$  and  $\log Z_{\text{abs}}$ . For each species,  $X$ , the log-likelihood of a given point in this interpolated grid,  $i$ , is assumed to be

$$\ln \mathcal{L}_i^X = -0.5 \left( \frac{r_i^X - r^X}{\sigma^X} \right)^2, \quad (8)$$

where  $r_i^X$  is the model metal-line ratio (i.e.,  $N_X/N_{\text{HI}}$ ) at

<sup>3</sup> Haardt & Madau (2001) and Haardt & Madau (2005) are more consistent with the number of absorbers with  $N_{\text{HI}} \approx 10^{13} \text{ cm}^{-2}$ , but none of the Haardt & Madau models are a good fit to absorbers with  $N_{\text{HI}} = 10^{13.5}$  to  $10^{14} \text{ cm}^{-2}$ .

<sup>4</sup> Since the H I column density at a particular velocity can be strongly dependent on the number of velocity components used to fit saturated Ly $\alpha$  profiles this does not remove all subjective bias from the analysis. We have endeavored to make sensible, consistent choices in all of our fits (Section 3) but in many cases a similar fit quality can be achieved with several combinations of the number and location of velocity components.

point  $i$ ,  $r^X$  is the observed metal-line ratio, and  $\sigma^X$  is the uncertainty in the observed metal-line ratio, which takes into account the uncertainties in both  $N_X$  and  $N_{\text{HI}}$ .

For metal-line detections, calculating the metal-line ratio and its associated uncertainty is straightforward, but the proper treatment of upper limits is less clear. Our approach is to treat the metal-line upper limits as step functions in probability; i.e., all column densities less than the  $3\sigma$  limit listed in Table 3 are equally likely (with probability = 1), as are all column densities above the listed limit (with probability = 0). However, since we are modeling ratios of metal-line column densities with respect to  $N_{\text{HI}}$  we need to take into account uncertainty in the H I column density,  $\sigma_{\text{HI}}$ . We do this by convolving the discontinuous likelihood predicted when  $\sigma_{\text{HI}} = 0$  with a Gaussian kernel having  $\sigma = \sigma_{\text{HI}}$ , which we then use to evaluate  $\mathcal{L}_i^X$  for each  $r_i^X$  in the interpolated grid.

Finally, the posterior probability at point  $i$  is determined using

$$\ln P_i = \ln \Pi_i + \sum_x \ln \mathcal{L}_i^x, \quad (9)$$

where  $\Pi_i$  is the prior at point  $i$  and the sum is performed over all species that are modeled. We then identify the interpolated grid points that maximize the marginal posterior probability for  $\log U$  and  $\log Z_{\text{abs}}$ , and adopt the 68.3% highest posterior density credible interval as the uncertainty in the model parameters.

There are also several quantities that we derive from the model parameters. The absorber density,  $n_{\text{H}}$ , is given by

$$\log (n_{\text{H}} [\text{cm}^{-3}]) = -6.80 + \log \Gamma_{-14} - \log U. \quad (10)$$

The mean pressure in the absorber is defined as

$$\begin{aligned} \log \langle P/k \rangle &= \log (n_{\text{H}} [\text{cm}^{-3}]) + \log T \\ &= -6.80 + \log T + \log \Gamma_{-14} - \log U, \end{aligned} \quad (11)$$

where  $T$  is the equilibrium temperature ( $\approx 10^4$  K) output from CLOUDY along with the model column densities, and subsequently interpolated onto the same fine grid. The neutral fraction,  $f_{\text{HI}}$ , is given by

$$\begin{aligned} \log f_{\text{HI}} &= 4.73 - 0.76 \log T - \log \Gamma_{-14} \\ &\quad + \log (n_{\text{H}} [\text{cm}^{-3}]) \\ &= -2.07 - 0.76 \log T - \log U. \end{aligned} \quad (12)$$

The H I column density and neutral fraction determine the total hydrogen column:

$$N_{\text{H}} = N_{\text{HI}} (1 + f_{\text{HI}}^{-1}) \approx N_{\text{HI}}/f_{\text{HI}}. \quad (13)$$

The absorber line-of-sight thickness,  $D_{\text{cl}}$ , is defined as

$$\begin{aligned} \log (D_{\text{cl}} [\text{kpc}]) &= -21.5 + \log (N_{\text{H}} [\text{cm}^{-2}]) \\ &\quad - \log (n_{\text{H}} [\text{cm}^{-3}]) \\ &= -12.6 + 0.76 \log T - \log \Gamma_{-14} + 2 \log U \\ &\quad + \log (N_{\text{HI}} [\text{cm}^{-2}]) \end{aligned} \quad (14)$$

and its hydrogen + helium mass,  $M_{\text{cl}}$ , is given by

$$\begin{aligned} \log (M_{\text{cl}} [M_{\odot}]) &= 7.24 + \log n_{\text{H}} \\ &\quad + 3 \log (D_{\text{cl}} [\text{kpc}]) \\ &= -37.4 + 2.28 \log T - 2 \log \Gamma_{-14} \\ &\quad + 5 \log U + 3 \log (N_{\text{HI}} [\text{cm}^{-2}]). \end{aligned} \quad (15)$$

Equation 15 assumes a uniform cloud density, a spherical cloud geometry, and a primordial helium abundance of  $Y_p = 0.2477$  (Peimbert et al. 2007).

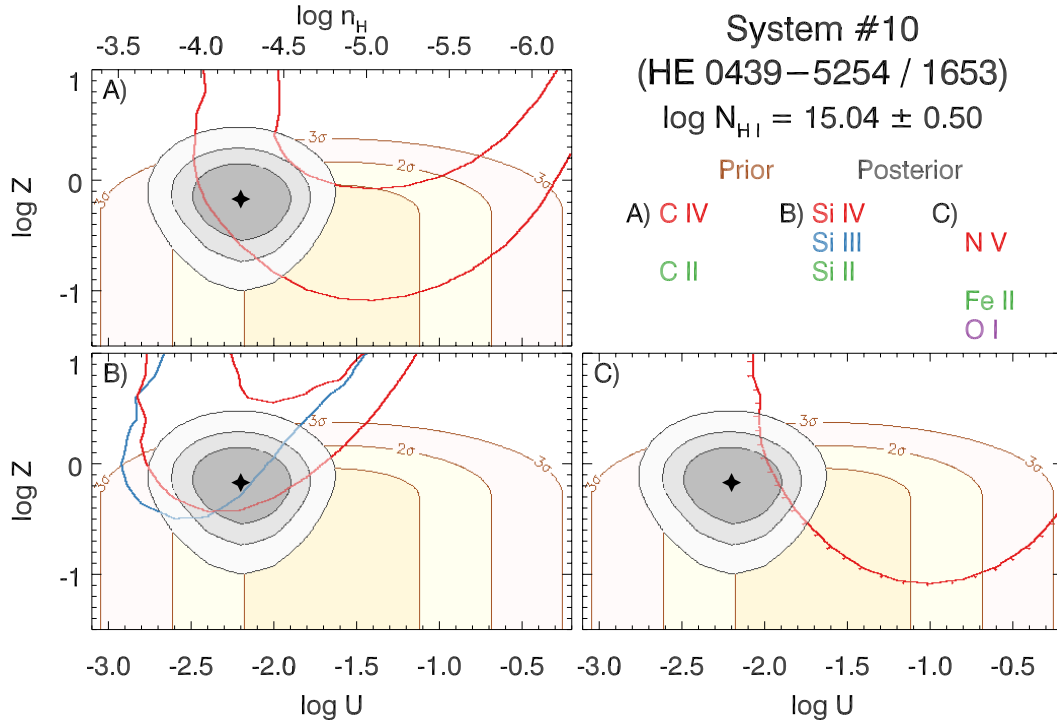
The results of our photo-ionization modeling are summarized in Table 9, which lists the following information by column: (1) the running system number of the absorber from Table 3; (2) the quasar sight line name; (3) the Ly $\alpha$  absorption velocity in  $\text{km s}^{-1}$ ; (4) a subjective grade that indicates our relative confidence in the photo-ionization model for this absorber (see discussion in Section 6); (5) the logarithm of the absorber's H I column density, in  $\text{cm}^{-2}$ ; (6) the logarithm of the absorber ionization parameter,  $U$ ; (7) the logarithm of the absorber metallicity,  $Z_{\text{abs}}$ , in solar units; (8) the logarithm of the mean absorber pressure,  $\langle P/k \rangle$ , in  $\text{cm}^{-3}$  K; (9) the logarithm of the line-of-sight cloud thickness,  $D_{\text{cl}}$ , in kpc; and (10) the logarithm of the cloud mass,  $M_{\text{cl}}$ , in  $M_{\odot}$ . Columns 11-13 of Table 9 reproduce the H I column density, ionization parameter, and absorber metallicity, respectively, for absorbers modeled in Table 6 of Paper 1.

The photo-ionization models for all absorbers in Table 9 are shown in Figure 6. Each model is depicted by three panels; the beige and gray contours, which represent the prior and posterior probability distributions for a given absorber, are identical in all three panels. Panel ‘‘A’’ shows all of the carbon ions used to constrain the model, Panel ‘‘B’’ shows all of the silicon ions, and Panel ‘‘C’’ shows everything else (sundry ions of oxygen, nitrogen, and iron). Metal-line detections are indicated with solid  $1\sigma$  contours enclosing the allowable region of parameter space, and  $3\sigma$  upper limits are shown with tick marks pointing toward the allowable region of parameter space. Contour lines are color coded to match the legend (e.g., red contours in Panel ‘‘A’’ signify constraints from C IV measurements). If an ion is listed in the legend but not seen in the corresponding panel (e.g., C II in Panel ‘‘A’’ for System 10, or Si II in Panel ‘‘B’’) then the limit is not stringent enough to meaningfully constrain the model. The filled star symbol is located at the peaks of the marginal distributions for  $\log U$  and  $\log Z_{\text{abs}}$  (i.e., columns 6 and 7 of Table 9).

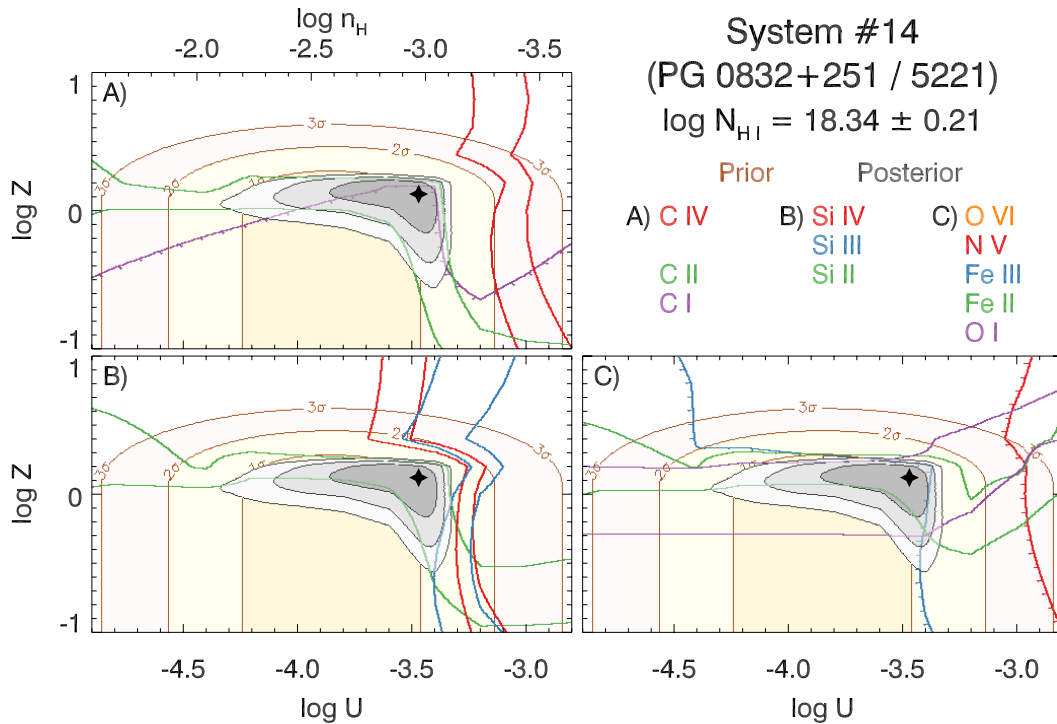
**Fig. Set 5. CLOUDY Photo-Ionization Models**

**Table 9.** CLOUDY Modeling Results

System	Sight Line	$z_{\text{abs}}$	Grade	$\log N_{\text{HI}}$	$\log U$	$\log Z_{\text{abs}}$	$\log(P/k)$	$\log D_{\text{cl}}$	$\log M_{\text{Cl}}$	$\log N_{\text{HI}}$	$\log U$	Stocke et al. (2013)	
												$\log N_{\text{HI}}$	$\log U$
(1)	(2)	(3)	(4)	(5)	(6)	(7)	(8)	(9)	(10)	(11)	(12)	(13)	
10	HE 0439-5254	1653	C	$15.04 \pm 0.50$	$-2.20^{+0.20}_{-0.18}$	$-0.17^{+0.20}_{-0.21}$	$-0.0^{+0.2}_{-0.3}$	$+0.8^{+0.6}_{-0.6}$	$5.5^{+1.6}_{-1.6}$	$15.21 \pm 0.44$	$-2.4^{+0.3}_{-0.2}$	$+0.1^{+0.9}_{-0.4}$	
14	PG 0832+251	5221	C	$18.34 \pm 0.21$	$-3.47^{+0.08}_{-0.26}$	$+0.12^{+0.08}_{-0.11}$	$+0.9^{+0.3}_{-0.1}$	$+1.3^{+0.2}_{-0.8}$	$8.3^{+0.2}_{-2.1}$	$18.48 \pm 0.17$	$-3.5^{+0.2}_{-0.2}$	$-0.5^{+0.2}_{-0.2}$	
17	PG 0832+251	5444	...	...	...	...	...	...	...	$16.39 \pm 0.91$	$-2.4^{+0.4}_{-0.5}$	$-0.9^{+0.7}_{-0.5}$	
19	PMN J1103-2329	1194	C	$14.76 \pm 0.16$	$-2.20^{+0.10}_{-0.16}$	$+0.35^{+0.12}_{-0.16}$	$-0.3^{+0.3}_{-0.2}$	$+0.4^{+0.3}_{-0.4}$	$4.1^{+0.8}_{-1.1}$	$15.94 \pm 0.47$	$-2.2^{+0.4}_{-0.5}$	$-0.8^{+0.5}_{-0.4}$	
21	RX J0439.6-5311	1674	C	$15.53 \pm 0.43$	$-2.36^{+0.17}_{-0.17}$	$-0.63^{+0.26}_{-0.25}$	$+0.2^{+0.2}_{-0.2}$	$+1.1^{+0.6}_{-0.6}$	$6.4^{+1.5}_{-1.6}$	$15.41 \pm 0.42$	$-2.6^{+0.4}_{-0.4}$	$-0.3^{+0.6}_{-0.5}$	
23	SBS 1108+560	654	...	...	...	...	...	...	...	$17.38 \pm 0.63$	$-3.1^{+0.4}_{-0.4}$	$0.0^{+1.0}_{-0.5}$	
25	SBS 1108+560	778	...	...	...	...	...	...	...	$15.44 \pm 0.42$	$-2.3^{+0.3}_{-0.3}$	$-0.5^{+0.3}_{-0.3}$	
26	SBS 1122+594	1221	B	$15.94 \pm 0.47$	$-2.30^{+0.15}_{-0.15}$	$-0.29^{+0.14}_{-0.21}$	$+0.1^{+0.2}_{-0.2}$	$+1.6^{+0.5}_{-0.5}$	$7.8^{+1.2}_{-1.4}$	$15.92 \pm 0.42$	$-2.5^{+0.4}_{-0.4}$	$-0.2^{+0.3}_{-0.3}$	
27	VII Zw 244	715	B	$15.22 \pm 0.28$	$-2.47^{+0.10}_{-0.10}$	$+0.19^{+0.16}_{-0.14}$	$+0.0^{+0.2}_{-0.2}$	$+0.3^{+0.3}_{-0.3}$	$4.2^{+0.7}_{-0.8}$	$15.81 \pm 0.26$	$-2.8^{+0.1}_{-0.2}$	$-0.2^{+0.1}_{-0.2}$	
102	3C 273	1585	A	$15.49 \pm 0.05$	$-3.22^{+0.05}_{-0.02}$	$-0.48^{+0.13}_{-0.09}$	$+0.9^{+0.1}_{-0.1}$	$-0.8^{+0.2}_{-0.1}$	$1.5^{+0.5}_{-0.3}$	$15.85 \pm 0.09$	$-3.2^{+0.2}_{-0.1}$	$-0.9^{+0.2}_{-0.2}$	
115	PG 0953+414	42664	B	$13.53 \pm 0.02$	$-1.48^{+0.12}_{-0.12}$	$+0.01^{+0.09}_{-0.08}$	$-0.7^{+0.1}_{-0.1}$	$+0.9^{+0.5}_{-0.4}$	$4.9^{+1.2}_{-1.0}$	...	...	...	
123	PG 1116+215	41522	A	$15.95 \pm 0.03$	$-3.09^{+0.04}_{-0.04}$	$-0.19^{+0.07}_{-0.08}$	$+0.7^{+0.1}_{-0.1}$	$-0.2^{+0.2}_{-0.2}$	$3.4^{+0.3}_{-0.3}$	$16.35 \pm 0.10$	$-3.3^{+0.1}_{-0.1}$	$-0.3^{+0.1}_{-0.2}$	
126	PG 1211+143	15321	A	$15.54 \pm 0.06$	$-2.74^{+0.13}_{-0.14}$	$-0.24^{+0.08}_{-0.07}$	$+0.4^{+0.2}_{-0.3}$	$+0.2^{+0.6}_{-0.4}$	$4.1^{+1.4}_{-1.1}$	$15.67 \pm 0.35$	$-2.9^{+0.5}_{-0.3}$	$-0.5^{+0.3}_{-0.4}$	
130	PG 1211+143	19305	B	$15.31 \pm 0.04$	$-2.20^{+0.05}_{-0.06}$	$-0.93^{+0.08}_{-0.09}$	$+0.1^{+0.1}_{-0.1}$	$+1.2^{+0.2}_{-0.2}$	$6.7^{+0.5}_{-0.5}$	$15.17 \pm 0.10$	$-2.4^{+0.1}_{-0.2}$	$-0.9^{+0.1}_{-0.1}$	
132	PG 1211+143	19481	D	$13.29 \pm 0.17$	$-1.24^{+0.25}_{-0.26}$	$+0.58^{+0.21}_{-0.18}$	$-0.9^{+0.2}_{-0.2}$	$+1.1^{+0.9}_{-0.9}$	$5.3^{+2.3}_{-2.4}$	$13.82 \pm 0.05$	$-2.1^{+0.1}_{-0.1}$	$-0.2^{+0.2}_{-0.1}$	
137	PG 1216+069	37049	B	$14.57 \pm 0.05$	$-2.02^{+0.05}_{-0.06}$	$+0.39^{+0.09}_{-0.07}$	$-0.5^{+0.1}_{-0.2}$	$+0.5^{+0.2}_{-0.2}$	$4.5^{+0.3}_{-0.5}$	...	...	...	
138	PG 1216+069	37138	B	$14.76 \pm 0.05$	$-2.11^{+0.06}_{-0.06}$	$-0.06^{+0.06}_{-0.07}$	$-0.2^{+0.1}_{-0.1}$	$+0.7^{+0.2}_{-0.2}$	$5.1^{+0.5}_{-0.5}$	...	...	...	
142	PG 1259+593	13825	A	$15.45 \pm 0.04$	$-2.36^{+0.06}_{-0.06}$	$-0.61^{+0.06}_{-0.06}$	$+0.2^{+0.1}_{-0.1}$	$+1.0^{+0.2}_{-0.2}$	$6.1^{+0.5}_{-0.5}$	$15.51 \pm 0.28$	$-2.2^{+0.3}_{-0.9}$	$-1.1^{+0.9}_{-0.3}$	
143	PG 1259+593	13914	A	$14.60 \pm 0.05$	$-1.78^{+0.10}_{-0.12}$	$-0.46^{+0.09}_{-0.08}$	$-0.3^{+0.1}_{-0.1}$	$+1.4^{+0.3}_{-0.4}$	$6.6^{+0.8}_{-1.1}$	$14.75 \pm 0.38$	$-1.7^{+0.3}_{-1.3}$	$-0.6^{+0.8}_{-0.5}$	
148	PHL 1811	22042	...	...	...	...	...	...	...	$14.88 \pm 0.09$	$-2.7^{+0.3}_{-0.2}$	$-0.3^{+0.2}_{-0.3}$	
149	PHL 1811	23313	A	$15.40 \pm 0.07$	$-3.05^{+0.03}_{-0.02}$	$-0.15^{+0.06}_{-0.08}$	$+0.6^{+0.1}_{-0.1}$	$-0.6^{+0.1}_{-0.1}$	$1.9^{+0.4}_{-0.3}$	$14.94 \pm 0.08$	$-2.7^{+0.2}_{-0.2}$	$-0.2^{+0.4}_{-0.2}$	
152	PHL 1811	24226	C	$18.08 \pm 0.04$	$-3.65^{+0.08}_{-0.18}$	$-0.25^{+0.07}_{-0.07}$	$+1.2^{+0.1}_{-0.1}$	$+0.8^{+0.2}_{-0.2}$	$6.9^{+0.6}_{-1.8}$	$18.00 \pm 0.50$	$-3.5^{+0.3}_{-0.9}$	$-0.7^{+0.8}_{-1.4}$	
153	PHL 1811	39658	D	$14.61 \pm 0.01$	$-1.37^{+0.19}_{-0.20}$	$-0.99^{+0.12}_{-0.11}$	$-0.6^{+0.2}_{-0.2}$	$+2.3^{+0.7}_{-0.7}$	$9.1^{+1.6}_{-1.7}$	...	...	...	
157	PHL 1811	52933	B	$14.84 \pm 0.04$	$-2.37^{+0.12}_{-0.12}$	$-0.57^{+0.09}_{-0.08}$	$+0.2^{+0.1}_{-0.1}$	$+0.4^{+0.4}_{-0.4}$	$4.2^{+0.6}_{-0.9}$	$14.87 \pm 0.03$	$-2.6^{+0.5}_{-0.5}$	$-0.5^{+0.4}_{-0.5}$	
170	PKS 0405-123	50059	B	$15.41 \pm 0.06$	$-2.92^{+0.05}_{-0.06}$	$+0.30^{+0.07}_{-0.07}$	$+0.2^{+0.1}_{-0.1}$	$-0.5^{+0.2}_{-0.2}$	$2.1^{+0.5}_{-0.6}$	...	...	...	
171	PKS 0405-123	50104	B	$16.45 \pm 0.02$	$-3.16^{+0.03}_{-0.03}$	$-0.24^{+0.08}_{-0.07}$	$+0.7^{+0.1}_{-0.1}$	$+0.2^{+0.1}_{-0.1}$	$4.6^{+0.4}_{-0.3}$	$16.45 \pm 0.07$	$-3.0^{+0.1}_{-0.1}$	$+0.1^{+0.2}_{-0.2}$	
175	PKS 1302-102	12655	A	$14.91 \pm 0.08$	$-2.82^{+0.06}_{-0.04}$	$+0.03^{+0.06}_{-0.06}$	$+0.4^{+0.1}_{-0.1}$	$-0.7^{+0.2}_{-0.1}$	$1.5^{+0.6}_{-0.1}$	$14.83 \pm 0.17$	$-2.8^{+0.1}_{-0.1}$	$+0.2^{+0.2}_{-0.2}$	
178	PKS 1302-102	28439	A	$17.11 \pm 0.03$	$-3.30^{+0.04}_{-0.04}$	$-1.26^{+0.14}_{-0.15}$	$+1.0^{+0.1}_{-0.1}$	$+0.7^{+0.2}_{-0.1}$	$6.1^{+0.4}_{-0.4}$	$17.10 \pm 0.40$	$-3.1^{+0.5}_{-0.3}$	$-1.7^{+0.6}_{-0.4}$	
187	Q 1230+0115	23404	C	$14.77 \pm 0.07$	$-2.16^{+0.11}_{-0.12}$	$-0.13^{+0.11}_{-0.10}$	$-0.1^{+0.2}_{-0.2}$	$+0.6^{+0.3}_{-0.4}$	$4.9^{+0.8}_{-1.0}$	$15.06 \pm 0.40$	$-2.2^{+0.4}_{-0.7}$	$-0.2^{+0.4}_{-0.4}$	



5.1: Photo-ionization model of the  $1653 \text{ km s}^{-1}$  absorber in the HE 0439–5254 sight line, which is associated with the targeted galaxy ESO 157–49 (Section A.2.4).



5.2: Photo-ionization model of the  $5221 \text{ km s}^{-1}$  absorber in the PG 0832+251 sight line, which is associated with the targeted galaxy NGC 2611 (Section A.2.6).

**Figure 6.** CLOUDY photo-ionization models for all absorbers in Table 9. Metal-line detections are indicated with solid  $1\sigma$  contours enclosing the allowable region of parameter space, and  $3\sigma$  upper limits are shown with tick marks pointing toward the allowable region of parameter space. Panel A shows the carbon ions, Panel B shows the silicon ions, and Panel C shows everything else, color coded by species. The prior and posterior distributions for a given absorber are identical in all three panels. The complete figure set (25 images) is available in the online journal.

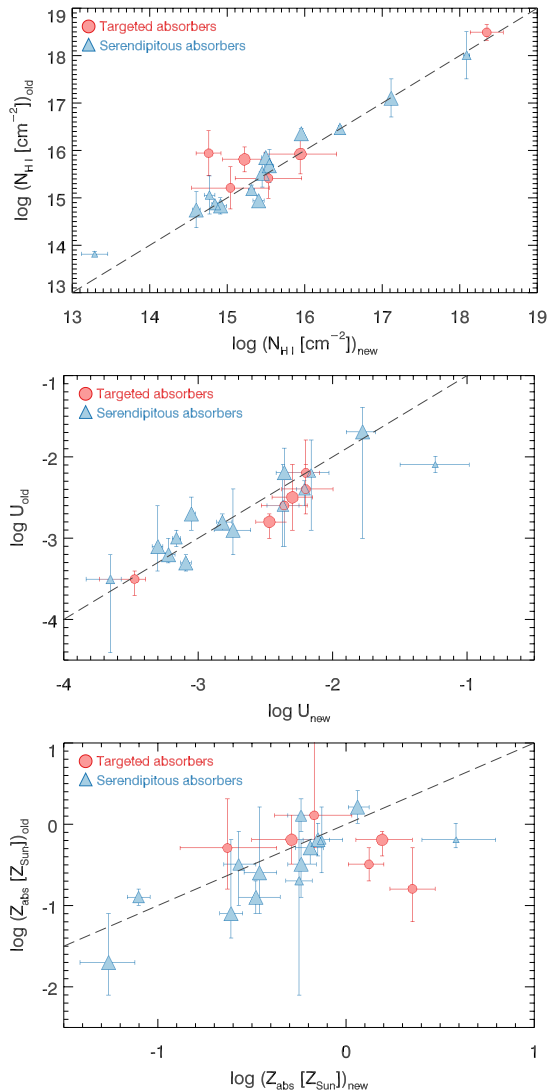


**Figure 7.** *Top:* Comparison of updated values of  $\log N_{\text{HI}}$  (“new”; see column 5 of Table 9) with the values adopted in Paper 1 (“old”; see column 11 of Table 9). *Middle:* Comparison of updated values of  $\log U$  with the values adopted in Paper 1. *Bottom:* Comparison of updated values of  $\log Z_{\text{abs}}$  with the values adopted in Paper 1. In all panels, the dashed line indicates perfect agreement between the two values. Symbol size is indicative of our confidence in the photo-ionization models (i.e., our absorber grades; see Section 6) with higher-confidence absorbers having larger plot symbols. The H I column densities and ionization parameters typically agree well, but our updated absorber metallicities are somewhat higher than the values found in Paper 1.

In the subsections below we compare the results in Table 9 with those presented in Paper 1 (Section 5.3) and with the photo-ionization models of the COS-Halos absorbers (Werk et al. 2014, Section 5.4). Generally speaking, our photo-ionization models are robust to our choice of Bayesian prior (i.e., running the models with and without a prior yield very similar results); individual models where this conclusion does not hold are detailed in Section A.3 of the Appendix.

### 5.3. Comparison with Photo-Ionization Results of Paper 1

We find that the values of  $N_{\text{HI}}$ ,  $U$ , and  $Z_{\text{abs}}$  that we derive here are generally in good agreement with the values

published in Paper 1, except that we tend to find somewhat higher absorber metallicities in our updated analysis. Plots of the “old” values from Paper 1 versus the “new” values from our updated analysis can be found in Figure 7. There are some exceptions to the general agreement in  $N_{\text{HI}}$  and  $U$  between the two analyses, however, which we detail in the Appendix, Section A.3, where appropriate. We also find no clear trends in absorber line-of-sight thickness, mass or mean pressure as a function of nearest galaxy luminosity or  $\rho/R_{\text{vir}}$ , again consistent with the results of Paper 1. Updated plots of these distributions are shown in Figure 8. These conclusions hold even if we restrict our analysis to the subset of absorbers for which we have the highest confidence in photo-ionization models (i.e., grade A absorbers).

### 5.4. Comparison with COS-Halos Photo-Ionization Models

Werk et al. (2014) presented photo-ionization models of 44 COS-Halos absorbers, finding that the circumgalactic gas traced by these absorbers tends to become more highly ionized and less dense with increasing distance from the nearest galaxy. We compare the results of our updated photo-ionization models to the best-fit relations of Werk et al. (2014) in Figure 9, where the top panel shows ionization parameter as a function of  $N_{\text{HI}}$ , the middle panel shows ionization parameter as a function of normalized impact parameter, and the bottom panels show total hydrogen volume and column density, respectively, as a function of normalized impact parameter. Our models assume a Bayesian prior for  $U(N_{\text{HI}})$  (see Equation 7), which is shown with the filled contours in the top panel.

All panels have a solid line with a dotted extrapolation that shows the best-fit relation from Werk et al. (2014). In the top panel, the slope of the Werk et al. (2014) relation differs from the slope assumed by our Bayesian prior (see Section 5.1), but most of our values are in reasonable agreement with those of Werk et al. (2014). The Werk et al. (2014) parameterization of ionization parameter as a function of normalized impact parameter also provides a reasonable description of our data both inside and outside of the region probed by COS-Halos ( $\rho \lesssim 0.5 R_{\text{vir}}$ ), albeit with large scatter. The Werk et al. (2014) fits to the total hydrogen volume and column densities, however, lay well above the bulk of our data points; we attribute this difference to the different assumed UVB models, a point we will return to in Section 6.1.

Thus, we conclude that the basic results of our photo-ionization models and those of Werk et al. (2014) are in good agreement. Where we differ is in their interpretation. While Werk et al. (2014) find increasing ionization state and decreasing hydrogen density as a function of normalized impact parameter at  $2\sigma$  significance, our photo-ionization results (Figure 9) are consistent with constant values of ionization parameter and total hydrogen density (i.e., no change with distance from the nearest galaxy). These slightly differing results may be due to the different normalized impact parameter ranges (i.e.,  $\rho/R_{\text{vir}} < 0.5$  for Werk et al. 2014 and  $\rho/R_{\text{vir}} \approx 0.5\text{-}2.0$  for the present sample).

This hypothesis is supported by Figure 3, which shows the distribution of total CGM  $N_{\text{HI}}$  (i.e., the sum over all

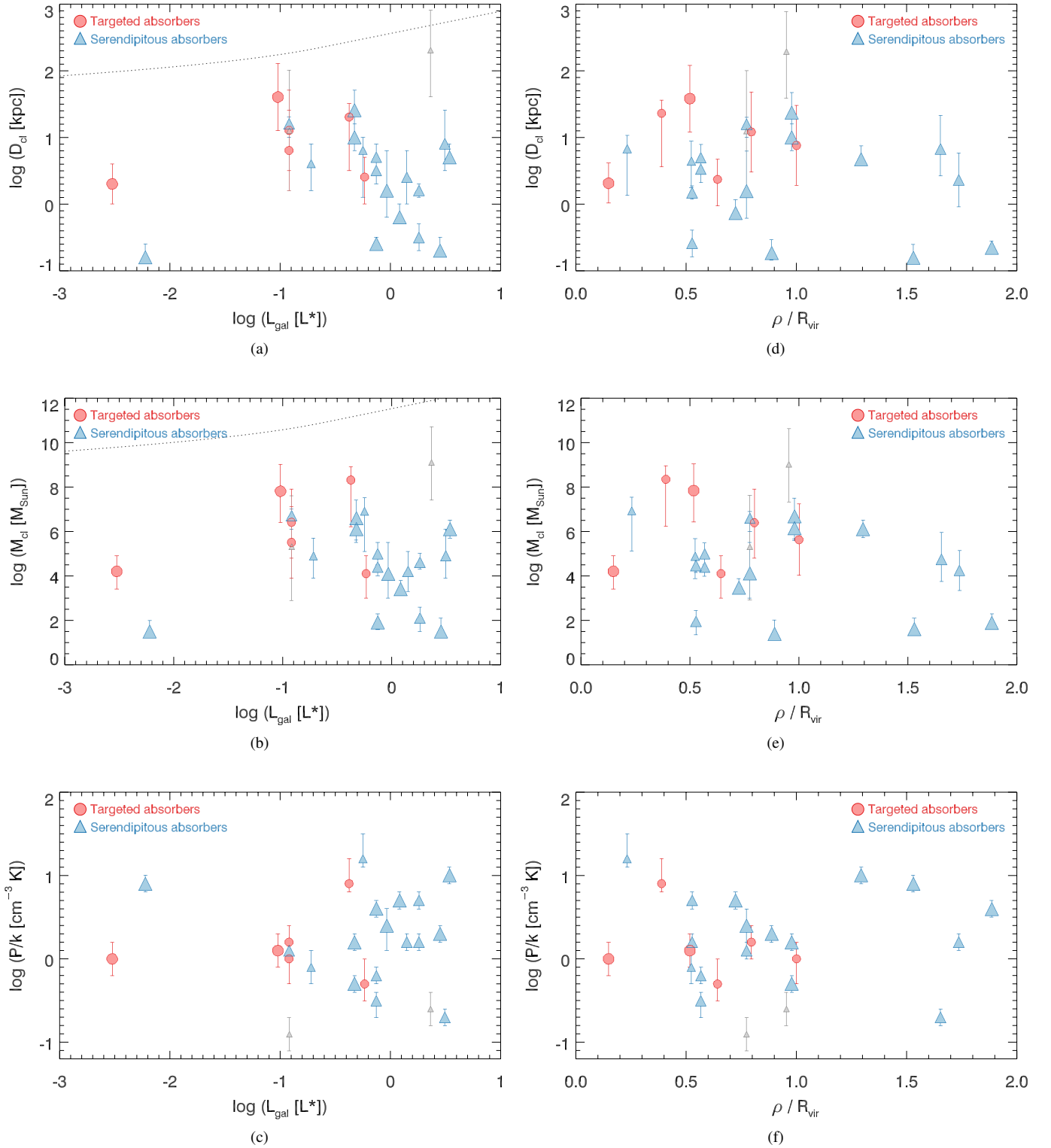


**Figure 8.** Distributions of  $D_{\text{cl}}$ ,  $M_{\text{cl}}$  and  $(P/k)$  as a function of nearest galaxy luminosity (Panels a-c) and normalized impact parameter (Panels d-f). As in Figure 7, symbol size is indicative of our confidence in the photo-ionization models (i.e., our absorber grades) with higher-confidence absorbers having larger plot symbols; the two grade D absorbers are colored gray. No obvious trends are present in any of the panels, in agreement with Figures 12-14 of Paper 1. The dotted lines in Panels a-b shows the galaxy's virial diameter and mass, respectively, as a function of luminosity.

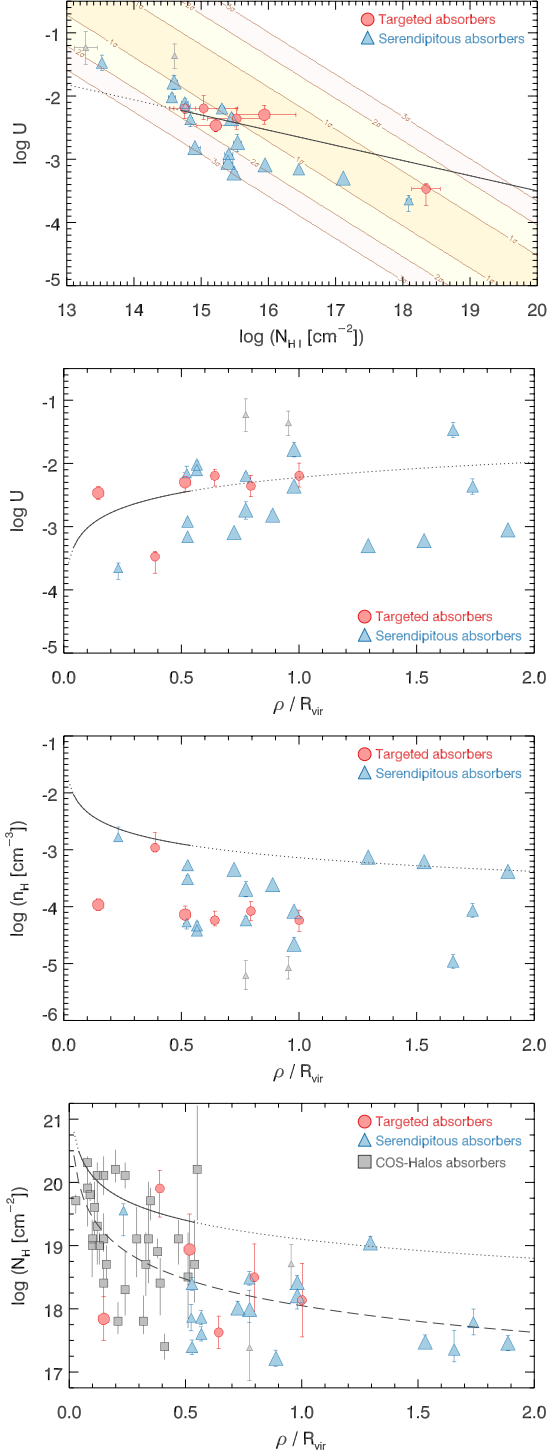


**Figure 9.** Distributions of model parameters as a function of  $N_{\text{HI}}$  and normalized impact parameter for our updated photo-ionization models. These models assume a Bayesian prior for ionization parameter as a function of  $N_{\text{HI}}$ , which is shown as  $1\sigma$ ,  $2\sigma$  and  $3\sigma$  contours in the top panel. Each panel has a solid line with a dotted extrapolation that shows the relationship found by [Werk et al. \(2014\)](#) for COS-Halos absorbers. As in [Figure 7](#), symbol size is indicative of our confidence in the photo-ionization models, with higher-confidence absorbers having larger plot symbols. The dashed line in the bottom panel is our power-law fit to the combined targeted, serendipitous, and COS-Halos data, and is described in [Section 5.4](#).

velocity components associated with a particular galaxy) as a function of normalized impact parameter. We have overplotted the COS-Halos measurements from Table 1 of [Werk et al. \(2014\)](#) for direct comparison with our values. The gray squares show the “adopted” values of  $N_{\text{HI}}$  and the vertical gray lines indicate the full range of values allowed by the data. There is excellent agreement in the small range of normalized impact parameter where our sample and COS-Halos overlap, and the addition of the COS-Halos values makes the trend of increasing  $N_{\text{HI}}$  with decreasing  $\rho/R_{\text{vir}}$  evident. A least-squares fit to the combined targeted, serendipitous, and COS-Halos data finds

$$N_{\text{HI}} = 10^{14.8 \pm 0.1} \left( \frac{\rho}{R_{\text{vir}}} \right)^{-2.7 \pm 0.3} \text{ cm}^{-2}. \quad (16)$$

This parameterization is shown as the dashed line in [Figure 3](#). A more sophisticated analysis that allows the COS-Halos values of  $N_{\text{HI}}$  to vary uniformly over the entire allowable range finds nearly identical results.

A similar result is found in the bottom panel of [Figure 9](#), which shows total hydrogen column,  $N_{\text{H}}$ , as a function of normalized impact parameter for our sample and COS-Halos. Again the “adopted” values of [Werk et al. \(2014\)](#) are shown with gray squares, and the full range of  $N_{\text{H}}$  by vertical gray lines. While the correlation is not as strong as in [Figure 3](#), the bottom panel of [Figure 9](#) nevertheless suggests that our data and the COS-Halos data can be described by a single power law. A least-squares fit to the combined data finds

$$N_{\text{H}} = 10^{18.0 \pm 0.3} \left( \frac{\rho}{R_{\text{vir}}} \right)^{-1.4 \pm 0.3} \text{ cm}^{-2}. \quad (17)$$

This parameterization is shown as the dashed line in the bottom panel of [Figure 9](#). A more sophisticated analysis that allows the COS-Halos  $N_{\text{H}}$  values to vary over their full allowed range again finds very similar results. The power-law slope of this fit is consistent within errors with the parameterization of [Werk et al. \(2014\)](#) for COS-Halos data, but the normalization is an order of magnitude lower, a  $\sim 2\sigma$  discrepancy. [Werk et al. \(2014\)](#) justify their use of this high normalization to account for saturated H I lines, for which they have only lower limits on  $N_{\text{HI}}$ ; a very recent paper by [Prochaska et al. \(2017\)](#) presents new observations providing better  $N_{\text{HI}}$  values, some but not all of which are higher than the lower limits of [Werk et al. \(2014\)](#), see [Figure 3](#) of [Prochaska et al. \(2017\)](#). Despite the hint of a discontinuity between our  $N_{\text{H}}$  values and those of COS-Halos at  $\rho \sim 0.5 R_{\text{vir}}$ , independent fits to the two data sets do not find statistically significant variations in normalization or power-law slope.

In addition to the differing impact parameter ranges probed, another clear distinction between the COS-Halos sample and ours is that the COS-Halos sight lines were chosen to probe  $L \approx L^*$  galaxies at  $z \approx 0.2$ , whereas our targeted and serendipitous samples probe a wide range of galaxy luminosities (see [Figure 1](#)) at  $z \lesssim 0.2$ . Thus, the fact that the targeted and serendipitous absorbers in [Figures 7-9](#) are relatively well-mixed and are reasonably fit by the best-fit relations derived from COS-Halos absorbers suggests that the luminosity of the nearest galaxy does not have a signifi-

cant effect on the derived circumgalactic absorption properties (see Section 6).

## 6. CGM ENSEMBLE PROPERTIES

In the full complement of  $\sim 50$  Ly $\alpha$  absorbers associated with galaxies studied here, 28% of them are found to be multiple velocity component absorbers defined as being in a single galaxy CGM by virtue of being within  $\pm 400$  km s $^{-1}$  of the galaxy redshift. Most of these multiple systems have Ly $\alpha$  lines that are highly saturated and blended, which makes determining their basic properties problematical for three reasons. First, deblending of multiple components is an uncertain process usually made less subjective by employing a  $\chi^2$  minimization of a multiple-component Voigt profile fit. Priors sometimes are set based on the velocity locations of metal-ion absorptions, which often are separated more distinctly than Ly $\alpha$  since these lines are intrinsically narrower. Even this, now rather standard, process (e.g., [Werk et al. 2012](#); [Savage et al. 2014](#); [Danforth et al. 2016](#)) assumes that the individual velocity components are well-modeled by Voigt profiles, that the metal lines align well in velocity with the H I absorptions and that small differences in the resulting  $\chi^2$  values are meaningful. Nevertheless, for the present analysis we have used the procedures outlined in [Danforth et al. \(2016\)](#) for multiple component fitting. This procedure differs from the process employed in Paper 1 by which these complexes were assumed to be a single, although complex, absorber associated with a single galaxy’s CGM. Values and associated uncertainties for the absorption line fits are found in Table 3.

Secondly, standard analysis procedures for saturated Ly $\alpha$  lines (e.g., apparent optical depth; [Savage & Sembach 1991](#)) provide only lower limits on H I column density. If higher order Lyman lines are available, a simultaneous line-fit or curve-of-growth (CoG) analysis can provide a much more secure  $N_{\text{HI}}$  value. For the serendipitous sample, CoG analyses are possible for most absorbers due to the availability of *FUSE* spectra of these bright AGN targets. For the targeted sample, the higher-order H I lines are not available (since *FUSE* spectra are not available excepting for a poor, short exposure of PG 0832+251) for study and any saturated Ly $\alpha$  lines yield uncertain  $N_{\text{HI}}$  values<sup>5</sup>. Comparing the physical cloud parameters for targeted absorbers compared to serendipitous absorbers finds no large differences between these two samples, but the  $N_{\text{HI}}$  values for many absorbers in the targeted sample remain uncertain as indicated in Table 9. Uncertain values of  $N_{\text{HI}}$  are one criterion used to determine the reliability of the results from the CLOUDY modeling of these absorbers (see below).

Thirdly, the basic geometry of these Ly $\alpha$  complexes is unclear even if the line deconvolution is straightforward. Is each velocity component a separate cool CGM cloud? This interpretation means that 13 galaxy CGMs probed here have 3 or 4 clouds found along the line of sight. Different ve-

locity components in these complexes may even be associated with different nearby galaxies (see Section 7.2). Or are these differing velocity structures within the same CGM cloud? Paper 1 implicitly assumed the latter interpretation which led to a modest “shadowing factor” of  $S = 1.4$ , in which there are few sight lines with multiple clouds in a single CGM but some of these clouds have complex velocity distributions. On the other hand, the multi-component line deconvolution shown in the COS spectra in Figure 4 yields a larger value of  $S = 2.0$  by assuming that these velocity components are all separate clouds. This shadowing factor ( $S$ ) was introduced and defined in Paper 1 and is the mean number of discrete clouds found along any one sight line within a single galaxy CGM (i.e., the number of clouds “shadowed” by another cloud from our perspective). The median number of discrete clouds along these sight lines is also 2, with 28% (13) of the CGMs studied having 3 or 4 clouds along the line-of-sight. For reference, the completely independent evaluation of the shadowing factor for the COS-Halos project by [Werk et al. \(2014\)](#) finds  $S = 2.4$ ; i.e., most COS-Halos sight lines have multiple detections in a single galaxy CGM. We discuss sample differences in the next subsection that might account for the difference in shadowing factors obtained between these two studies.

The new Ly $\alpha$  line deconvolutions performed here and shown in Figure 4 for these complex absorbers could make, at least in principle, a significant difference in the ensemble CGM properties compared to those obtained by Paper 1, including the total filling factor and mass of the cool gas in the CGM. The basic procedure to obtain these quantities (see Paper 1 for details) is to use those CGM absorbers that have multiple ionization states of the same element (e.g., Si II, Si III and Si IV) as representative of the full CGM cool cloud population, which may or may not be a true assumption. This is related to a basic unstated assumption of both this study and COS-Halos that the methodology of using single QSO sight line probes of many galaxies provides a statistically accurate picture of the CGM of any one galaxy with similar properties (e.g., super- $L^*$ , star-forming galaxies). This assumption is implicitly made when we calculate ensemble CGM properties in this Section. The percentage of absorbers at  $\rho \leq R_{\text{vir}}$  for which CLOUDY modeling is available is high, 12 of 15 (see below), so the physical parameters found are a reasonable approximation to the full CGM sample. We take the virial radius to be the full extent of the CGM despite some uncertainty ([Shull 2014](#)).

In order to make the best ensemble mass estimate from the current, modest-sized sample, we have graded the absorbers A through D in decreasingly well-constrained values for ionization parameter ( $U$ ) and thus cloud density, size and mass. This letter grade uses both the S/N of the metal-line detections which constrain the CLOUDY modeling and the accuracy of the  $N_{\text{HI}}$  value based on the availability and S/N of the higher-order Lyman lines. Grades A (8 absorbers) and B (9 absorbers) include absorbers with high-S/N detections in metal-lines and multiple Lyman line detections providing accurate CoG  $N_{\text{HI}}$  values. Grade B absorbers are slightly less well-constrained in  $U$  and  $N_{\text{HI}}$  than grade A

<sup>5</sup> In most cases, a single Ly $\alpha$  line fit tends to under-predict the  $N_{\text{HI}}$  for moderate and stronger H I absorption ( $\log N_{\text{HI}} \gtrsim 13.5$ ; [Danforth et al. 2010](#)).



absorbers by having either lower S/N metal-line detections or somewhat inconsistent constraints in the CLOUDY modeling. Grade C absorbers (6 absorbers) have less accurate  $N_{\text{HI}}$  values either due to being Ly $\alpha$ -only detections (targeted absorbers) or poor CoG solutions that could be due to blending of higher order Lyman lines in the FUSE band. However, many grade C absorbers have good metal-line detections which yield good constraints on ionization parameter, particularly constraining against high values of  $\log U$  (see e.g., the CLOUDY model in Section 5 for the absorber PG 0832+251/5221). Grade D absorbers (2 absorbers) lack both accurate  $N_{\text{HI}}$  values and also accurate  $U$  determinations, with no strong constraints against high values of  $U$ . For example, the absorber PHL 1811/39658 has weak detections of only C III 977 ( $4\sigma$ ) with FUSE and the C IV doublet ( $3.0$  and  $2.5\sigma$ ) with COS. Not only is  $N_{\text{HI}}$  poorly constrained in this case but the very weak and uncertain metal-line detections lead to a very uncertain  $\log U$  value. We do not use the two grade D absorbers in our ensemble mass calculations. Our best estimates for ensemble properties use absorbers with grades A-C, thus maximizing the sample size without significantly degrading the quality of the result.

Our modeling process assumes a single, homogeneous gas phase for the metal-enriched clouds, for which a CLOUDY (Ferland et al. 1998) photo-ionization model is constructed. These models (see Section 5) determine cloud density from the resulting value of the ionization parameter assuming a meta-galactic UV ionizing spectrum at  $z = 0$  as specified by Haardt & Madau (2012) for all absorbers, since our sample is at low-redshift (see Section 5 for justification of this choice). The Haardt & Madau (2012) UV background best reproduces the low-redshift H I column density distribution (Danforth et al. 2016) for  $\log N_{\text{HI}} > 14$  (Shull et al. 2015), where almost all CGM absorbers are detected. Given the presence of varying ionization states, this modeling relies primarily on the lower ions to provide the ionization parameter since the higher ionization states may be influenced by some collisional ionization.

As mentioned in Paper 1, the absorbers in this sample are well outside any “proximity distance” where the ionizing flux which leaks out from the nearby galaxy exceeds the meta-galactic ionizing flux from QSOs (Giroux & Shull 1997). This calculation assumes that a very high (probably unrealistically high) fraction of ionizing radiation escapes from the nearby galaxy ( $\langle f_{\text{esc}} \rangle = 5\%$ ), in order to determine a quite conservative estimate for the maximum proximity distance for each absorber based on the nearest galaxy’s current SFR (Giroux & Shull 1997). Since all of our absorbers are well outside this distance, the meta-galactic ionizing flux is assumed to be isotropic in our CLOUDY modeling.

The internal temperature and thus pressure of these clouds is also determined from the CLOUDY model (see details in Paper 1 and Section 5). The derived pressures shown in the bottom panels of Figure 8 vary considerably around a mean value of  $\langle P/k \rangle = 2 \text{ cm}^{-3} \text{ K}$ , a value which is  $\sim 0.7$  dex lower than the mean value reported in Paper 1. This is largely due to an error in Paper 1 that overestimated the cloud pressure by a factor of  $\approx 5$ .

The calculated cloud density together with the observed H I column density and neutral fraction determine the line-of-sight cloud thickness,  $D_{\text{cl}}$ . These cloud sizes range from 150 pc to 40 kpc (see Table 9 and Figure 8). The smallest cloud sizes are quite close to the minimum size suggested to survive in the CGM over a long timescale ( $\geq 250$  Myr) by Armillotta et al. (2016); the largest cloud sizes are nearly a factor of ten larger than the largest HVC found near the Milky Way (Complex C; Wakker et al. 2007). While there is one CLOUDY solution (for the absorber PHL 1811/39658) that suggests a cloud size still larger ( $\sim 200$  kpc) this absorber has a very poorly constrained photo-ionization model (grade D). Therefore, we discount this absorber’s model and suggest a largest cloud size of  $\sim 40$  kpc (covering about 2% of the entire CGM when viewed from afar).

Assuming spherical symmetry allows a mass estimate for each cloud modeled. Individual cloud mass estimates can be quite uncertain ( $\sigma(M_{\text{cl}}) \sim 30\text{-}50\%$ ) due to uncertainties in the CLOUDY modeling (including the possible presence of multi-phase gas), to uncertainties in the H I column density when the Ly $\alpha$  is saturated and/or blended, and to the substantial sensitivity of the calculated mass to the line-of-sight thickness from which it is derived ( $M_{\text{cl}} \propto D_{\text{cl}}^3$ ). In this sample, cloud masses range from  $30 M_{\odot}$  to  $2 \times 10^8 M_{\odot}$ , the latter value being over two orders of magnitude more massive than Complex C (Wakker et al. 2007). These cloud mass estimates are listed in Table 9 and shown in Figure 8.

The CLOUDY models for components of the complex absorbers yield smaller line-of-sight cloud sizes and masses compared to Paper 1. As inferred by the photo-ionization analysis these absorption complexes break up into smaller (3-10 kpc) clouds that have estimated cloud masses of  $10^5$ - $10^{6.5} M_{\odot}$ . This increases the shadowing factor and the filling factor, which increases the total CGM ensemble mass. But dividing very massive absorbers into separate clouds has the effect of decreasing the total CGM mass estimate because, in the limit of unity covering factor, the few most massive clouds dominate the total filling factor and the ensemble mass. By this new analysis method for the complex absorbers, the total filling factors are 1.5 times greater for all luminosity classes than as given in Paper 1 (see their Table 7); e.g., 5-9% for super- $L^*$  galaxies.

In calculating the ensemble CGM cool gas mass we have followed the procedure described in detail in Paper 1 in which the number of clouds ( $N_{\text{cl}}$ ) in each half-dex size range is determined from the covering factor ( $C$ ), shadowing factor ( $S$ ), virial radius of the associated galaxy ( $R_{\text{vir}}$ ) and cloud size ( $R_{\text{cl}}$ ) by the following equation, which was derived in Paper 1:

$$N_{\text{cl}} = C S \left( \frac{R_{\text{vir}}}{R_{\text{cl}}} \right)^2. \quad (18)$$

The ensemble mass in each mass bin is then  $M_{\text{tot}} = N_{\text{cl}} M_{\text{cl}}$ ; for this calculation we have assumed that the CGM extends to the virial radius of these galaxies (but see Shull 2014) and used the clouds associated with both the super- $L^*$  and sub- $L^*$  subsamples (as in Paper 1) as representative of bulk CGM properties for galaxies in both of these luminosity subsamples, since the covering and shadowing factors for each sub-

sample are nearly identical. While the dwarfs have far fewer detected clouds, that subsample also has much lower covering factors ( $C$ ) within the virial radius ( $C \sim 1/2$ ), and much larger associated errors. Also as in Paper 1, we have divided the CGM into volumes defined by the inner and outer half-radii as the covering factor declines slightly between these two impact parameters. Three-quarters of the CGM mass is inside  $1/2 R_{vir}$ . The ensemble cold cloud numbers and mass in each luminosity subsample are determined using the mean virial radius for each subsample (see Paper 1).

The combination of larger filling factors and larger numbers of modest-mass clouds (factor of nearly twice more in the  $\sim 10^5$ - $10^{6.5} M_\odot$  range) leaves our best estimate for the ensemble cool CGM mass nearly unchanged at  $\log(M/M_\odot) = 10.2 \pm 0.3$  for super- $L^*$  galaxies, identical (but with slightly larger uncertainty) to the value presented in Table 7 of Paper 1. This best estimate uses all 23 absorbers with data and CLOUDY modeling quality of A, B and C grades. If only the best quality A- and B-grade absorbers are used, this sample of 17 absorbers finds  $\log(M/M_\odot) = 10.4 \pm 0.4$ . The larger uncertainty is due to the smaller number of large (20-30 kpc), massive ( $> 10^{6.5} M_\odot$ ) clouds in the full ensemble (3 vs 5). Using only grade A absorbers finds a similar mean mass estimate but with a much larger uncertainty due to the smaller sample of massive clouds. Almost all of the CGM clouds detected at  $\rho \leq R_{vir}$  by this survey are modeled in this process; 12 of 15 absorbers have metals and almost all of them are modeled in Section 5. Since there are no obvious differences in basic properties (e.g.,  $N_{HI}$  values) between those few unmodeled clouds and the large majority of modeled clouds, the above estimate of ensemble CGM cool cloud mass likely is unbiased by the absence of models for these few.

The error budget for this CGM ensemble mass estimate is substantial. Since the ensemble mass estimates are dominated by a small number of the largest clouds, the sampling errors are large,  $\sim 50\%$ . But then there are also systematic errors associated with the CLOUDY modeling itself, due both to uncertainties in individual metal-line measurements and to the detailed methodology in constructing the best-fit models based on those ratios (see Section 5). These errors are reflected in the individual uncertainties associated with cloud line-of-sight thicknesses and masses recorded in Table 9. Despite the statistical gain of averaging many modeled clouds, the errors due to modeling uncertainties are comparable to the sampling errors, leading to total errors in the ensemble mass estimate of 0.3 dex.

Even with this increase in uncertainty, our ensemble super- $L^*$  galaxy CGM mass estimate of  $\log(M/M_\odot) = 10.2 \pm 0.3$  is substantially lower than the COS-Halos “preferred lower limit” of  $\log(M/M_\odot) \geq 10.8$  (Werk et al. 2014) at the  $2\sigma$  level. The COS-Halos estimate is presented as a firm lower limit on CGM mass due to saturated H I absorption lines in their sample. However, a COS-Halos calculation similar to the one performed above and in Paper 1 obtains a total CGM cool gas mass of  $\log(M/M_\odot) = 10.5$ ,  $1\sigma$  higher than the value obtained here and in Paper 1. A more recent study of CGM gas structure using a hierarchi-

cal, photo-ionized cloud structure to explain the various ionization states including O VI finds a total cool gas mass of  $\log(M/M_\odot) = 10.1 \pm 0.1$  (Stern et al. 2016). The Stern et al. (2016) study also finds covering factors and filling factors for Ly $\alpha$  and the low ions comparable to the values we found in Paper 1 and herein. An even more recent paper (Prochaska et al. 2017) extends the Werk et al. (2014) analysis by obtaining better  $N_{HI}$  values for COS-Halos absorbers with highly-saturated Ly $\alpha$ . This new work suggests a total cool CGM mass of nearly  $10^{11} M_\odot$ , at even greater variance to the value obtained herein. We critique these various CGM cool gas mass estimates in the next subsection.

In both the current study and the COS-Halos study, the cool CGM ensemble cloud mass is dominated by the few very large clouds with line-of-sight thicknesses of  $\geq 10$  kpc and estimated masses  $\geq 10^{6.5} M_\odot$ . Werk et al. (2014) find even larger, more massive clouds with estimated line-of-sight thicknesses of up to 2 Mpc. These cloud sizes are so large that even Werk et al. (2014) question whether inferred sizes can be as large as this, since 2 Mpc is considerably larger than the virialized region of an  $L^*$  galaxy. Excluding a very poorly-constrained (grade D) CLOUDY solution for one absorber that yields a line-of-sight thickness of  $\sim 200$  kpc, the largest cloud thicknesses we find in the current study are 20-40 kpc, which yield inferred cloud masses of  $10^7$ - $10^8 M_\odot$ .

Are even these large cloud sizes reasonable or just the result of unsuspected systematics in the CLOUDY modeling? The recent discovery by Davis et al. (2015) leaves little doubt that large size ( $\geq 10$ -20 kpc) cool CGM clouds can exist. Davis et al. (2015) found H I and/or C IV absorption common to a close triplet of QSO sight lines (“The LBQS Triplet”; Crighton et al. 2010) at the redshift of a very nearby, star-forming  $0.07 L^*$  spiral. While the physical structure of clouds this large is not clear, Davis et al. (2015) set a firm lower limit of  $\geq 10^6 M_\odot$  on the mass of this cloud. And if the mean ionization parameter from the present study is adopted for these absorbers, then the inferred mass of this cloud is  $\geq 10^7 M_\odot$ . Further research on the internal, physical structure of CGM clouds will provide a much more secure ensemble mass for the cool phase of galaxy halos, a work which is now in progress in Cycle 23 of HST observations (Guest Observer Program #14127, M. Fumagalli, PI; see also Bowen et al. 2016).

### 6.1. Systematics and the Estimated Baryon Content of the Cool CGM

The ensemble cool CGM cloud mass determination is important for taking an accurate census of spiral galaxy baryons and assessing the status of the “missing baryon” problem. Since the most obvious physical condition for this “missing” gas is in the hard-to-detect  $T = 10^5$ - $10^{6.5}$  K range (but see Savage et al. 2014; Stocke et al. 2014; Werk et al. 2016; Prochaska et al. 2017), at present its amount can best be calculated indirectly by totaling those baryon reservoirs that are more easily detectable and assuming a total baryon reservoir set by the universal dark matter to baryon ratio. This hypothesized hotter gas is suggested by simulations (e.g., Klypin et al. 2001; Faerman, Sternberg, & McKee 2016) to be massive

enough to be the dominant baryon reservoir in spiral galaxies with an extent comparable to a small, spiral-rich group in which individual star-forming galaxies reside (Stoche et al. 2014; Faerman et al. 2016). A hot intra-group medium is also suggested for spiral-rich galaxy groups by downward extrapolation from the more massive halos of elliptical-dominated groups (Mulchaey 2000) and by some (but not all) observational analyses of the Local Group gas (e.g., Anderson & Bregman 2011; Gupta et al. 2012; Faerman et al. 2016).

While data and analysis limitations make all current estimates uncertain to a factor of  $\sim 2$ , the different results presented in the previous paragraph suggest substantial differences in the number of “missing baryons”. The Werk et al. (2014) COS-Halos “preferred lower limit” amounts to  $\geq 30\%$  of the baryons in spiral galaxies. And the recent Prochaska et al. (2017) reanalysis of the COS-Halos absorbers finds  $\approx 50\%$  while the ensemble mass estimated here and in Paper 1 yield 10-15% baryon fraction. The Stern et al. (2016) formalism finds baryon fractions at the  $\leq 10\%$  level while admitting that their assumed hierarchical cloud structure minimizes a total mass estimate. While the lower limit found by Werk et al. (2014) and the value quoted by Prochaska et al. (2017) are 4-5 times higher than the amount found herein, the COS-Halos galaxies are suggested to be in twice-higher-mass halos, so the baryon fractions calculated differ by a factor of 2-2.5. Using nominal values (see Table 8 in Paper 1) obtained by other studies for the  $L^*$  spiral galaxy baryon percentages in stars and gas in the spiral disk ( $\sim 20\%$ ), hotter O VI-absorbing gas in the CGM ( $\sim 6\%$ ), and very hot ( $T > 10^7$  K) coronal gas ( $\leq 10\%$ ), then the Werk et al. (2014) lower limit on cool CGM mass implies that  $\geq 2/3$  of all spiral galaxy baryons have been found; i.e., currently detected and identified in emission and/or absorption. The most recent Prochaska et al. (2017) paper suggests that, between the cool and hot CGM masses, all the baryons in spiral halos may have been located. On the other hand, if the value derived herein, in Paper 1, and in the Stern et al. (2016) analysis is used, then  $\geq 1/2$  of spiral galaxy baryons remain “missing”. While these differences are large, they are only somewhat greater than the combined statistical errors of these various analyses.

While we have quoted statistical errors on our mass estimates, important systematic differences exist between the COS-Halos studies and this one. Most importantly is the value of the ionization rate assumed to be impinging on these clouds because derived cloud densities, and thus cloud masses, are determined from the CLOUDY modeling, which uses an assumed meta-galactic ionizing spectrum. The use of different values quoted in the most recent works (Haardt & Madau 2001, 2012; Kollmeier et al. 2014; Khaire & Srianand 2015; Shull et al. 2015; Madau & Haardt 2015; Gaikwad et al. 2016) can add  $\geq \pm 0.3$  dex of *systematic* uncertainty to the total (i.e., ionization-corrected) hydrogen column, and a greater systematic uncertainty to the computed mass, depending on method used. Additional systematic bias occurs when studying absorbers at different redshifts due to the very steep dependence of the H I ionization rate ( $\Gamma_{\text{H}}$ ) on redshift

(see Section 5.1). Our use of the H I photo-ionization rate at  $z = 0$  as compared to a  $\sim 25\%$  larger value at  $z = 0.05$  (the median redshift of our sample) has very little effect on the estimated cloud masses. However, Werk et al. (2014) and Prochaska et al. (2017) assume a much more intense radiation field that amounts to a factor of  $\sim 3-4$  times larger ionization rate, when corrected back to  $z = 0$  from the mean COS-Halos absorber redshift of  $z = 0.2$ . The Haardt & Madau (2012, HM12 hereafter) UVB spectrum is assumed for this conversion from  $z = 0.2$  to  $z = 0$ . We assert that it is this difference in assumed ionization rate (Haardt & Madau (2001, HM01 hereafter) at  $z = 0.2$  assumed by Werk et al. 2014 and Prochaska et al. 2017, and HM12 at  $z = 0$  assumed herein) that leads to the cloud densities in this survey (i.e., largely at  $\rho > 0.5 R_{\text{vir}}$ ) appearing to be lower than the COS-Halos cloud densities at slightly smaller impact parameters (see Figure 9; bottom two panels). Using the results found in Shull et al. (2015) (see their Table 1 & Figure 2), for a given  $N_{\text{H}}$ , the neutral fraction is  $\sim 0.6$  dex higher for the HM12 spectrum than for the HM01 spectrum. By Equation 8 in Werk et al. (2014) and Equation 7 in Prochaska et al. (2017) this  $\approx 4$  times larger  $N_{\text{H}}$  for a given  $N_{\text{HI}}$  translates directly into a  $\approx 4$  times larger total CGM cool gas mass. This difference can be seen in the bottom panels of Figure 9, in which the Werk et al. (2014) fits to cloud densities are significantly higher than the current data; some of the Prochaska et al. (2017) inferred cloud densities are even higher (see their Figure 8, right-hand panels).

Ultimately, the correct value of the H I ionization rate is not known at present, particularly at low- $z$  (although see very recent work on  $\text{H}\alpha$  fluorescence in clouds at  $z \approx 0$  that may rule out the HM01 ionization rate; Fumagalli et al. 2017, see also Donahue et al. 1995). We justify our use of the HM12 spectrum through the detailed analysis of various ionization rates presented in Shull et al. (2015), which included a comparison with observed column density distributions (see their Figure 2). What is striking in this Figure is that the low-H I column density distribution is well-matched using the earlier HM01 UVB, but the higher H I column densities are much better matched by the HM12 background. While none of the UVB spectra match the *slope* of the observed column density distribution, the origin of this discrepancy remains a mystery. And what is the best match at  $\log N_{\text{HI}} > 14.5$  is also not clear. But, since the CGM absorbers are all at higher column densities, the choice of the HM12 spectrum appears to be the most appropriate for CGM studies at this time.

As reported in Paper 1 and herein, none of the present sample of absorbers occurs so close to the nearest galaxy that the ionizing flux impinging on the cloud becomes dominated by the escaping Lyman continuum radiation from the nearby galaxy; i.e., all of the absorbers in the present sample have impact parameters larger than the “proximity distance” for a rather high assumed escape fraction of ionizing photons of 5% (Giroux & Shull 1997). However, using the SFRs and impact parameters for COS-Halos absorbers found in Werk et al. (2013) we find that 18 out of 28 of the COS-Halos absorbers lie at impact parameters less than the proximity distance for a more plausible escape fraction of 2%. Both be-

cause the impact parameter is a projected distance and because the leakage of ionizing photons is very likely to be highly anisotropic in star-forming galaxies, only a fraction of the 18 absorbers actually may have their photo-ionization rate dominated by UV photons from the nearby galaxy. Still, if this occurs even in just a few cases the under-estimation of the ionizing flux for these absorbers can lead to an under-estimate of the cloud density for the ionization parameter set by the metal-line ratios in the absorber. If this “proximity effect” is present for some COS-Halos absorbers, it means that COS-Halos has *under*-estimated the ionization rate in these cases. But, even if present, this is likely to be a small effect (Werk et al. 2014 came to this same conclusion) since the solid angle illumination of a CGM cloud by the nearby galaxy is modest at CGM cloud distances, and much smaller than the isotropic UVB impinging on the cloud.

While there may be differences between these two mass estimates due to assumed ionizing radiation field levels, there are definitely differences in the radial domain of applicability of these results as described in Section 2.1 and shown in Figures 1 and 2. Briefly, the COS-Halos study has no data at all at  $\gtrsim 1/2 R_{\text{vir}}$ , while the present study has very little data at  $\leq 1/2 R_{\text{vir}}$  compared with COS-Halos (7 absorbers only from this study, all of which have CLOUDY models). Therefore, one could argue that these studies are largely disjoint and thus complementary and cannot be easily compared due to the quite different radial distribution of impact parameters. For example, the analysis of Prochaska et al. (2017) suggests that the CGM cool gas mass has converged in the COS-Halos data and there is little to no CGM beyond  $\rho \geq 0.5 R_{\text{vir}}$ . This conclusion is based on a cloud column density distribution which declines quickly with impact parameter, truncating at an impact parameter of 160 kpc. On the other hand, at larger impact parameters, the present study finds no significant correlation between  $N_{\text{HI}}$  and impact parameter. In the current sample there are quite a few metal-bearing, high- $N_{\text{HI}}$  absorbers at  $\rho \geq 0.5 R_{\text{vir}}$ , including metal-line detections in absorbers beyond the virial radius (Figure 13, and Figures 8 & 9 in Paper 1). Paper 1 finds  $\approx 25\%$  of the cool CGM between  $0.5\text{-}1 R_{\text{vir}}$ , at variance with the Prochaska et al. (2017) conclusion.

On the other hand, if the COS-Halos choice of the HM01 ionization is adopted, then a total CGM cool gas mass inside the virial radius of slightly greater than  $10^{11} M_{\odot}$  is obtained. If the twice larger halo mass calibration of Prochaska et al. (2011a) is used (see Figure 1 in Stocke et al. 2013), the baryon fraction of the CGM cool gas mass exceeds 50%. While it is beyond the scope of this paper to decide which ionization rate and halo mass calibration are correct, we favor a lower value of the CGM cool gas mass both because the HM01 ionization rate appears to be ruled out by recent low- $z$  H $\alpha$  fluorescence observations (Adams et al. 2011; Fumagalli et al. 2017) and because a larger reservoir of hot, compared to cool, gas mass is expected around star-forming galaxies in small galaxy groups (Klypin et al. 2001; Faerman et al. 2016, see also Stocke et al. 2014 for relevant observations). High-S/N HST/COS observations of QSO probes through small galaxy groups are now in progress (cycle 23; J. Stocke, PI

to search for broad, shallow O VI and Ly $\alpha$  absorption associated with this hotter gas.

Since there is only a small overlap in radial domain between our sample and COS-Halos, one can argue that to obtain the best total CGM cool gas mass estimate, these values should be added. But in this case we need to renormalize the COS-Halos mass estimate for  $\rho < 1/2 R_{\text{vir}}$  to the HM12 ionization rate at  $z = 0.2$ . For the most recent Prochaska et al. (2017) mass estimate this yields:  $\log(M/M_{\odot}) = 10.4 \pm 0.3$  for the inner CGM. This renormalized value is now within the statistical errors of our mass estimate here and in Paper 1. For the outer CGM we take 25% of the CGM calculated herein from Paper 1. We make no correction in this calculation for the larger halo mass galaxies in the COS-Halos studies compared to the sample herein; i.e., we use a total halo mass appropriate for a  $2 L^*$  galaxy from Paper 1 and here. In this case the total CGM cool gas mass estimate obtained is:  $\log(M/M_{\odot}) = 10.5 \pm 0.3$ ,  $1\sigma$  higher than our estimate. This amounts to a cool CGM baryon fraction of  $\sim 30\%$ , twice the value obtained from our data alone.

In conclusion, while this study updates and slightly revises the ensemble CGM properties of star-forming galaxies, the new values obtained are nearly indistinguishable from the findings of Paper 1. Specifically, for this sample alone, the ensemble CGM mass calculation finds the same values as Paper 1 for all three luminosity bins. Since the difference between this study and Paper 1 is how the multi-component Ly $\alpha$  absorbers are handled, the cool CGM mass calculation appears to be robust with respect to the detailed data analysis process used for the multi-component absorber complexes that dominate the CGM cool cloud mass. Additionally, the ensemble cool CGM mass of  $\log(M/M_{\odot}) = 10.2 \pm 0.3$  obtained herein and in Paper 1 is identical to within statistical errors with the recent result of Stern et al. (2016), which uses a much more specific model for cloud structure. This suggests that the mass calculation is also robust with respect to the detailed structure assumed for these clouds and the cool CGM gas mass constitutes a significant, but still minority, contribution (10-15%) of the spiral galaxy baryon inventory.

However, the COS-Halos study better samples the inner half of the virial radius of massive spirals, while the current study better samples the outer half. After renormalizing the COS-Halos mass estimate to the less intense ionization rate and smaller total halo mass appropriate for our sample, the estimated baryon fraction in the cool CGM gas is 30%, twice the value quoted above. Given all the statistical and systematic uncertainties, we consider this baryon fraction to be the most accurate estimate currently.

## 7. DISCUSSION

### 7.1. Galaxy-Absorber Correlations

#### 7.1.1. Metal-line Detections and Nondetections

In this Section we examine basic correlations between galaxies and their CGM absorbers. Figures 10 and 11 compare histograms of H I column density and absorber-galaxy radial velocity difference, respectively, for absorbers with and without metals. The top panel of both Figures compares absorbers that exhibit absorption from any metal species with

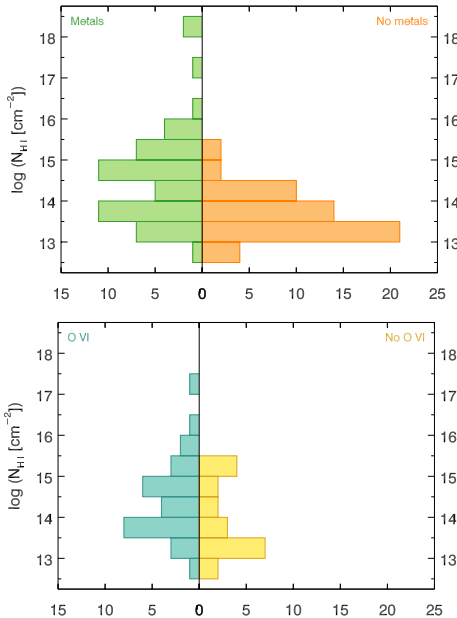


**Figure 10.** Distribution of H I column density for absorbers with and without metals (top) and with and without O VI absorption specifically (bottom). In the top panel no constraints are placed on the strength of the metal-line absorption or lack thereof. In the bottom panel a cutoff of  $N_{\text{O VI}} = 10^{13.2} \text{ cm}^{-2}$  is used for the presence or absence of O VI absorption (i.e., only O VI absorbers with larger column densities are considered, and O VI must be detectable at the cutoff column density to at least  $3\sigma$  significance for O VI non-detections).

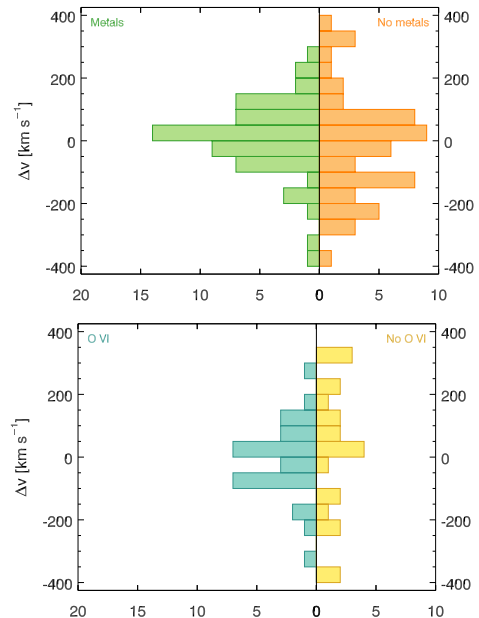
those that are metal free (i.e., H I-only systems) without regard to the strength of the metal-line absorption or lack thereof. The bottom panel of both Figures compares O VI absorbers specifically to those that do not show O VI (but perhaps show absorption from other metal species), both for a more direct comparison with the COS-Halos results and because O VI is the metal species that is the most sensitive tracer of low-metallicity gas located far from galaxies (Stocke et al. 2006, 2007). To be considered an O VI absorber for the purposes of these histograms an absorber must have  $N_{\text{O VI}} \geq 10^{13.2} \text{ cm}^{-2}$ . To be an O VI non-detection O VI must be detectable (i.e., high quality *FUSE* data must be available or the absorber must have sufficient redshift for O VI to be detectable in *HST/COS* data) to a  $3\sigma$  limit of  $N_{\text{O VI}} < 10^{13.2} \text{ cm}^{-2}$ .

Figure 10 shows that CGM absorbers with no detected metal lines have a lower average H I column than metal-line absorbers. This suggests that some of the “metal-free” absorbers may have similar metallicity to those with detected metals, but their H I column is so low as to make their associated metal lines undetectable in the current spectra; i.e., with greater S/N we would expect some of the “metal-free” absorbers in the right-hand side of Figure 10 to become metal-line absorbers. Based on the *CLOUDY* models described in Section 5, the metal-free absorbers could have metallicities  $\lesssim 0.1 Z_{\odot}$ . The bottom panel of Figure 10 attempts to correct for this effect by examining absorbers with and without O VI above a certain threshold. After this correction the average H I column density for CGM absorbers with and without

O VI are more comparable, although the metal-free absorbers are still systematically at lower  $N_{\text{H I}}$ .

If we assume for the moment that the metal-line detections are associated with high-metallicity outflows and the non-detections are associated with infalling, low-metallicity gas, then the similarity between the velocity distributions of H I absorbers with associated metal lines and those without (Figure 11) suggests that there is no clear kinematic discriminator between the two. This speculative conclusion also holds for the O VI and non-O VI absorbers. However, the relatively high threshold of metallicities ( $\log(Z/Z_{\odot}) \geq -1$ ) accessed by current COS spectroscopy leaves unanswered the metallicity of true IGM absorbers far from galaxies since the IGM metallicity level found at  $z > 2$  is in the range  $\log(Z/Z_{\odot}) \approx -2$  to  $-3$  (Schaye et al. 2003; Aguirre et al. 2004; Simcoe, Sargent, & Rauch 2004). Much higher S/N COS spectra than those presented here would need to be obtained to address this question.

Another issue that Figures 10 and 11 bring to light is systematic uncertainties in the estimate of the CGM mass (Section 6). The mass of individual CGM absorbers can only be estimated if there are sufficient metals present to constrain photo-ionization models (see Section 5 for details), so the “metal-free” absorbers are de facto assumed to have similar sizes and masses to the modeled absorbers. The large number of CGM absorbers with low-H I column density and no metals detected suggests that the ensemble CGM mass estimate of Section 6 is likely an overestimate of the true value. This increases the discrepancy between our CGM cool cloud mass



**Figure 11.** Distribution of absorber-galaxy radial velocity difference for absorbers with and without metals (top) and with and without O VI absorption specifically (bottom). In the top panel no constraints are placed on the strength of the metal-line absorption or lack thereof. In the bottom panel a cutoff of  $N_{\text{O VI}} = 10^{13.2} \text{ cm}^{-2}$  is used for the presence or absence of O VI absorption (i.e., only O VI absorbers with larger column densities are considered, and O VI must be detectable at the cutoff column density to at least  $3\sigma$  significance for O VI non-detections).

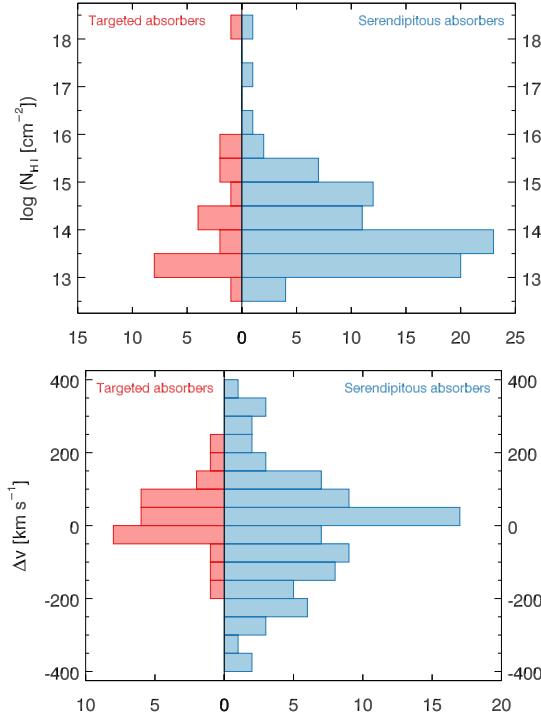


**Figure 12.** Distribution of H I column density (top) and absorber-galaxy radial velocity difference (bottom) for targeted and serendipitous absorbers. There are no significant differences in either quantity between the two samples.

estimate and that of [Werk et al. \(2014\)](#). A detailed discussion of this point can be found in Section 6.

### 7.1.2. Targeted and Serendipitous Absorbers

Given the differences between the targeted and serendipitous samples, such as the higher uncertainties in  $N_{\text{HI}}$  values for targeted absorbers (see discussions in Sections 3 and 5), it is fair to ask whether there are any systematic differences in the CGM properties of these galaxies. While Figure 1 shows that the targeted sample preferentially probes lower-luminosity galaxies at smaller impact parameters than the serendipitous sample, Figure 12 shows that there is little difference in the distributions of H I column density and absorber-galaxy radial velocity difference. The targeted sample shows some evidence for having a smaller characteristic velocity difference ( $|\Delta v| < 200 \text{ km s}^{-1}$ ) than the serendipitous sample, with only  $\sim 4\%$  (1/27) of its absorbers having  $|\Delta v| > 200 \text{ km s}^{-1}$  as compared to  $\sim 23\%$  (20/87) for the serendipitous one.

One interpretation of Figure 12 is that the outskirts of luminous galaxies look remarkably like the CGM of low-luminosity galaxies, except with a larger spread in velocity. This could simply be a consequence of higher mass halos having larger velocity dispersions, but it may suggest that the luminous serendipitous galaxies possess analogs to Galactic HVCs, which could be fossil relics of previous mergers with lower-luminosity companions. In the case of Milky Way HVCs, the connection with dwarf satellites is occasionally clear (e.g., the Magellanic Stream; [D’Onghia & Fox 2016](#)), but often even the largest HVCs cannot be associated with

a present-day Milky Way satellite (e.g., Complex C; [Wakker et al. 2007](#)).

Whenever appropriate in subsequent Figures we have endeavored to plot data points from the targeted and serendipitous samples with different plot symbols (circles for targeted galaxies/absorbers and triangles for serendipitous ones as in previous Figures). In all cases the data from the two different samples are well mixed, aside from the aforementioned differences in the host galaxy luminosities and impact parameters. This indicates that there are no further systematic differences in galaxy or inferred CGM properties between these two samples. Therefore, here and in Paper 1 the targeted and serendipitous samples are treated as a single sample.

### 7.1.3. Galaxy-Absorber Kinematics

Figures 13-15 examine correlations between properties of CGM absorbers and their host galaxies. In Sections 4.2 & 4.4 of Paper 1 we investigated basic observables relevant to absorber-galaxy kinematics. While the plots here present the data in a different format the overall conclusions here and in Paper 1 are the same.

The top panel of Figure 13 shows the galaxy-absorber radial velocity difference for metal-line and H I-only absorbers as a function of QSO-galaxy impact parameter. This plot of directly-observable quantities shows that there is little difference in the distribution of absorbers with and without associated metals, except that virtually all absorbers with  $\rho \lesssim 50 \text{ kpc}$  have associated metals and velocities close to the galaxy velocity. The bottom panel shows the same data plotted in normalized units, where the radial velocity difference is displayed as a multiple of the escape velocity from the galaxy halo at  $R = \rho$  and the impact parameter is plotted as a multiple of the galaxy virial radius. While some caution is advisable so as not to over-interpret this plot of derived quantities where both axes are dividing a projected quantity by a three-dimensional value, both in Paper 1 and here we interpret these low impact parameter and low  $|\Delta v|$  absorbers as recycling gas that is either outflowing or infalling but almost certainly remains bound to the associated galaxy.

At larger impact parameters ( $\rho \gtrsim 50 \text{ kpc}$ ) the  $|\Delta v|$  values increase significantly. However, this difference may be largely artificial because this is also the impact parameter where our overall sample becomes dominated by the serendipitous rather than the targeted galaxies. Since the serendipitous absorbers are associated with more luminous galaxies (see Figure 1), the velocity differences are systematically larger but the  $|\Delta v|/v_{\text{esc}}$  distributions are not so different; i.e., compare the spread in  $\Delta v$  at  $\rho \approx 100 \text{ kpc}$  in the top panel of Figure 13 with the spread in  $|\Delta v|/v_{\text{esc}}$  at  $\rho/R_{\text{vir}} \approx 1$  in the bottom panel.

However, there are a few (5) significant outliers in the bottom panel of Figure 13 with  $|\Delta v|/v_{\text{esc}} > 5$ , which are certainly not gravitationally bound to their associated galaxy. Whether this means that these five are true IGM absorbers, not associated with a single galaxy despite their modest impact parameter ( $\rho/R_{\text{vir}} \approx 1.5$ ), or whether these are unbound infalling or ejected clouds, is not clear. The three absorbers apparently associated with low mass galaxies ( $\log M_* < 8$ ; see Figure 14) could be associated with large-scale structures

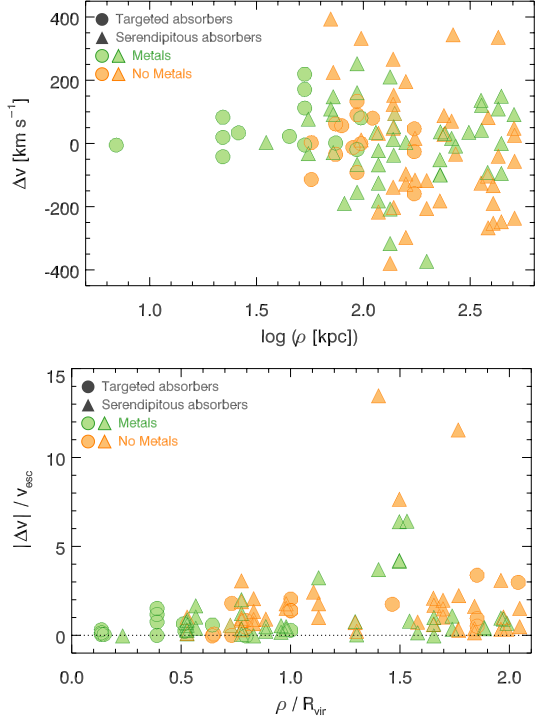


**Figure 13.** Distribution of CGM absorber-galaxy radial velocity difference as a function of impact parameter in directly observable (top) and derived (bottom) units. The absorbers with the largest velocity difference ( $|\Delta v| > 5 v_{\text{esc}}$ ) are all located far from the nearest galaxy ( $\rho \gtrsim 1.4 R_{\text{vir}}$ ).

in their vicinities instead (Rosenberg et al. 2003; Yoon et al. 2012; Keeney et al. 2014; Stocke et al. 2014). The same may be the case for the multiple-velocity-component absorbers with  $|\Delta v|/v_{\text{esc}} > 5$  apparently associated with galaxies at  $\log M_* \approx 9.4$ . The uncertain associations mentioned here (3C 273/1585, Mrk 335/2281, PG 1116+215/17614 & 17676, and Q 1230+0115/1497) are detailed in Section A.2 of the Appendix (see also Section 7.2).

Figure 14 is similar to Figure 13 except that it plots the luminosity of the host galaxy instead of an absorber’s distance from it. The top panel of Figure 14 plots directly-observable quantities: galaxy-absorber radial velocity difference as a function of rest-frame  $g$ -band galaxy luminosity in  $L^*$  units. Again we find no clear distinction between CGM absorbers with and without associated metals. The bottom panel plots the radial velocity difference as a multiple of escape velocity from the galaxy at  $R = \rho$  as a function of the host galaxy’s stellar mass; see Section 4 for a description of the  $M_*$  derivation. The dispersion of  $|\Delta v|/v_{\text{esc}}$  is clearly higher for galaxies with  $M_* < 10^{10} M_{\odot}$  and probably indicates that some of these are unbound absorbers.

The general trends found in the bottom panels of Figures 13 and 14 are unsurprising since lower mass galaxies have smaller escape velocities and the escape velocity for a given galaxy decreases as the distance from the galaxy increases. Thus, an observed value of  $|\Delta v| < 400 \text{ km s}^{-1}$  will be a larger multiple of the escape velocity far away from less massive galaxies, exactly as found in Figures 13 and 14. The handful of absorbers with extremely large peculiar velocities

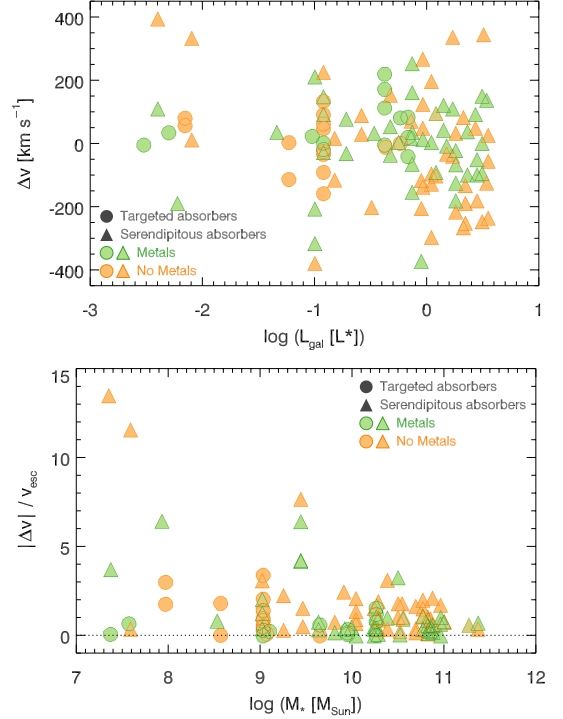


**Figure 14.** Distribution of CGM absorber-galaxy radial velocity difference as a function of galaxy size in directly observable (top) and derived (bottom) units. The absorbers with the largest velocity difference ( $|\Delta v| > 5 v_{\text{esc}}$ ) are all associated with less massive galaxies ( $M_* < 10^{10} M_{\odot}$ ).

( $|\Delta v|/v_{\text{esc}} > 5$ ) are a mixture of metal-line and H I-only absorbers, and all but one have  $N_{\text{HI}} < 10^{14} \text{ cm}^{-2}$ . However, the three absorbers with the largest  $|\Delta v|/v_{\text{esc}}$  values are metal-free to a limiting metallicity of  $\lesssim 10\%$  solar. The absorber with the largest  $|\Delta v|/v_{\text{esc}}$  value (Q 1230+0115/1497) is in an area very well surveyed for galaxies to a limit of  $< 0.01 L^*$ . In Rosenberg et al. (2003) we speculated that this absorber and the 3C 273/1585 absorber (at  $|\Delta v|/v_{\text{esc}} \sim 6.5$  in this plot) both are part of a large-scale filament of galaxies and gas in this region and not associated with any one galaxy (see also Keeney et al. 2014).

Taken together, these Figures show that there is no easy kinematic or size/mass dichotomy between absorbers with associated metal lines and those without. Going one step further, this means that we have found no simple kinematic diagnostic to distinguish low-metallicity gas accreting onto a galaxy from higher-metallicity gas entrained in a galactic wind even though simulations strongly imply that both infalling and outflowing gas are pervasive in the CGM at  $z \sim 0$  (e.g., Kereš & Hernquist 2009).

This conclusion is bolstered by Figure 15, which shows the distribution of CGM sight lines with respect to the host galaxy’s major axis for the subset of QSO-galaxy pairs where the galaxy’s major axis is well-defined. Half of the CGM sight lines (15/30) are located within the galaxy’s virial radius, and we see a modest dependence on impact parameter of the fraction of sight lines containing metals, with 80% (12/15) of the sight lines located within a galaxy’s virial radius containing metals as opposed to 60% (9/15) of the sight

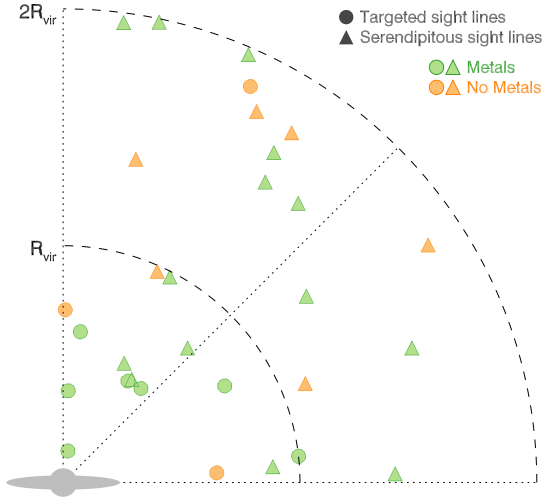


**Figure 15.** Distribution of QSO sight lines with respect to the major axis of the nearest galaxy, where such information is available. Half of the sight lines (15/30) are located within the galaxy’s virial radius and 70% (21/30) are located within  $45^\circ$  of the galaxy’s minor axis. There is no appreciable difference in the fraction of sight lines containing metals as a function of azimuthal angle, but there is some dependence on impact parameter with 80% (12/15) of sight lines within the galaxy’s virial radius containing metals as compared to 60% (9/15) at larger distances.

lines at larger distances. However, the fraction of sight lines containing metals as a function of azimuthal angle is relatively constant. This is somewhat surprising as galactic outflows are found to be bipolar with small opening angles centered on the minor axis (Veilleux et al. 2005) and IGM accretion is expected to occur closer to the galaxy’s major axis (Kereš & Hernquist 2009).

Bouché et al. (2012) found a bimodal distribution of CGM absorbers when studying strong Mg II absorbers at  $z \sim 0.1$ . In that study, half of the sight lines containing strong Mg II absorbers were located near the galaxy’s major axis and the other half within  $30^\circ$  of its minor axis. While 70% (21/30) of our CGM sight lines are located closer to the galaxy’s minor axis than its major axis<sup>6</sup>, Figure 15 shows that the azimuthal angle distribution of the sight lines is otherwise rather uniform. However, this could be because we are examining all sight lines that show CGM absorption, regardless of the H I column density, whereas Bouché et al. (2012) were studying the distribution of strong Mg II absorbers, which are known to preferentially select Lyman limit systems ( $N_{\text{HI}} > 10^{17.3} \text{ cm}^{-2}$ ; Steidel 1995). Our CGM sample has too few Lyman limit systems (4) to make a direct comparison with the Bouché et al. (2012) results, but if we limit our sample to only include absorbers with  $N_{\text{HI}} > 10^{15} \text{ cm}^{-2}$  we still do not find a bimodal absorber distribution.

<sup>6</sup> Some of the targeted sight lines were specifically chosen to be near the targeted galaxy’s minor axis, potentially biasing this result. However, we find the same fraction of sight lines closer to the galaxy’s minor axis in the targeted (7/10) and serendipitous (14/20) samples, suggesting that there is no systematic bias between the samples.

## 7.2. Are Absorbers Associated Unambiguously with a Single Galaxy?

We have assumed throughout this Paper that a galaxy-absorber association exists if a galaxy is located within a projected distance of  $2 R_{\text{vir}}$  of the QSO sight line and has a velocity within  $400 \text{ km s}^{-1}$  of an H I Ly $\alpha$  absorber. Here we examine the robustness of this assumption by searching for not only the nearest galaxy (ng) to the QSO sight line (i.e., those tabulated in Tables 1 and 2) but the next-nearest galaxy (nng) as well. The last three columns of Tables 1 and 2 list the ratios of the impact parameters for the nearest and next-nearest galaxies ( $\eta_\rho = \rho_{\text{ng}}/\rho_{\text{nng}}$ ), the ratios of their normalized impact parameters ( $\eta_{\text{vir}} = (\rho/R_{\text{vir}})_{\text{ng}}/(\rho/R_{\text{vir}})_{\text{nng}}$ ), and the ratios of their normalized absorber-galaxy velocity differences ( $\eta_{\Delta v} = (|\Delta v|/v_{\text{esc}})_{\text{ng}}/(|\Delta v|/v_{\text{esc}})_{\text{nng}}$ ), respectively. In all cases a value near zero means that the nearest galaxy is significantly closer than the next-nearest galaxy, suggesting a secure association. In some cases only one galaxy is located with  $\rho < 1 \text{ Mpc}$  and  $|\Delta v| < 400 \text{ km s}^{-1}$  of an absorber (i.e., the maximum extent of our search volume;  $1 \text{ Mpc} = 2 R_{\text{vir}}$  for a galaxy with  $L \approx 20 L^*$  according to the prescription of Paper 1), in which case we quote an upper limit for  $\eta_\rho$  but no value for  $\eta_{\text{vir}}$  or  $\eta_{\Delta v}$ . Figure 16 shows that almost all associations in this sample are rather unambiguous since there is no arguably closer galaxy ( $\eta_{\text{vir}} > 1$ ) in either normalized impact parameter ( $\rho/R_{\text{vir}}$ ) or normalized velocity difference ( $|\Delta v|/v_{\text{esc}}$ ). However, there are a few exceptions in both samples.

While the serendipitous sample galaxies were chosen to have  $\eta_{\text{vir}} < 1$  by construction (see Section 2 for details), the targeted sample galaxies were chosen first with no specific isolation criterion, which could lead to some ambiguities. In most cases the targeted galaxy is the closest to the absorber, but Figure 16 shows four cases with  $\eta_{\text{vir}} > 1$ , two at  $\rho/R_{\text{vir}} \geq 1.5$  and two at much smaller normalized impact parameters and velocity differences.

The two targeted absorbers with ambiguous associations ( $\eta_{\text{vir}} > 1$ ) at large  $\rho/R_{\text{vir}}$  are related to each other, as the QSO/galaxy pairs were chosen specifically to observe two distinct sight lines to probe two galaxies at comparable redshifts. It is not surprising that these absorbers have ambiguous associations. The 1ES 1028+511 sight line has two H I Ly $\alpha$  absorbers within  $400 \text{ km s}^{-1}$  of each other and a targeted galaxy that corresponds to each absorber. If this were a serendipitous sight line, then the two Ly $\alpha$  absorbers would be treated as probing the CGM of a single galaxy, so for the purposes of the  $\eta$  values in Table 1 we treat SDSS J103108.88+504708.7 as the nearest galaxy and UGC 5740 as the next-nearest galaxy. Similarly, the galaxy SDSS J103108.88+504708.7 is actually closer to the 1SAX J1032.3+5051 sight line than is UGC 5740 so it is treated as the nearest galaxy there as well. The bottom panel of Figure 16 shows that these two absorbers have peculiar velocities greater than the escape velocities for these two galaxies, making their direct association with either galaxy ambiguous.

The third and fourth ambiguous associations in Figure 16 are targeted galaxies in small groups in which a fainter mem-



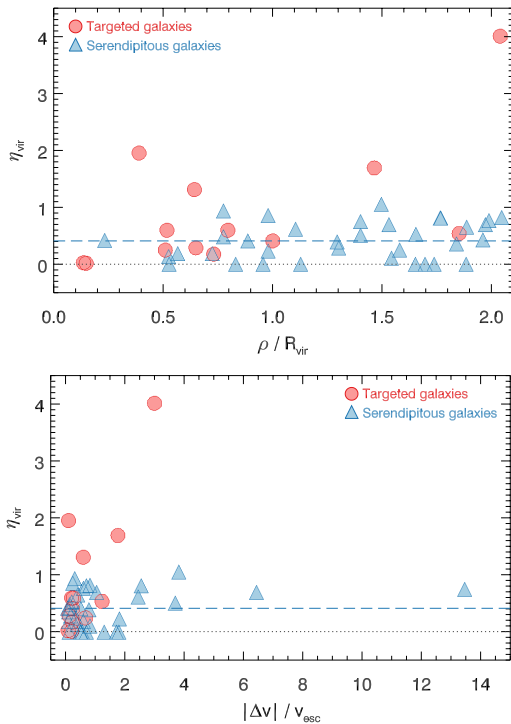


**Figure 16.** Ratio of the normalized impact parameter for the nearest galaxy compared to the normalized impact parameter for the next-nearest galaxy as a function of normalized impact parameter (top) and normalized velocity absorber-galaxy difference (bottom). The dashed horizontal line indicates the median value of  $\eta_{\text{vir}}$  in the serendipitous sample, which is more homogeneous than the targeted sample. The serendipitous sample shows no clear trend in the top panel and only a slight ( $1.4\sigma$ ) positive correlation in the bottom panel. Small values of  $\eta_{\text{vir}}$  indicate that the next-nearest galaxy is much further from the absorber than the nearest galaxy.

ber is closer to the sight line. In one case, the luminous starburst galaxy NGC 2611 was the galaxy targeted for observation using the PG 0832+251 sight line but subsequent, deeper spectroscopy found that it is a member of a small group of galaxies, one of which is significantly closer to the sight line than NGC 2611. The case of the PMN J1103–2329 sight line is similar in that it was chosen to probe the starburst galaxy NGC 3511 but the lower-luminosity galaxy NGC 3513 is in fact closer to the sight line and has a velocity coincident with the  $1194 \text{ km s}^{-1} \text{ Ly}\alpha$  absorber. NGC 3511 has a velocity coincident with the other velocity component in this absorber at  $1113 \text{ km s}^{-1}$ . No other targeted associations appear ambiguous.

While the “typical” serendipitous galaxy is  $\sim 2.4$  times closer than the next-nearest galaxy ( $\eta_{\text{vir}} = 0.41$ ; dashed horizontal lines in Figure 16) there is large scatter and no trend for galaxies closer to the QSO sight line to have smaller  $\eta_{\text{vir}}$  values (i.e., more secure associations). There is also no significant trend ( $1.6\sigma$  positive correlation as measured by Kendall’s tau test) for associations with larger velocity differences (see bottom panel of Figure 16, where we use a single absorption velocity equal to the  $N_{\text{HI}}$ -weighted mean of all of the associated absorption components when the  $\text{Ly}\alpha$  absorber is complex). However, in both plots of Figure 16, the  $y$ -axis is a measure of the robustness of the association only

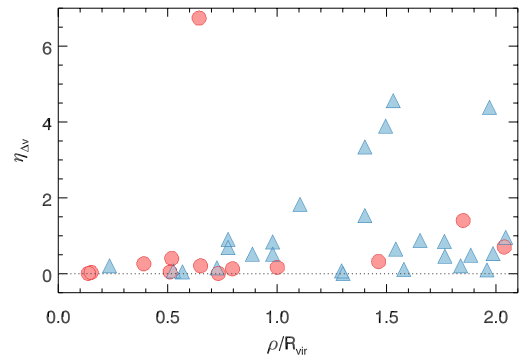


**Figure 17.** The ratio of the normalized absorber-galaxy velocity difference ( $|\Delta v|/v_{\text{esc}}$ ) for the nearest galaxy compared to the normalized velocity difference for the next-nearest galaxy as a function of normalized impact parameter ( $\rho/R_{\text{vir}}$ ). Small values of  $\eta_{\Delta v}$  indicate that the next-nearest galaxy is much further from the absorber in velocity space than the nearest galaxy. Beyond  $\sim 1.4$  virial radii,  $\sim 25\%$  of the associations are questionable due to the next-nearest galaxy having a much closer velocity match with the absorber than the nearest galaxy.

on the sky plane, which the original association criteria (i.e., choosing the closest galaxy by normalized impact parameter) constrains to be  $\lesssim 1$ . Thus, this plot does not measure fully the robustness of the serendipitous associations.

Figure 17 shows the ratio of the normalized velocity differences for the nearest and next-nearest galaxies,  $\eta_{\Delta v}$ , plotted against normalized impact parameter,  $\rho/R_{\text{vir}}$ , for the nearest galaxy. As before the smaller the  $y$ -axis value, the more secure the association with the individual galaxy we have identified. Here there is a clear trend in which there are significantly larger  $\eta_{\Delta v}$  values at  $\gtrsim 1.4$  virial radii. This means that while the next-nearest neighbor is farther from the absorber on the sky, it is significantly closer in radial velocity difference, making these associations more ambiguous.

**Table 10.** Next-Nearest Galaxy Properties for Passive Galaxy Associations

Nearest Galaxy	$cz_{\text{ng}}$ ( $\text{km s}^{-1}$ )	$L_{\text{ng}}$ ( $L^*$ )	NG Type	$(\rho/R_{\text{vir}})_{\text{ng}}$	NNG Type	$L_{\text{nng}}$ ( $L^*$ )	$\eta_{\rho}$	$\eta_{\Delta v}$	Comments
(1)	(2)	(3)	(4)	(5)	(6)	(7)	(8)	(9)	(10)
SDSS J122950.57+020153.7	1775	0.006	dSph	1.53	SBb	0.43	0.31	4.55	Dwarf post-starburst; rich group member
SDSSJ 111906.68+211828.7	41428	1.2	Sa	0.72	S0	0.92	0.22	0.16	BLA and broad-O VI present; rich group member
SDSS J130101.05+590007.1	13862	0.47	S0	0.98	dSph	0.063	1.55	0.53	Broad-O VI present
SDSS J215517.30-091752.0	21951	2.7	E	1.98	SBa	0.67	1.47	0.77	Small group member; metal-free absorbers
2MASX J13052094-1034521	28304	3.4	E:	1.29	S:	0.33	0.91	0.08	Broad-O VI present

One complication for this plot is that the  $N_{\text{HI}}$ -weighted mean absorber velocity is used. For some complexes of absorbers, the velocity spread of the observed components is large enough that an individual component velocity may coincide with the associated absorber velocity even if the mean velocity does not (see discussion of individual cases in Section A.2 of the Appendix). The one targeted absorber/galaxy pair with large  $\eta_{\Delta v} = 6.7$  is the PMN J1103-2329/NGC 3511 association discussed above, which has one velocity component coincident with the galaxy recession velocity and another at  $\Delta v = 80 \text{ km s}^{-1}$ .

The physical circumstances that create these large values of  $\eta_{\Delta v}$  are the combination of a small galaxy close to the sight line, which we identify as the associated galaxy, and a larger, more luminous and massive galaxy farther away. Since the more massive galaxy has a larger estimated escape velocity, its  $|\Delta v|/v_{\text{esc}}$  is smaller. These large  $\eta_{\Delta v}$  values in Figure 17 are unlikely to be due to incomplete galaxy survey work along these sight lines. Two of the serendipitous absorbers with the largest  $\eta_{\Delta v}$  values are 3C273/1585 and Q 1230+0115/1489, which are both in regions surveyed completely to well below  $0.01 L^*$ .

This type of ambiguity occurs  $\sim 25\%$  of the time for absorbers with associated galaxies at  $\rho/R_{\text{vir}} \geq 1.4$ , but with some lesser ambiguity at  $1 < \rho/R_{\text{vir}} < 1.4$ . Although the sample size is small, we conclude that claimed associations are robust for absorbers found within the virial radius of individual galaxies but become increasingly uncertain beyond one virial radius. While the virial radius does not seem to provide any firm physical boundary for the CGM (Shull 2014, and see Section 3.1 in Paper 1), operationally it appears to be a good, rough estimate for the maximum extent to which individual galaxies can be associated with CGM absorbers.

### 7.2.1. Do Passive Galaxies Possess Cool CGM Clouds?

One of the more intriguing results from the COS-Halos (Tumlinson et al. 2011) study of the cool gas CGM of low-redshift galaxies is that luminous (see Figure 2), passive galaxies with very low sSFR have H I Ly $\alpha$  absorption in their halos (Thom et al. 2012). Unlike star-forming galaxies in the COS-Halos study, most of these galaxy halos are

not detected in O VI, the targeted metal ion (Tumlinson et al. 2011). However, some are detected in low-ionization absorption (e.g., Mg II, Si II, C II; Werk et al. 2013), and Mg II absorption has been detected in luminous early-type galaxies at intermediate redshifts in some cases (Zahedy et al. 2016). Both the presence and origins of this cool gas are uncertain and problematical since in-falling cool CGM gas clouds are thought to fuel new star formation in the galaxy disk and winds produced by recent star formation are thought to create outflowing and recycling CGM clouds in galaxy halos. Neither seems to be the case for passive galaxies.

In the current serendipitous sample there are only five apparently associated galaxies which have very low-sSFR (sSFR  $< 10^{-11} \text{ yr}^{-1}$ ; see Figure 2) based on the non-detection of H $\alpha$  in our galaxy survey data (Keeney et al. 2017). If the cool gaseous halos of early- and late-type galaxies are similar we would expect that a comparable number of bright early-type and late-type galaxy halos would be detected since they are comparably numerous in the low- $z$  universe based on the SDSS luminosity functions of red and blue galaxies shown in Montero-Dorta & Prada (2009). But, instead, only  $\sim 15\%$  (5/35) of the associated galaxies in our sample are Ly $\alpha$  detections in very low-sSFR galaxies. No very low-sSFR galaxies were targeted by the COS GTO observations.

The primary concern mentioned in Paper 1 about the potential association of low-sSFR galaxies with absorbers is that early-type systems are typically found in rich groups or clusters. This makes it likely that other possible associated galaxies with high sSFR can be nearby. However, this does not diminish concerns as to why this gas does not fall into the passive galaxy stimulating star formation. The five absorbers in Table 3 that are associated with very low-sSFR galaxies are listed in Table 10 keyed by the associated galaxy name. Both the basic properties of the associated galaxy and the next nearest galaxy (NNG) are listed with column headings as defined in Table 7. The first entry (SDSS J122950.57+020153.7) is a dwarf post-starburst galaxy near the 3C 273 sight line, which has been extensively modeled and discussed by Stocke et al. (2004) and Keeney et al. (2014). Since this galaxy is quite different from the others in Table 10, it will not be discussed further here.

Three of the remaining associations are at  $\rho < 1.4 R_{\text{vir}}$  for which our analysis above suggests that associations should be secure. Two of these 4 are identified as being members of small galaxy groups and there is a broad O VI + BLA absorber that has been identified as group gas near SDSS J111906.68+211828.7 (Stocke et al. 2014). Two other absorbers with passive galaxy associations possess broad O VI absorption. In two of the four cases the NNG is also an early-type galaxy so that for these two the only association ambiguity is between an individual passive galaxy (either the nearest galaxy or the NNG) or with an entire group of galaxies. The last two absorbers in Table 10 have the largest impact parameters and have NNGs which are late-type star forming galaxies which could be the associated galaxy; e.g., these two have  $\eta_{\rho} \geq 1$  but are not so well-matched in velocity with the absorber. For these two the concerns of Paper 1 seem valid that an alternative late-type galaxy association is plausible.

But based on the two firmest associations in Table 10 (SDSS J111906.68+211828.7 and SDSS J130101.05+590007.1) we confirm the result of Thom et al. (2012) that Ly $\alpha$  absorption is associated with some early-type, low- $z$  galaxies. Unlike Thom et al. (2012) we find metal absorption, including O VI, associated with at least one H I velocity component in all but one case in Table 10. The two-component Ly $\alpha$ -only absorber PHL 1811/21998, 22042 is almost 2 virial radii from the nearest luminous galaxy, SDSS J215517.30–091752.0, and could be primordial infall onto this galaxy and/or others in the region.

While the very low, *current* sSFR of these galaxies makes them typical of early-type galaxies in the local universe, only one of these four luminous passive galaxies has sensitive GALEX upper limits, confirming that this galaxy (SDSS J215517.30–091752.0) is fully passive. For 2MASX J13052094–1034521, weak GALEX UV detections require a longer-term sSFR of  $\log \text{sSFR} = -11.3$ ; the other two galaxies have no GALEX observations. If these two and the 16 COS-Halos passive galaxies of Thom et al. (2012) all lack significant UV flux, then these Ly $\alpha$ -detected passive galaxies are rather typical red galaxies in which star formation has largely, if not completely, ceased. And yet they possess cool gas clouds in their halos. Near-UV imaging with HST/WFC3 can measure their longer-term star formation rate and resolve this outstanding question. Similar observations of the Thom et al. (2012) galaxies can determine if CGM-selected passive galaxies had star forming events too long ago to show H $\alpha$  emission. Ly $\alpha$  absorption-selected passive galaxies can provide new insights into the evolutionary progress of galaxies across the “green valley”. Their further study is warranted for understanding how star formation is quenched in galaxies.

Three of the five absorbers in this sample are complexes of two or three Ly $\alpha$  velocity components; at least one of these components is metal-rich in each case. These three have strong, broad O VI which is likely to be “warm” ( $T > 10^5$  K) gas associated with the entire galaxy group (Stocke et al. 2014). One of these (PG 1116+215/41428) was described in

Stocke et al. (2014) as a “warm” absorber in a small galaxy group. The warm gas in these groups is postulated to be interface gas between the cool, photo-ionized gas clouds in the CGM and a hotter intra-group medium in the process of developing in these galaxy groups (Stocke et al. 2014). Similar “warm” absorption could be present in the Thom et al. (2012) absorbers associated with passive galaxies but the COS-Halos spectra have insufficient signal-to-noise to detect the broad, shallow O VI and Ly $\alpha$  that we predict is present.

The hypothesis which arises out of this analysis is that the hot intra-group gas may be inhibiting the accretion of these cool gas clouds onto the associated galaxy so that no ongoing star formation is induced by CGM gas in these cases. The source of this cool CGM gas could be either a past star formation event in the passive galaxy or a wind from a lower luminosity, even dwarf galaxy like in the case of the 3C 273 dwarf post-starburst galaxy. After being ejected from a group galaxy, the cool gas clouds in small galaxy groups may not accrete easily onto passive galaxies in their vicinity. They remain “warm” ( $5 < \log T < 6.5$ )<sup>7</sup> due to being shock-ionized by collisions with other CGM clouds or through contact with the hotter intra-group medium which is in the process of developing in these groups. New HST/COS observations of nearby galaxy groups can be used to test this hypothesis (HST Cycle 23 project #14277; J. Stocke, PI).

### 7.3. CGM Properties and SFR Correlations

Because there is a strong dichotomy in CGM properties between star-forming and “passive” galaxies in the COS-Halos study (Tumlinson et al. 2011; Thom et al. 2012), it might be expected that correlations between basic CGM properties and SFR/sSFR would be present in our sample. Since one source of CGM gas is ejected and/or recycling gas produced by current or longer-term star formation in the disk, CGM/galaxy disk correlations would be expected. On the other hand, QSO probes through the CGM of individual galaxies are anecdotal in that they sample only a specific pencil beam through each galaxy’s gaseous halo; i.e., while the CGM of disk galaxies with high and low SFRs might possess quite different bulk CGM properties, individual sight lines may not reflect accurately such differences. Further, there may be timing differences between the observed SFR and the gaseous content of the CGM so that current CGM properties may be correlated with past, rather than current, star-forming activity.

At high- $z$ , the C II\*  $\lambda 1335.7$  Å transition can derive the sSFR of DLA host galaxies (Wolfe, Prochaska, & Gawiser 2003a; Wolfe, Gawiser, & Prochaska 2003b), but these values were not used individually but rather as averages in redshift bins over many systems to verify the SFR vs. redshift relationship (a.k.a. the “Madau plot”; Madau et al. 1996; Steidel et al. 1999). Therefore, while correlations between CGM absorption properties and associated galaxy SFR would be interesting, if no correlation is present we cannot conclude that the CGMs of high- vs low-SFR galaxies are similar.

Figure 18 shows the relationship between SFR determined

<sup>7</sup> All temperatures reported in logarithms have units of Kelvin.

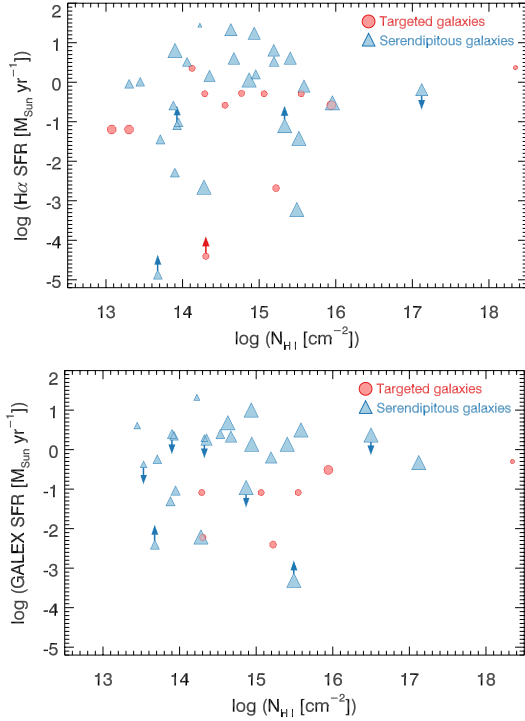


**Figure 18.** Galaxy SFR as measured by  $H\alpha$  (top) and *GALEX* FUV continuum (bottom) luminosity as a function of total CGM H I column density. No statistically significant correlation is evident.

by  $H\alpha$  line emission (top) and by *GALEX* FUV continuum emission (bottom) with  $\log N_{\text{HI}}$ . No correlations are found except perhaps a very shallow decrease in  $\log N_{\text{HI}}$  with increasing  $H\alpha$  SFR. A similar absence of correlations are found by using sSFR (Figure 19). Because our sample shows no trend of H I column density with impact parameter, we make no re-normalization of the column density data to a specific impact parameter. However, we have used the cumulative  $N_{\text{HI}}$  values for complex absorbers described in the previous paragraph, thus summing all of the CGM clouds along each sight line.

While the H I column density is one of a handful of direct observables, we also searched for correlations between SFR and the two model parameters emerging from the CLOUDY modeling: ionization parameter and absorber metallicity. While this greatly reduces our sample size (23 absorbers have good quality CLOUDY model fits but not all of these have good SFR estimates), a case can be made that these derived CGM quantities may be more closely tied to current or recent SFR. We are left with  $\sim 12$  sample points only and no correlations between nearest galaxy SFR and either ionization parameter or metallicity is present. We conclude that individual sight line CGM properties cannot be used as indicative of the entire CGM condition in any one galaxy probed.

## 8. CONCLUSIONS

In this paper we have presented the basic data used to determine specific CGM cool cloud properties and ensemble cool ( $T \sim 10^4$  K) CGM gas mass estimates associated with low- $z$  galaxies as first presented in Paper 1. We refer the reader to [Savage et al. \(2014\)](#) and [Stocke et al. \(2014\)](#) for a detailed

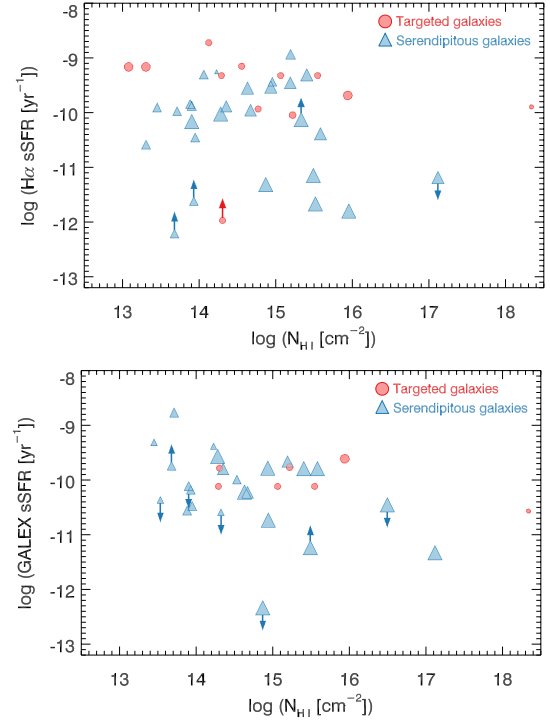


**Figure 19.** Galaxy sSFR as measured by  $H\alpha$  (top) and *GALEX* FUV continuum (bottom) luminosity as a function of total CGM H I column density. No statistically significant correlation is evident.

discussion of the O VI absorption and the “warm” gas phase since in this paper and Paper 1 we concentrate on the cool, photo-ionized gas.

These data include the H I and metal-line absorption (Section 3) seen in FUV spectra of bright AGN taken with *HST/COS*, *HST/STIS* and *FUSE*. Detailed line fits and tabulated column densities are presented in Figure 4 and Table 3. The sample analyzed herein includes a “targeted” set of sight-line/galaxy pairs observed by the COS GTO team using *HST/COS* with the G130M and G160M gratings. A second sample of “serendipitous” sight-line/galaxy pairs uses *HST/COS*, *HST/STIS* and *FUSE* FUV spectra of very bright AGN whose detected H I absorptions at  $z \lesssim 0.2$  lie within  $\sim 2$  virial radii of a foreground galaxy in our extensive database of  $\sim 700$  galaxies located  $< 1$  Mpc from these sight lines. These samples nicely complement the two samples of galaxies constituting the COS-Halos and COS-Dwarfs surveys ([Tumlinson et al. 2011](#); [Bordoloi et al. 2014](#)). Basic data for the associated galaxies also are presented in Section 4, including redshifts, luminosities, metallicities and star-formation rates determined both by  $H\alpha$  imaging (see Appendix B) and by *GALEX* UV imaging, as well as inferred properties such as virial radius, stellar mass and halo mass (see Tables 6 & 7 in Section 4). Single-phase, homogeneous CLOUDY photo-ionization models are presented in Section 5; when multi-phase gas is present we attempt to model only the coolest phase detected (i.e., the lowest ions).

The following major results are obtained:

1. We find that associations between absorbers and an individual, nearest galaxy are robust, and almost always unambiguous, *if the sight line lies within the virial radius of the galaxy*. These associations become less secure at larger impact parameters and are sometimes ambiguous at  $\rho > 1.4 R_{\text{vir}}$ , where the absorbers are often more appropriately linked to several nearby galaxies or to an entire small galaxy group (see Section 7.2).
2. We find no evidence for increasing ionization parameter or declining H I column density, line-of-sight cloud thickness, cloud mass, or cloud pressure with increasing impact parameter. These results differ from the trends found by Werk et al. (2014) from the COS-Halos sample, but are not inconsistent because these two studies probe different ranges of impact parameter:  $\rho < 0.5 R_{\text{vir}}$  for COS-Halos and  $0.5 R_{\text{vir}} < \rho < 2 R_{\text{vir}}$  for this study. The associated galaxies also differ since the COS-Halos galaxies were selected to be both luminous and isolated while the current sample has no such restrictions.
3. We find no correlations between current or longer term (i.e.,  $\leq 1$  Gyr) SFR and CGM absorber parameters like  $N_{\text{HI}}$ . This is expected since it seems quite unlikely that a single, pencil-beam probe of the CGM can adequately constrain its bulk properties.
4. We have found at least two, and possibly four, serendipitously discovered absorbers with H I and metal-lines associated with passive galaxies (Section 7.2.1), in support of the COS-Halos discoveries of such unexpected associations (Thom et al. 2012). Since the presence of cool gas in passive galaxy halos is unexpected, these absorption-line detected, passive galaxies deserve further study.
5. Using the metal-rich absorbers detected in these *HST*/COS and *HST*/STIS spectra as a fair sampling of the CGM of low- $z$  galaxies, we confirm the ensemble CGM cool cloud mass obtained by Paper 1 of  $\log(M/M_{\odot}) = 10.2 \pm 0.3$ . Since we have employed a different line-fitting method than used in Paper 1, this result suggests that these mass estimates are robust to the details of the data analysis.
6. We summarize the statistical understanding of the cool, photo-ionized CGM obtained from this study of a diverse set of low- $z$  galaxies as follows. The cool cloud population of a typical  $L \geq L^*$ , star-forming galaxy consists of a few thousand individual clouds at sizes of  $> 1$  kpc (there are likely  $> 10,000$  smaller clouds with sizes  $200 \text{ pc} \leq D_{\text{cl}} < 1 \text{ kpc}$ ) that fill  $\sim 5\text{-}9\%$  of the CGM volume inside the virial radius of these galaxies. The 300-500 largest ( $\geq 20$  kpc), most massive ( $\geq 10^7 M_{\odot}$ ) clouds dominate the ensemble CGM mass but are detected only  $\gtrsim 20\%$  of the time along random sight lines through the volume inside the virial

radius. Thus, the number of these most massive clouds in any absorption-line probe of the CGM is small, which leads to sparse sampling statistics and large uncertainties in ensemble mass ( $\pm 0.3$  dex estimated herein for the super- $L^*$  sample). Lower mass star-forming galaxies have similar CGM properties (scaled down by galaxy mass), although dwarfs have lower cloud covering factors, as detailed in Paper 1.

7. While the statistical error budget on the determination of the CGM cool gas mass is large (factor of  $\sim 2$ ), both for this study and COS-Halos, the Werk et al. (2014) “preferred lower limit” and the latest COS-Halos value of nearly  $10^{11} M_{\odot}$  (Prochaska et al. 2017) suggest a very different picture of the CGM than the current result. Much of the difference in these values can be attributed to the considerably different low- $z$  ionization rate assumed; this study assumed Haardt & Madau (2012) while COS-Halos assumes the higher values of Haardt & Madau (2001). While it is beyond the scope of this paper to determine which of these two ionization rates (if either) are correct for CGM absorbers, we have instead corrected the latest COS-Halos CGM cool gas mass estimate to the Haardt & Madau (2012) ionization rate and then used both results in the radial regime for which each best-samples the CGM (COS-Halos at  $\rho \leq 0.5 R_{\text{vir}}$  and the present study outside that radius). By this method, we obtain a “best-value” for the CGM cool gas mass of  $\log(M/M_{\odot}) = 10.5 \pm 0.3$ , amounting to  $\sim 30\%$  of the total baryon inventory of  $L \geq L^*$  spiral galaxies.

We further suggest that many of the O VI absorbers, cataloged but not studied herein, are likely detections of “warm” or “warm-hot” interface gas at  $T \approx 10^5\text{-}10^{6.5}$  K (Savage et al. 2014; Stocke et al. 2014). While this O VI-absorbing gas probably does not contain sufficient baryons to account for all those “missing”, the abundance of these absorbers at  $z \sim 0$  ( $dN/dz \approx 4$ ; Stocke et al. 2014) attests to the likely presence of large amounts of even hotter ( $T \approx 10^6\text{-}10^7$  K) gas that may permeate small, low-redshift, spiral-rich galaxy groups. Despite O VI being a minority tracer of gas at those temperatures, the lack of high-resolving-power spectrographs at soft X-ray wavelengths means that *HST*/COS remains the most sensitive way to detect such gas currently through broad, shallow O VI and Ly $\alpha$  absorbers.

We wish to thank the anonymous referee for comments that stimulated us to improve the quality of the final manuscript. This work was supported by NASA grants NNX08AC146 and NAS5-98043 to the University of Colorado at Boulder for the *HST*/COS project. BAK and JTS gratefully acknowledge additional support from NSF grant AST1109117. This research has made use of the NASA/IPAC Extragalactic Database (NED) which is operated by the Jet Propulsion Laboratory, California Institute of Technology, under contract with the National Aeronautics and Space Administration. This research has also made use of the “K-corrections calculator” service available at <http://kcor.sai.msu.ru/>.

We thank J. Rosenberg and E. Ryan-Weber, who assisted in selecting the targeted QSO/galaxy pairs in this study, and J. Moloney for assistance with the cosmological simulations of Shull et al. (2015).

*Facilities:* HST (COS, STIS), ARC (SPICAM, DIS), Sloan, GALEX, KPNO:2.1m, CTIO:0.9m

## APPENDIX

### A. NOTES ON INDIVIDUAL CASES

#### A.1. Absorption-Line Fits

In the descriptions below each absorber discussed is identified by the sight line target name/recession velocity ( $\text{km s}^{-1}$ ).

##### A.1.1. IES 1028+511/967

Paper 1 listed a column density of  $\log N_{\text{HI}} = 17.21_{-3.20}^{+0.22}$  for this absorber, but Table 3 lists  $b \approx 20 \text{ km s}^{-1}$  and  $\log N_{\text{HI}} \approx 14.3$ . The column densities formally overlap to within the quite large uncertainties listed in Paper 1 but our re-analysis finds that  $\log N_{\text{HI}} > 17$  requires  $b < 8 \text{ km s}^{-1}$ , which cannot be resolved using COS data with a velocity resolution of  $17 \text{ km s}^{-1}$ .

##### A.1.2. FBQS J1010+3003/1264 & 1380

Similar to the case above, Paper 1 lists  $\log N_{\text{HI}} = 17.79_{-3.48}^{+0.11}$  and Table 3 lists  $b \approx 30 \text{ km s}^{-1}$  and  $\log N_{\text{HI}} \approx 14.5$ . Here the  $\text{Ly}\alpha$  absorption is located near  $\text{Ly}\gamma$  absorption at  $z = 0.2546, 0.2549$  (Danforth et al. 2016) and whether a high-column-density solution is allowed is somewhat dependent on assumed component structure. We have adopted a two-component, low-column-density solution here, matching the fits of Danforth et al. (2016), as the lack of any metals associated with an absorber with  $\log N_{\text{HI}} \sim 18$  would be remarkable.

##### A.1.3. HE 0439–5254/1581, 1653, 1763 & 1805

This is another case where the assumed component structure matters. Paper 1 and Keeney et al. (2013) fit a total of two component in this region, with the strong one centered at  $1662 \text{ km s}^{-1}$  with  $\log N_{\text{HI}} = 14.36_{-0.07}^{+0.13}$ . Here we fit a total of four components, with one BLA to account for the very red wing at  $\lambda > 1223.2 \text{ \AA}$  and a weak metal-free component at  $1581 \text{ km s}^{-1}$ . This allows for a narrower, higher column density component at  $1653 \text{ km s}^{-1}$  than found in Paper 1, which is preferred by the photo-ionization model in Section A.3.1.

##### A.1.4. PG 0832+251/5221, 5337, 5396 & 5444

This system shows extremely broad, saturated  $\text{Ly}\alpha$  absorption with asymmetric wings, suggesting multiple velocity components. In Paper 1 we fit this profile with two components at  $5227$  and  $5425 \text{ km s}^{-1}$ , the first of which had a column density of  $\log N_{\text{HI}} \approx 18.5$ . While a *FUSE* spectrum exists for this sight line that shows O VI absorption at  $\sim 5221 \text{ km s}^{-1}$ , its S/N is quite low and cannot help constrain the H I component structure. Here we are basing our component structure on the metal-line velocity components,

which show four consistent components in low-ionization species. We adopt these component velocities for H I and hold them fixed while fitting the  $\text{Ly}\alpha$  profile. Unfortunately, the  $\text{Ly}\alpha$  profile is completely saturated for the two interior components so we are unable to constrain their Voigt profile parameters with any confidence. The outermost components can be constrained by the blue and red wings of the  $\text{Ly}\alpha$  profile, but the parameters for the  $5441 \text{ km s}^{-1}$  component are still quite uncertain. The specified  $\text{Ly}\alpha$  parameters are consistent with the low S/N  $\text{Ly}\beta$  detection in the *FUSE* data.

##### A.1.5. PMN J1103–2329/1113 & 1194

Paper 1 fits this profile with a single velocity component but we use two to better fit the blue wing of the profile. The column densities of the  $1194 \text{ km s}^{-1}$  component are consistent to within uncertainties regardless of which component structure is adopted.

##### A.1.6. RX J0439.6–5311/1638, 1674 & 1734

Paper 1 (and Keeney et al. 2013) fit this profile with a single  $\text{Ly}\alpha$  component at  $1672 \text{ km s}^{-1}$ , while we fit it here with multiple components, including one BLA, to better fit asymmetries in the wings of the  $\text{Ly}\alpha$  line profile. These components are heavily blended so the inferred Voigt profile parameters are quite uncertain. As with the HE 0439–5254 absorption system at similar velocity (Section A.1.3), the higher column density afforded by the multi-component fit is preferred by the photo-ionization models of Section A.3.5.

##### A.1.7. SBS 1108+560/654, 715 & 778

This sight line presents a unique challenge because a Lyman-limit system (LLS) at  $z = 0.4634$  dramatically reduces the observed flux at  $\lambda \lesssim 1340 \text{ \AA}$ . Above this cutoff, the spectrum exhibits quite high S/N, while below it the S/N is effectively zero in some regions. As with the PG 0832+251 system in Section A.1.4 we use the associated low-ionization metals to constrain the H I component structure, and attempt to fit the  $\text{Ly}\alpha$  profile holding these velocities fixed. However, the very poor S/N in this region of the spectrum, combined with the proximity to the Galactic DLA absorption at such low redshift, renders us unable to meaningfully constrain the H I column density for this absorber. In Paper 1 we did report H I column densities for two velocity components at  $665$  &  $778 \text{ km s}^{-1}$ , but our re-analysis cannot support those values.

##### A.1.8. SBS 1122+594/1221

The column density listed for this absorber in Paper 1 ( $\log N_{\text{HI}} = 17.71_{-2.85}^{+0.35}$ ) agrees with the value in Table 3 to within the large uncertainties. The higher column density does not fit the blue wing of the  $\text{Ly}\alpha$  profile as well as the lower column density does, but both are acceptable fits to the data.

##### A.1.9. VII Zw 244/715

As with the previous absorber, we report a lower column density than Paper 1, but both solutions are acceptable fits to the data. We prefer the lower column density solution in this case because it provides a better fit to the red wing of the  $\text{Ly}\alpha$  profile.

A.1.10. *3C 273/1019*

As discussed in [Savage et al. \(2014\)](#) and [Stocke et al. \(2014\)](#) this absorber includes a BLA and associated broad O VI absorption. [Stocke et al. \(2014\)](#) and [Yoon et al. \(2012\)](#) identify this absorber with a very rich foreground group on the southern outskirts of the Virgo Cluster.

A.1.11. *3C 273/1585*

This absorber was analyzed extensively by [Tripp et al. \(2002\)](#) and [Sembach et al. \(2001\)](#) based on STIS and FUSE spectroscopy, respectively. The H I fit in Table 3 finds a slightly higher  $b$ -value and lower column density than those of [Sembach et al. \(2001\)](#) and our metal-line values also differ slightly, owing primarily to the increased S/N of the COS spectrum we analyze. Detailed studies of the associated galaxy by [Stocke et al. \(2004\)](#) and [Keeney et al. \(2014\)](#) make a plausible case for the association of this absorber with a dwarf post-starburst galaxy in a galaxy filament near the Virgo Cluster, although ambient filament gas is also probably necessary to understand its detailed properties ([Keeney et al. 2014](#)). Gas at a comparable recession velocity was found in the nearby sight line Q 1230+0115; a discussion of the physical sizes of these absorbers can be found in [Rosenberg et al. \(2003\)](#). Single-phase, homogeneous photo-ionization models of this absorber by [Keeney et al. \(2014\)](#) differ only slightly from the original [Tripp et al. \(2002\)](#) model in being at slightly higher metallicity ( $\sim 15\%$  solar abundance) and larger size ( $\sim 130$  pc), primarily based on better upper limits on Si IV and C IV in the COS data. The photo-ionization models presented in Section A.3.10, which use an updated methodology, suggest a higher metallicity of  $35 \pm 10\%$  solar abundance and a line-of-sight cloud size of 50-100 pc, but given the systematic uncertainties in photo-ionization modeling the three models agree remarkably well.

A.1.12. *H 1821+643/36139, 36307, 36339, 36439, & 36631*

This absorption complex was analyzed by [Tripp et al. \(2001\)](#) who concluded that the higher redshift component contains a BLA and an associated broad O VI line that is almost certainly due to collisionally-ionized gas at  $\log T \approx 5.5$  (see also [Savage et al. 2014](#)). Our simultaneous fit to the Ly $\alpha$  and Ly $\beta$  profiles suggests that there are three blended components (two BLAs) with velocities of 36307, 36339, & 36439 km s $^{-1}$ . This three-component solution agrees with the fits of [Danforth et al. \(2016\)](#), although Paper 1 and [Savage et al. \(2014\)](#) only fit two components to this profile.

A.1.13. *PG 0953+414/42512, 42664, 42759 & 42907*

First studied by [Savage et al. \(2002\)](#) using rather low S/N STIS data, the COS spectrum obtained by the COS GTOs has much higher S/N ([Savage et al. 2014](#)). The new spectrum reveals a total of four components in Ly $\alpha$ , two of which align with rather strong O VI lines (see Figure 1 in [Savage et al. 2014](#)). [Savage et al. \(2014\)](#) find that the Ly $\alpha$ + O VI absorbers are consistent with cool, photo-ionized gas. In this compilation we identify two independent H I systems, each associated with O VI absorption (see Table 3).

A.1.14. *PG 1116+215/17614, 17676, 17786 & 18202*

This system was most recently studied by [Savage et al. \(2014\)](#) who found three H I components in Ly $\alpha$  and two O VI absorbers, one of which aligns well with one of the H I components. The  $b$ -values of these lines suggests photo-ionized gas. According to [Savage et al. \(2014\)](#) the other metal line absorptions (C IV and O VI) do not align well with the weak H I component allowing no firm conclusions to be drawn about the physical conditions of this gas. We also fit the Ly $\alpha$  with three components and find that, using our wavelength solution, the  $cz = 17786$  km s $^{-1}$  H I aligns reasonably well with the metal lines. Under the assumption that the H I and metal-line absorption arise in the same gas, the line widths suggest temperatures consistent with photo-ionized gas although these detections are weak enough that there is a considerable range in suggested temperatures.

A.1.15. *PG 1116+215/41522 & 41522*

This absorber has been studied extensively in [Danforth et al. \(2010\)](#), [Savage et al. \(2014\)](#) and [Stocke et al. \(2014\)](#). While all three papers suggest that a BLA is present which aligns well with the broad O VI absorption, [Savage et al. \(2014\)](#) fit the Ly $\alpha$  line with three components and find a significantly smaller  $b$ -value than the other analyses. This lower value suggests photo-ionized gas, while the BLA fit made by [Stocke et al. \(2014\)](#) found collisionally-ionized gas at  $T \approx 400,000$  K. Here we fit the H I lines with two components, consistent with the approach of [Stocke et al. \(2014\)](#). The two velocity components, one broad and one narrow, have best-fit velocities that are coincident (see Table 3).

A.1.16. *PG 1211+143/15170, 15321, 15357, 15431 & 15574*

This absorption was studied in detail using the STIS data by [Tumlinson et al. \(2005\)](#). This complex includes several velocity components which align well with the velocities of nearby galaxies in a rich group of galaxies. As shown in the plot of the 15321 km s $^{-1}$  absorber there is a very broad O VI absorption detected only in the weaker line of the doublet due to obscuring Galactic lines at this redshift. A BLA is almost certainly present in the highly saturated Ly $\alpha$  profile, which we and [Tumlinson et al. \(2005\)](#) fit as three components, only one of which has associated metals.

A.1.17. *PG 1211+143/19305, 19424, 19481 & 19557*

This absorption complex was also studied in detail by [Tumlinson et al. \(2005\)](#) and it also contains a very strong, very broad O VI line. [Tumlinson et al. \(2005\)](#) decomposed this complex into four components, including a BLA, but our simultaneous fit to all available H I lines from STIS and FUSE do not require a BLA (although at least one of the components has  $b > 35$  km s $^{-1}$ ). In this case these absorptions have only one nearby galaxy to which they are most likely associated, although the galaxy survey in this region is not exceptionally deep ( $M_r < -19.5$ ;  $L > 0.2 L^*$ ) since it is due entirely to the SDSS.

A.1.18. *PG 1216+069/37049, 37138, 37363 & 37455*

Paper 1 lists only one velocity component at 37091 km s $^{-1}$  for this sight line, but the COS spectrum clearly shows two

components in Ly $\alpha$  and Ly $\beta$  near this velocity as well as two more components  $\sim 300 \text{ km s}^{-1}$  redward, all of which have associated metals.

A.1.19. *PG 1259+593/13825, 13914 & 14014*

Both of these absorbers contain strong O VI absorption which [Savage et al. \(2002\)](#) and [Savage et al. \(2014\)](#) find to be consistent with photo-ionization. A third component at  $14014 \text{ km s}^{-1}$  is clearly present in the COS data but was not listed in Paper 1.

A.1.20. *PHL 1811/24226*

This absorber is the strong LLS studied in detail by [Jenkins et al. \(2003\)](#), who also presented a detailed discussion of the luminous, early-type associated galaxy. [Savage et al. \(2014\)](#) deconvolved a BLA from the highly-saturated Ly $\alpha$  absorption that corresponds to a very broad O VI line, yielding an approximate temperature of 300,000 K in collisionally-ionized gas. We fit only a single velocity component to the Ly $\alpha$  profile and find no strong evidence for associated O VI absorption, differing from the [Savage et al. \(2014\)](#) analysis. However, line blending in the *FUSE* data preclude an entirely consistent H I solution that satisfies the constraints of all of the lines, so the detailed component structure is less certain for this absorber than for other absorbers with comparable data. Nonetheless, the AGN continuum in the *FUSE* data is completely absorbed shortward of the Lyman limit at  $cz = 24226 \text{ km s}^{-1}$ , implying that the total H I column among all components is  $> 10^{17.9} \text{ cm}^{-2}$ , consistent with our best-fit value of  $\log N_{\text{HI}} = 18.08 \pm 0.04$ .

A.1.21. *PHL 1811/39658 & 39795*

The absorption tabulated here has a strong, aligned H I + O VI absorber whose  $b$ -values suggest cool, photo-ionized gas ([Savage et al. 2014](#)). But [Savage et al. \(2014\)](#) also find another three O VI velocity components, one of which (shifted by  $\sim 270 \text{ km s}^{-1}$  relative to the strong, photo-ionized absorber) lacks detectable Ly $\alpha$  absorption, implying a very hot, collisionally-ionized plasma at  $\log T > 5.7$  ([Stocke et al. 2014](#)). We fit a total of three O VI components and confirm the lack of H I associated with the redmost component centered at  $39930 \text{ km s}^{-1}$ .

A.1.22. *PHL 1811/52914 & 52933*

This absorber was found by [Savage et al. \(2014\)](#) to have two Ly $\alpha$  velocity components, neither of which align with an observed O VI absorber. [Stocke et al. \(2014\)](#) reanalyzed this spectrum and found that, while Ly $\alpha$  absorption exists at the O VI velocity (see Figure 4), the inferred  $b$ -values of H I and O VI suggest cool, photo-ionized gas.

A.1.23. *PKS 0405–123/28947 & 28958*

[Savage et al. \(2014\)](#) fit the Ly $\alpha$  absorption with a two-component model, one narrow and one BLA, which we adopt here. Weak O VI found at this velocity in the *FUSE* spectrum can be either cool, photo-ionized gas or warm, collisionally-ionized gas since the velocity separation of the two Ly $\alpha$  components is comparable to the uncertainties in registering the *FUSE* data to the COS data (see also [Stocke et al. 2014](#)).

A.1.24. *PKS 0405–123/45617, 45783 & 45871*

Paper 1 lists only two velocity components for this system, but our simultaneous fit to the Ly $\alpha$  and Ly $\beta$  profiles suggests that there are three components total. The bluer system from Paper 1 is now comprised of two weak, blended components.

A.1.25. *PKS 0405–123/49910, 49946, 50001, 50059, 50104 & 50158*

The very well-known, strong LLS absorber at  $50104 \text{ km s}^{-1}$  was first studied in [Chen & Prochaska \(2000\)](#) and [Prochaska et al. \(2004\)](#), and the much higher S/N COS spectrum is described in detail in [Savage et al. \(2010\)](#). The latter authors fit this absorption complex with multiple components, several of which contain broad O VI ([Tripp et al. 2008](#); [Thom et al. 2008](#)) at temperatures consistent with collisionally-ionized gas. At  $\approx -280 \text{ km s}^{-1}$  relative to the LLS is an O VI-only system with no associated H I absorption requiring a very hot temperature ( $\log T > 6.1$ ; [Savage et al. 2010](#)). The decrement at the Lyman limit in the *FUSE* spectrum of this absorber suggests a total H I column among all velocity components of  $\log N_{\text{HI}} = 16.63 \pm 0.02$ , which is consistent with the total H I column ( $\log N_{\text{HI}} = 16.49 \pm 0.21$ ) found by the Voigt profile fits of [Savage et al. \(2014\)](#), which we adopt here.

A.1.26. *PKS 1302–102/12573, 12655 & 12703*

Again Paper 1 lists only two velocity components for this system but simultaneously fitting the Ly $\alpha$  and Ly $\beta$  profiles indicates that the redward component of Paper 1 contains two narrower, blended components.

A.1.27. *PKS 2155–304/16965, 17113 & 17340*

This absorption complex was first studied in detail by [Shull et al. \(1998\)](#) and [Shull, Tumlinson, & Giroux \(2003\)](#) using GHRS data. In the latter publication the O VI detection is discussed in the context of a possible O VIII detection using *Chandra* and *XMM*. Here we model this complex with two strong components and a much weaker third one. The O VI detection discussed by [Shull et al. \(2003\)](#) is redshifted relative to the  $cz = 17112 \text{ km s}^{-1}$  H I by  $\approx 45 \text{ km s}^{-1}$ .

A.1.28. *Q 1230+0115/23294 & 23404*

Paper 1 lists only one H I component at this velocity, but two are clearly present in the COS data.

## A.2. Galaxy Properties

In Sections A.2.1–A.2.10, the targeted galaxies are discussed in the order in which they appear in Table 6. Then the serendipitous galaxies are discussed in Sections A.2.11–A.2.45 in the order in which they appear in Table 7.

### A.2.1. UGC 5740

This dwarf spiral is observed at intermediate inclination and probed by both the 1ES 1028+511 and also the 1SAX J1032.3+5051 sight lines at impact parameters of 79–110 kpc ( $1.5\text{--}2.0 R_{\text{vir}}$ ). It is the only targeted galaxy other than ESO 157–49 to be probed by multiple sight lines or at  $\rho > R_{\text{vir}}$ . Its recession velocity of  $649 \pm 4 \text{ km s}^{-1}$  is derived



from H I 21-cm emission (Schneider et al. 1992) and its H $\alpha$  flux has been measured by Kennicutt et al. (2008), whose value we adopt. All distance-dependent quantities (e.g., luminosity, stellar mass, SFR) for this galaxy assume a distance of 18.5 Mpc (Tully 1988; Sorce et al. 2014) rather than the Hubble-flow distance. This galaxy was not detected by GALEX so we are unable to estimate its FUV SFR. See Section 7.2 for a discussion of the absorber associations for this and the following galaxy.

#### A.2.2. SDSS J103108.88+504708.7

This dwarf irregular galaxy is probed by the 1ES 1028+511 sight line at an impact parameter of 26 kpc ( $0.5 R_{\text{vir}}$ ). Its SDSS spectrum indicates it has a recession velocity of  $934 \pm 7 \text{ km s}^{-1}$  and shows weak H $\alpha$  emission, which is used to derive its H $\alpha$  SFR. The H $\alpha$  SFR is quoted as a lower limit because the aperture correction for this very low- $z$  galaxy is quite large (Iglesias-Páramo et al. 2013).

#### A.2.3. UGC 5478

This dwarf irregular galaxy is probed by the FBQS J1010+3003 sight line with an impact parameter of 57 kpc ( $0.7 R_{\text{vir}}$ ). Its recession velocity of  $1378 \pm 5 \text{ km s}^{-1}$  is derived from H I 21-cm emission (de Vaucouleurs et al. 1991). The H $\alpha$  SFR is derived from narrowband images and the internal extinction correction is calculated from the Balmer decrement. All distance-dependent quantities assume a distance of 23.4 Mpc (Tully 1988).

#### A.2.4. ESO 157–49

This edge-on spiral is probed by the HE 0435–5304, HE 0439–5254, and RX J0439.6–5311 sight lines at impact parameters of 74–172 kpc ( $0.8$ – $1.8 R_{\text{vir}}$ ) and was studied in detail by Keeney et al. (2013). Associated metal lines are found in the closer sight lines but only Ly $\alpha$  is detected toward HE 0435–5304. ATCA H I 21-cm emission maps with  $4 \text{ km s}^{-1}$  velocity resolution and H $\alpha$  images from the CTIO 0.9-m were used to study its H I morphology and H $\alpha$  SFR, respectively (see Keeney et al. 2013 for details). We adopt the HIPASS recession velocity of  $1673 \pm 7 \text{ km s}^{-1}$  (Meyer et al. 2004), and the metallicity is derived using the N2 index of Pettini & Pagel (2004). Since SDSS magnitudes are not available for this galaxy we estimate its  $g$ - and  $i$ -band magnitudes from the broadband ( $B$ ,  $R$ ,  $I$ ) magnitudes listed in the NASA Extragalactic Database (NED) using the photometric conversions of Jester et al. (2005). The galaxy’s stellar mass is then calculated from these derived values. All distance-dependent quantities for this galaxy assume a distance of  $23.9 \pm 0.2 \text{ Mpc}$  (Willick et al. 1997; Tully et al. 2009).

#### A.2.5. ESO 157–50

This galaxy, also an edge-on spiral, is located near ESO 157–49 on the sky but has a higher redshift and luminosity. It is probed by the HE 0439–5254 sight line at an impact parameter of 89 kpc ( $0.65 R_{\text{vir}}$ ) and was again studied by Keeney et al. (2013) using ATCA H I 21-cm maps and CTIO 0.9-m H $\alpha$  images. Its recession velocity of  $3874 \pm 12 \text{ km s}^{-1}$

is from HIPASS (Meyer et al. 2004), the galaxy metallicity is derived using the N2 index of Pettini & Pagel (2004), and the stellar mass is calculated from NED ( $B$ ,  $R$ ,  $I$ ) photometry converted to SDSS  $g$ - and  $i$ -band magnitudes using the relations of Jester et al. (2005).

#### A.2.6. NGC 2611

This nearly edge-on spiral is probed by the PG 0832+251 sight line at an impact parameter of 53 kpc ( $0.4 R_{\text{vir}}$ ). Its recession velocity of  $5226 \pm 11 \text{ km s}^{-1}$  is derived from H I 21-cm emission (Springob et al. 2005). The associated Ly $\alpha$  absorption profile in the COS data is exceptionally broad and saturated, easily a LLS, but without higher-order Ly-series lines we cannot deconvolve the precise H I columns associated with most of the velocity components present in the metal-line data (see Section A.1.4). The galaxy metallicity is derived from our high-resolution DIS spectrum, which shows significant H $\beta$  absorption that must be accounted for to accurately measure the H $\beta$  emission flux. As discussed in Section 7.2, this galaxy is actually a member of a small group of galaxies, one of which is considerably closer to the QSO sight line though it is also considerably fainter than NGC 2611.

#### A.2.7. NGC 3511

This galaxy is a nearly edge-on spiral that is probed by the PMN J1103–2329 sight line at an impact parameter of 97 kpc ( $0.64 R_{\text{vir}}$ ). Its recession velocity of  $1114 \pm 6 \text{ km s}^{-1}$  comes from HIPASS (Meyer et al. 2004), and H $\alpha$  images of this galaxy were obtained with the KPNO 2.1-m telescope. We calculate the stellar mass using SDSS  $g$ - and  $i$ -band magnitudes derived from NED  $B$ ,  $V$ ,  $R$ ,  $I$  photometry (Jester et al. 2005). All distance-dependent quantities for this galaxy assume a distance of 13.6 Mpc (median of 18 redshift-independent distances listed by NED).

As discussed in Section 7.2, the association of this absorber with NGC 3511 is unclear. While the recession velocity of NGC 3511 matches the lower of two velocity components in the absorber, the higher velocity component is a close match to the recession velocity of another group member, NGC 3513, which is also closer to the sight line. Notably, if this absorber were in our serendipitous sample we would associate it with NGC 3513 rather than NGC 3511. The sight line is, however, projected along the minor axis of the low-level starburst galaxy NGC 3511.

#### A.2.8. M 108

This intermediate inclination spiral is the highest luminosity galaxy in the targeted sample, with an H I 21-cm-derived recession velocity of  $696 \pm 1 \text{ km s}^{-1}$  (Springob et al. 2005). It is probed by the SBS 1108+560 sight line at an impact parameter of 22 kpc ( $0.14 R_{\text{vir}}$ ), which also makes it the closest probe of a galaxy’s CGM (in terms of virial radii) in either sample. Unfortunately, a LLS at  $z = 0.4634$  precludes us from analyzing the H I absorption in this system (see Section A.1.7). Furthermore, the galaxy’s large size on the sky prevent the use of our standard ground-based methods. SDSS pipeline photometry is not reliable for such large sources, so we convert the broadband ( $B$ ,  $V$ ,  $I$ ) magnitudes listed in NED

to SDSS  $g$ - and  $i$ -band values (Jester et al. 2005) to calculate the galaxy’s stellar mass. We do not have images with a large enough FOV to capture all of the galaxy’s  $H\alpha$  flux, so we adopt the value of Kennicutt et al. (2008). The galaxy metallicity in Table 6 is the average of individual measurements of several H II regions from SDSS and our own DIS spectroscopy. The FUV luminosity is from Rifatto, Longo, & Capaccioli (1995) and uncorrected for intrinsic extinction, and thus highly uncertain. All distance-dependent quantities for this galaxy assume a distance of 10.7 Mpc (median of 9 redshift-independent distances listed by NED).

#### A.2.9. IC 691

This dwarf irregular galaxy is probed by the SBS 1122+594 sight line at an impact parameter of 45 kpc ( $0.5 R_{\text{vir}}$ ) and was studied in detail by Keeney et al. (2006).  $H\alpha$  images of this galaxy come from the KPNO 2.1-m telescope, its recession velocity of  $1199 \pm 7 \text{ km s}^{-1}$  is derived from H I 21-cm emission (de Vaucouleurs et al. 1991), and its intrinsic extinction is estimated from its observed Balmer decrement as described in Calzetti (2001). GALEX photometry for this galaxy is from Hao et al. (2011), and all distance-dependent quantities assume a distance of 23.7 Mpc (Tully 1988).

#### A.2.10. UGC 4527

This low surface brightness dwarf galaxy is the faintest galaxy in either sample and is located only 7 kpc ( $0.15 R_{\text{vir}}$ ) from the VII Zw 244 sight line, making it the closest probe of a galaxy’s CGM (in terms of impact parameter, second closest in terms of virial radii) in either sample. Its recession velocity of  $721 \pm 6 \text{ km s}^{-1}$  is derived from H I 21-cm emission (Schneider et al. 1992), but the luminosity, halo mass, and stellar mass of this galaxy are very uncertain because there is insufficient optical photometry available in NED to reliably estimate its SDSS  $g$ - and  $i$ -band magnitudes. However, this galaxy is clearly forming stars as evidenced by its weak  $H\alpha$  and FUV emission.

#### A.2.11. SDSS J122815.96+014944.1

This star-forming dwarf is located 70 kpc ( $1.4 R_{\text{vir}}$ ) from the 3C 273 sight line. Its metallicity is derived from emission lines present in the SDSS spectrum, and its  $H\alpha$  SFR is derived from narrowband images.

#### A.2.12. SDSS J122950.57+020153.7

This dwarf post-starburst galaxy, located 81 kpc ( $1.5 R_{\text{vir}}$ ) from the 3C 273 sight line, was studied in detail by Stocke et al. (2004) and Keeney et al. (2014). We adopt the FUV SFR and metallicity of Keeney et al. (2014), who use SED modeling of the galaxy’s GALEX+SDSS photometry to estimate its metallicity due to the lack of any optical emission lines in low- or high-resolution optical spectra. The  $H\alpha$  SFR comes from narrowband imaging. Despite the large uncertainties, this galaxy has the lowest metallicity estimate of all galaxies in this sample. The absorber is at high  $|\Delta v|/v_{\text{esc}} > 5$ , contains metal absorption, and may have been ejected from this galaxy. Alternately, the absorber may be associated with

a large- scale structure or rich galaxy group in this vicinity (Rosenberg et al. 2003; Yoon et al. 2012; Stocke et al. 2014). The absorber association and “passive” nature of this galaxy are discussed further in Section 7.2.1.

#### A.2.13. Mrk 892

This galaxy was part of the “alternate” sample of Paper 1, and is probed by the 3C 351 sight line at an impact parameter of 173 kpc ( $1.8 R_{\text{vir}}$ ). Its  $H\alpha$  SFR and metallicity are derived from SDSS emission-line fluxes. The lenticular morphology and bright nucleus of this galaxy suggest that it may harbor an AGN, but SDSS classifies it as a star-forming galaxy using emission line diagnostics (Kewley et al. 2006), an interpretation which is supported by the galaxy’s strong GALEX FUV emission.

#### A.2.14. SDSS J182202.70+642138.8

This  $L^*$  galaxy is probed by the H 1821+643 sight line at an impact parameter of 157 kpc ( $0.8 R_{\text{vir}}$ ). Its recession velocity is adopted from Tripp et al. (1998) but the only optical spectrum we have in hand for this galaxy is from WIYN/HYDRA and does not cover the  $H\alpha$  emission line. Thus, we cannot directly measure the galaxy’s metallicity; we use the mass-metallicity relationship of Lee et al. (2006) to estimate it instead. We attempt to estimate the galaxy’s  $H\alpha$  SFR by bootstrapping from  $H\beta$  as follows: (1) we estimate the intrinsic extinction at  $H\alpha$  using the galaxy’s observed morphology and inclination angle ( $H\alpha$  attenuation  $\sim 1.2$ ); (2) we determine the Balmer decrement ( $\sim 3.2$  assuming an intrinsic value of 2.87; Calzetti 2001) that yields the same  $H\alpha$  attenuation as our morphological estimate; (3) we multiply the observed  $H\beta$  flux by this derived Balmer decrement to estimate the  $H\alpha$  flux that would have been present in the galaxy spectrum. Since this is a spectroscopic estimate we apply our usual aperture correction procedure (a factor of  $\sim 2.0$  in this case). A similar procedure is followed for several galaxies below for which we have optical spectra that cover  $H\beta$  but not  $H\alpha$ .

#### A.2.15. SDSS J000529.16+201335.9

This dwarf irregular galaxy is located 97 kpc ( $1.8 R_{\text{vir}}$ ) from the Mrk 335 sight line. Its recession velocity is derived from H I 21-cm emission maps (van Gorkom et al. 1996) and its long-slit optical spectrum shows weak  $H\alpha$  and marginal  $H\beta$  emission. We have estimated its metallicity using the observed emission line fluxes. The  $H\alpha$  SFR comes from narrowband imaging, but have not applied our usual intrinsic extinction correction due to the large uncertainties in the observed Balmer decrement and galaxy morphology; thus, the tabulated  $H\alpha$  SFR is highly uncertain.

#### A.2.16. NGC 6140

This intermediate-inclination galaxy was part of the “alternate” sample of Paper 1 and is probed by the Mrk 876 sight line at an impact parameter of 257 kpc ( $1.6 R_{\text{vir}}$ ). Its recession velocity of  $908 \pm 1 \text{ km s}^{-1}$  is derived from H I 21-cm emission (Springob et al. 2005), its stellar mass is calculated from NED ( $B, V, I$ ) photometry converted to SDSS  $g$ - and  $i$ -band magnitudes using the relations of Jester et al. (2005),

and all distance-dependent quantities for this galaxy assume a distance of 18.6 Mpc (Tully 1988). The galaxy metallicity is estimated from an APO/DIS spectrum taken on 2016 Mar 20 and the  $H\alpha$  SFR is taken from the  $H\alpha$  imaging of Sánchez-Gallego et al. (2012), who have corrected for [N II] contamination and internal extinction.

A.2.17. *SDSS J095638.90+411646.1*

This luminous spiral is located 438 kpc ( $1.7 R_{\text{vir}}$ ) from the PG 0953+414 sight line. Its  $H\alpha$  SFR and metallicity are derived from SDSS emission-line fluxes. The intrinsic extinction estimate derived from the face-on morphological correction predicts an  $H\alpha$  attenuation ( $\sim 1.3$ ) that is approximately half the value inferred from the observed Balmer decrement for this galaxy. If the large spread in  $\text{Ly}\alpha$  velocity components for the associated absorber are separate clouds, some components may be associated with another nearby galaxy (see Section 7.2).

A.2.18. *SDSS J111905.51+211733.0*

This galaxy is probed by the PG 1116+215 sight line at an impact parameter of 133 kpc ( $1.5 R_{\text{vir}}$ ). Its recession velocity is from Prochaska et al. (2011b), but the only optical spectrum we have for this galaxy is from WIYN/HYDRA and does not cover the  $H\alpha$  region. As in Section A.2.14, we bootstrap an  $H\alpha$  SFR estimate from the observed  $H\beta$  emission flux but cannot directly measure the galaxy's metallicity. We use the estimate of the galaxy metallicity using the mass-metallicity relation of Lee et al. (2006) instead. The four-component H I+O VI absorber near this galaxy has two components at  $|\Delta v|/v_{\text{esc}} > 5$  (see Section 7.2). Some or all of these absorptions may be associated instead with a galaxy group that includes this galaxy (Stocke et al. 2014).

A.2.19. *SDSS J111906.68+211828.7*

This intermediate-inclination galaxy is located 139 kpc ( $0.7 R_{\text{vir}}$ ) from the PG 1116+215 sight line. Its SDSS spectrum shows weak Balmer emission, from which its  $H\alpha$  SFR and metallicity are derived. The metallicity estimate uses the N2 index of Pettini & Pagel (2004) because no [O III] emission is observed. This galaxy has the highest metallicity estimate of all galaxies where such estimates are available, and a sSFR low enough to be classified as passive by the COS-Halos definition ( $< 10^{-11} \text{ yr}^{-1}$ ; Tumlinson et al. 2011). At least some of this absorption may be due to a galaxy group to which this galaxy belongs (Stocke et al. 2014).

A.2.20. *IC 3061*

This very low- $z$ , edge-on spiral is projected 138 kpc ( $1.1 R_{\text{vir}}$ ) from the quasar PG 1211+143. Its recession velocity of  $2136 \pm 1 \text{ km s}^{-1}$  is derived from H I 21-cm emission measurements (Springob et al. 2005) and its metallicity is derived from SDSS emission-line fluxes. All distance-dependent quantities for this galaxy assume a distance of 42.0 Mpc (median of 10 redshift-independent distances listed by NED). The FUV magnitude is from Rifatto et al. (1995) and its SFR calibration is highly uncertain. While another nearby Virgo Cluster galaxy has a closer velocity match with the absorber (see Table 2), the impact parameter to IC 3061 is quite small and the association is deemed secure.

A.2.21. *SDSS J121409.55+140420.9*

This intermediate-inclination spiral is probed by the PG 1211+143 sight line at an impact parameter of 137 kpc ( $0.8 R_{\text{vir}}$ ). Its  $H\alpha$  SFR and metallicity are derived from emission lines in the SDSS spectrum. Its  $H\alpha$  SFR is treated as uncertain, however, because emission line diagnostics (Kewley et al. 2006) indicate a significant AGN contribution.

A.2.22. *SDSS J121413.94+140330.4*

This galaxy is located 72 kpc ( $0.8 R_{\text{vir}}$ ) from the PG 1211+143 sight line and has no FUV photometry available. Its  $H\alpha$  SFR and metallicity are estimated from an APO/DIS spectrum taken on 2016 Feb 6.

A.2.23. *SDSS J121930.86+064334.4*

This starburst galaxy, probed by the PG 1216+069 sight line at an impact parameter of 505 kpc ( $1.8 R_{\text{vir}}$ ), is the most luminous galaxy ( $3.5 L^*$ ) in either sample and the galaxy probed at the largest impact parameter. Its  $H\alpha$  SFR and metallicity are derived from SDSS emission-line fluxes. Its  $H\alpha$  SFR is treated as uncertain, however, because its very broad emission lines indicate a strong AGN contribution.

A.2.24. *SDSS J121923.43+063819.7*

This galaxy is projected 93 kpc ( $0.6 R_{\text{vir}}$ ) from the quasar PG 1216+069. Its recession velocity is from Prochaska et al. (2011b), but the only optical spectrum in hand for this galaxy is from WIYN/HYDRA and does not cover the  $H\alpha$  region. As before, we bootstrap an  $H\alpha$  SFR estimate from the observed  $H\beta$  emission and estimate the galaxy metallicity using the relation of Tremonti et al. (2004).

A.2.25. *UGC 8146*

This edge-on dwarf spiral is probed by the PG 1259+593 sight line at an impact parameter of 114 kpc ( $1.5 R_{\text{vir}}$ ). Its recession velocity of  $668 \pm 1 \text{ km s}^{-1}$  is derived from H I 21-cm emission maps (Springob et al. 2005) and its metallicity is derived from SDSS emission-line fluxes. The  $H\alpha$  SFR is derived from narrowband images. All distance-dependent quantities assume a distance of 18.5 Mpc (median of 15 redshift-independent distances listed by NED).

A.2.26. *SDSS J130101.05+590007.1*

This intermediate-inclination spiral is projected 138 kpc ( $1.0 R_{\text{vir}}$ ) from the quasar PG 1259+593. The SDSS spectrum of this galaxy shows very weak  $H\alpha$  and  $H\beta$  emission, from which the  $H\alpha$  SFR and metallicity are derived. The metallicity uses the N2 index of Pettini & Pagel (2004) because no [O III] emission is observed. This galaxy has a sSFR low enough to be classified as passive by the COS-Halos definition ( $< 10^{-11} \text{ yr}^{-1}$ ; Tumlinson et al. 2011), but there is no compelling reason to doubt this association (see Section 7.2.1).

A.2.27. *SDSS J215456.65-091808.6*

This galaxy is probed by the PHL 1811 sight line at an impact parameter of 269 kpc ( $1.3 R_{\text{vir}}$ ). Its  $H\alpha$  SFR and metallicity are derived from SDSS emission-line fluxes. The  $H\alpha$  SFR is listed as a lower limit due to the large aperture correction for this galaxy.

A.2.28. *SDSS J215517.30–091752.0*

This galaxy was part of the “alternate” sample of Paper 1, and is probed by the PHL 1811 sight line at an impact parameter of 502 kpc ( $2.0 R_{\text{vir}}$ ). Its  $\text{H}\alpha$  SFR and metallicity are derived from SDSS emission-line fluxes. This galaxy has the largest stellar mass of any studied herein and a sSFR low enough to be classified as passive (Tumlinson et al. 2011). There are no other luminous galaxies close to the absorber in this field, so the association with this passive galaxy seems reasonable despite the large impact parameter (see Section 7.2.1).

A.2.29. *J215447.5–092254*

This galaxy is projected 309 kpc ( $1.3 R_{\text{vir}}$ ) from the PHL 1811 sight line, and was part of the “alternate” sample of Paper 1. We adopt the recession velocity of Prochaska et al. (2011b) but the  $\text{H}\alpha$  SFR and metallicity are derived from an AAT/AA $\Omega$  spectrum with uncertain flux calibration. We flag the  $\text{H}\alpha$  SFR as uncertain but not the metallicity as the O3N2 index relies on ratios of emission line fluxes in narrow spectral regions (specifically,  $[\text{O III}] \lambda 5007/\text{H}\beta$  and  $[\text{N II}] \lambda 6583/\text{H}\alpha$ ). The stellar mass was derived from SDSS  $g, r, i$  images obtained with the MOSAIC imager on the CTIO Blanco 4-m telescope.

A.2.30. *J215450.8–092235*

This galaxy is also part of the “alternate” sample of Paper 1, and is probed by the PHL 1811 sight line at an impact parameter of 237 kpc ( $2.0 R_{\text{vir}}$ ). Its recession velocity is adopted from Prochaska et al. (2011b) but its  $\text{H}\alpha$  SFR and metallicity are derived from an AAT/AA $\Omega$  spectrum as with the previous galaxy. Similarly, the galaxy’s stellar mass is derived from CTIO/MOSAIC imaging in the SDSS  $g, r, i$  bands. In addition to being at the limit of this survey ( $\rho = 2.0 R_{\text{vir}}$ ), this galaxy has the highest sSFR of any galaxy studied herein.

A.2.31. *2MASS J21545996–0922249*

This galaxy is projected 35 kpc ( $0.2 R_{\text{vir}}$ ) from the PHL 1811 sight line and its recession velocity of  $24223 \pm 45 \text{ km s}^{-1}$  is adopted from 6dF (Jones et al. 2005). An AAT/AA $\Omega$  spectrum is available for this galaxy but shows no emission lines, so we are unable to estimate its  $\text{H}\alpha$  SFR. Its stellar mass was derived from CTIO/MOSAIC imaging in the SDSS  $g, r, i$  bands, and its metallicity was estimated using the relation of Tremonti et al. (2004).

A.2.32. *J215506.5–092326*

This luminous starburst galaxy is probed by the PHL 1811 sight line at an impact parameter of 228 kpc ( $1.0 R_{\text{vir}}$ ) and has the highest  $\text{H}\alpha$  SFR of any galaxy in either sample. Its recession velocity is adopted from Prochaska et al. (2011b), its  $\text{H}\alpha$  SFR and metallicity are derived from an AAT/AA $\Omega$  spectrum and its stellar mass is determined using CTIO/MOSAIC  $g, r, i$  imaging.

A.2.33. *J215454.9–092331*

This starburst galaxy has the highest redshift and largest FUV SFR of any galaxy studied herein. It is located 354 kpc

( $1.7 R_{\text{vir}}$ ) from the PHL 1811 sight line and its recession velocity is adopted from Prochaska et al. (2011b). Its  $\text{H}\alpha$  SFR and metallicity are derived from an AAT/AA $\Omega$  spectrum and its stellar mass is measured from CTIO/MOSAIC  $g, r, i$  images.

A.2.34. *J031201.7–765517*

This galaxy is from the “alternate” sample of Paper 1, and is probed by the PKS 0312–770 sight line at an impact parameter of 239 kpc ( $1.9 R_{\text{vir}}$ ). Its recession velocity is from Prochaska et al. (2011b), but we have no optical spectroscopy in hand to estimate its  $\text{H}\alpha$  SFR or metallicity. Furthermore, its luminosity, halo mass, and stellar mass are highly uncertain because there is insufficient optical photometry available in NED to reliably estimate its SDSS  $g$ - and  $i$ -band magnitudes. Nevertheless, we use the relation of Lee et al. (2006) to estimate the galaxy metallicity from its ill-constrained stellar mass.

A.2.35. *J031158.5–764855*

This galaxy is also from the “alternate” sample of Paper 1 and is located 381 kpc ( $1.6 R_{\text{vir}}$ ) from the PKS 0312–770 sight line. Its recession velocity is from Prochaska et al. (2011b), but we have no optical spectrum available to measure its  $\text{H}\alpha$  SFR or metallicity. As with the previous galaxy, there is insufficient optical photometry available in NED to reliably estimate its luminosity, halo mass & stellar mass. We have estimated the galaxy metallicity using the relation of Tremonti et al. (2004).

A.2.36. *2MASX J04075411–1214493*

This  $L^*$  galaxy is probed by the PKS 0405–123 sight line at an impact parameter of 378 kpc ( $2.0 R_{\text{vir}}$ ). Its recession velocity of  $29050 \pm 3 \text{ km s}^{-1}$  is adopted from Johnson et al. (2013) and its stellar mass is derived from CTIO/MOSAIC imaging in the SDSS  $g, r, i$  bands. Its  $\text{H}\alpha$  SFR is bootstrapped from the  $\text{H}\beta$  flux as described in Section A.2.14 because no  $\text{H}\alpha$  coverage is available in our CTIO/HYDRA spectrum, and is listed as a lower limit due to the large intrinsic extinction correction for this galaxy. A low-resolution APO/DIS spectrum with no flux calibration taken on 2012 Sep 16 shows emission from  $\text{H}\alpha$  and  $[\text{N II}]$  but not  $\text{H}\beta$  and  $[\text{O III}]$ ; therefore, the galaxy’s metallicity is estimated using the N2 index calibration of Pettini & Pagel (2004). The lack of  $\text{H}\beta$  and  $[\text{O III}]$  emission lines in the APO spectrum is not surprising, however, since they are located in regions of greatly reduced sensitivity due to the instrumental dichroic. The next-nearest galaxy is physically closer to the sight line and a better match to the  $N_{\text{HI}}$ -weighted mean velocity of the two  $\text{Ly}\alpha$  components, making this association uncertain.

A.2.37. *J040743.9–121209*

This galaxy is projected 197 kpc ( $1.1 R_{\text{vir}}$ ) from the quasar PKS 0405–123. Its recession velocity of  $45989 \pm 3 \text{ km s}^{-1}$  is adopted from Johnson et al. (2013) and is  $\sim 270 \text{ km s}^{-1}$  larger than the value in Paper 1, which used the redshift reported by Chen et al. (2001). Its stellar mass is derived from CTIO/MOSAIC  $g, r, i$  images, and an APO/DIS spectrum taken on 2012 Sep 23 shows no optical emission lines. Thus,

we use the relation of Tremonti et al. (2004) to estimate the galaxy metallicity.

#### A.2.38. J040751.2–121137

This luminous, intermediate-inclination galaxy is responsible for the LLS in the PKS 0405–123 spectrum first studied by Chen & Prochaska (2000). It is projected 117 kpc ( $0.5 R_{\text{vir}}$ ) from the sight line, and we now adopt the galaxy redshift of Johnson et al. (2013) rather than the value from Chen & Mulchaey (2009) as in Paper 1. The galaxy’s stellar mass is estimated from CTIO/MOSAIC images in the SDSS  $g, r, i$  bands. The galaxy metallicity and  $H\alpha$  SFR are estimated from an APO/DIS spectrum obtained on 2016 Oct 29. The metallicity is derived using the N2 index of Pettini & Pagel (2004) because the  $H\beta$  and [O III] emission lines are affected by the instrumental dichroic (a low-S/N CTIO/HYDRA spectrum of this galaxy has no  $H\alpha$  coverage and no  $H\beta$  emission).

#### A.2.39. NGC 4939

This luminous, intermediate-inclination spiral is projected 261 kpc ( $1.0 R_{\text{vir}}$ ) from the quasar PKS 1302–102. Its recession velocity of  $3112 \pm 2 \text{ km s}^{-1}$  is derived from H I 21-cm emission maps (Springob et al. 2005). We calculate its stellar mass using NED ( $B, V, R, I$ ) photometry converted to SDSS  $g$ - and  $i$ -band magnitudes using the relations of Jester et al. (2005). All distance-dependent quantities assume a distance of 39.3 Mpc (median of 18 redshift-independent distances listed by NED). No FUV photometry or optical spectroscopy are available for this galaxy, but a catalog of  $H\alpha$  + [N II] fluxes for 250 H II regions in the galaxy is available in Tsvetanov & Petrosian (1995). To calculate the galaxy’s  $H\alpha$  SFR we have summed the fluxes from all of the individual H II regions and assumed that  $[\text{N II}]/H\alpha = 1/3$ . The galaxy metallicity is estimated using the relation of Tremonti et al. (2004).

#### A.2.40. 2MASX J13052026–1036311

This galaxy is probed by the PKS 1302–102 sight line at an impact parameter of 227 kpc ( $0.9 R_{\text{vir}}$ ). Its recession velocity of  $12755 \pm 45 \text{ km s}^{-1}$  is adopted from 6dF (Jones et al. 2005), but we have no optical spectra in hand from which to measure its  $H\alpha$  SFR or metallicity. Its stellar mass is estimated from the  $B, R$  photometry of Prochaska et al. (2011b) using the relations of Jester et al. (2005) to convert to SDSS  $g$ - and  $i$ -band magnitudes. The galaxy metallicity is estimated using the relation of Tremonti et al. (2004).

#### A.2.41. 2MASX J13052094–1034521

This massive galaxy is located 353 kpc ( $1.3 R_{\text{vir}}$ ) from the PKS 1302–102 sight line, and its recession velocity of  $28304 \pm 45 \text{ km s}^{-1}$  is adopted from 6dF (Jones et al. 2005). Unlike the previous galaxy, we do have an optical spectrum in hand, which shows no emission lines; thus we are unable to measure the galaxy’s metallicity (it is estimated using the relation of Tremonti et al. (2004)), but we are able to set a spectroscopic limit on the  $H\alpha$  SFR. We flag the  $H\alpha$  SFR limit as uncertain because we do not know if any  $H\alpha$  emission is present outside of the spectroscopic aperture.

The galaxy’s stellar mass is derived from  $B, R$  photometry (Prochaska et al. 2011b) converted to SDSS  $g, i$  magnitudes using the conversions of Jester et al. (2005), and its sSFR is low enough to be passive by the COS-Halos definition (Tumlinson et al. 2011), but there is no compelling reason to doubt this association (see Section 7.2.1).

#### A.2.42. 2MASX J21584077–3019271

This galaxy is probed by the PKS 2155–304 sight line at an impact parameter of 425 kpc ( $2.0 R_{\text{vir}}$ ). Its recession velocity of  $17005 \pm 31 \text{ km s}^{-1}$  is adopted from 6dF (Jones et al. 2005) but we have no additional optical spectrum from which to measure its  $H\alpha$  SFR or metallicity. Its stellar mass is calculated from  $B, R$  photometry (Prochaska et al. 2011b) converted to SDSS  $g, i$  magnitudes (Jester et al. 2005). The galaxy metallicity is estimated using the relation of Tremonti et al. (2004).

#### A.2.43. J215845.1–301637

This luminous galaxy is located 403 kpc ( $1.8 R_{\text{vir}}$ ) from the PKS 2155–304 sight line, and was part of the “alternate” sample of Paper 1. Its recession velocity is adopted from McLin (2003) and Yao et al. (2010), but we have no optical spectrum from which to measure its  $H\alpha$  SFR or metallicity. Further, its luminosity, halo mass, and stellar mass are highly uncertain because there is insufficient optical photometry in NED to reliably estimate its SDSS  $g$ - and  $i$ -band magnitudes. The galaxy metallicity is estimated using the relation of Tremonti et al. (2004).

#### A.2.44. CGCG 14–54

This dwarf irregular galaxy, located 70 kpc ( $1.4 R_{\text{vir}}$ ) from the Q 1230+0115 sight line, is from the “alternate” sample of Paper 1 and has the lowest stellar mass of any galaxy studied herein. Its recession velocity of  $1105 \pm 5 \text{ km s}^{-1}$  is derived from H I 21-cm emission, and its  $H\alpha$  SFR and metallicity are derived from SDSS emission-line fluxes. The  $H\alpha$  SFR is listed as a lower limit due to the large aperture correction for this galaxy. All distance-dependent quantities assume a distance of 9.6 Mpc (Karachentsev & Nasonova 2013). The associated absorber has  $|\Delta v|/v_{\text{esc}} > 10$  and no associated metals. We speculate that this absorber is not associated with a single galaxy (see also Rosenberg et al. 2003).

#### A.2.45. SDSS J123047.60+011518.6

This galaxy is probed by the Q 1230+0115 sight line at an impact parameter of 55 kpc ( $0.5 R_{\text{vir}}$ ). Its recession velocity of  $23327 \pm 18 \text{ km s}^{-1}$  is measured from a WIYN/HYDRA spectrum that does not cover the  $H\alpha$  region; this is  $\sim 200 \text{ km s}^{-1}$  bluer than the redshift quoted in Paper 1. The updated redshift aligns much more closely with the  $\text{Ly}\alpha$  absorption velocity and is derived from a high-quality emission line spectrum; the previous redshift was derived from a low-S/N spectrum contaminated by moonlight (McLin 2003) and is deemed spurious. As before when we lack  $H\alpha$  coverage, we bootstrap an  $H\alpha$  SFR estimate from the observed  $H\beta$  flux and estimate the galaxy metallicity using the relation of Lee et al. (2006).

### A.3. Photo-Ionization Models

Below, each modeled absorber is discussed in turn, with the model “grade” (A, B, C, D) assessing the quality of the absorption-line data and the CLOUDY constraints noted in brackets after each absorber identification (see Section 6 and Table 9).

#### A.3.1. HE 0439–5254/1653 [C]

With detections in only H I, C IV, Si III and Si IV, this targeted absorber (System 10 in Table 3) barely meets our threshold for CLOUDY modeling. Nonetheless, we find a single-phase solution consistent with all of the metal-line detections above, as well as the upper limits set by the non-detection of C II, N V, etc. Since our  $N_{\text{HI}}$  value is consistent with that of Paper 1 we find a very similar  $\log U$  value, but our updated model metallicity is somewhat lower (although still consistent with the Paper 1 value to within the uncertainties).

This is a rare case where our assumed prior effects the model’s preferred values. A pure maximum likelihood analysis that assumes no prior predicts  $\log U = -2.30^{+0.19}_{-0.18}$  and  $\log Z_{\text{abs}} = +0.16^{+0.44}_{-0.34}$  for this absorber. The ionization parameter preferred by the maximum likelihood analysis is close to the value in Table 9, so the effect of the prior is to (unsurprisingly) nudge the absorber metallicity toward the galaxy metallicity (see Table 6).

#### A.3.2. PG 0832+251/5221 [C]

This targeted absorber (System 14 in Table 3) has a plethora of metal-line detections, but has perhaps the most uncertain  $N_{\text{HI}}$  value of any tabulated in Table 9 (see Section A.1.4 for details). However, if its H I column is taken at face value then this is the strongest H I absorber that we attempt to model. Our updated model attempts to reproduce the metal-line ratios from the observed O I, C II, Si II, and Fe II detections, as well as the C I and Fe III upper limits; the region of highest posterior probability is mildly inconsistent with the C I upper limit. The contours for the Si III, Si IV, and C IV detections and the N V upper limit are also shown, but are not used to constrain the model. The C IV detection in particular is clearly inconsistent with the solution derived from the lower ions, exemplifying the multi-phase nature of this absorber. This updated model finds a similar ionization parameter but higher metallicity than the model of Paper 1.

#### A.3.3. PG 0832+251/5444 [—]

This absorber (System 17 in Table 3) was modeled in Paper 1 but we do not model it here. There are sufficient metal-line detections to attempt to model it, but the H I column is too uncertain because this velocity component is located in the trough of an extremely strong Ly $\alpha$  absorber (see Figure 4 and Section A.1.4).

#### A.3.4. PMN J1103–2329/1194 [C]

This targeted absorber (System 19 in Table 3) was detected in Si III, Si IV, C IV and N V, and has stringent upper limits on C II and Si II. We fit the Ly $\alpha$  profile with two

velocity components (see Section A.1.5) and find a considerably lower H I column density than in Paper 1; consequently, our updated CLOUDY model finds a similar ionization parameter but a much higher metallicity than the model of Paper 1. Our photo-ionization model cannot simultaneously reproduce the metal-line ratios for all of the detected ions, so it uses the Si III and Si IV detections (and C II and Si II limits) to constrain the model, ignoring the C IV and N V detections. This is another case where our imposed prior on absorber metallicity affects the model’s preferred values. A pure maximum likelihood analysis with no prior finds  $\log U = -2.27^{+0.14}_{-0.15}$  and  $\log Z_{\text{abs}} = +0.48^{+0.16}_{-0.15}$ .

#### A.3.5. RX J0439.6–5311/1674 [C]

As with the HE 0439–5254 absorber that probes the same targeted galaxy (Section A.3.1), this absorber (System 21 in Table 3) is detected only in Si III, Si IV and C IV, but has stringent limits on C II, Si II and N V. Our updated model assumes a similar  $N_{\text{HI}}$  value to that of Paper 1 and finds a comparable ionization parameter but a lower metallicity than the model of Paper 1, although all of the values overlap within uncertainties. All of this absorber’s metal-line detections and limits can be reproduced with this single-phase model.

#### A.3.6. SBS 1108+560/654 [—]

This absorber (System 23 in Table 3) was modeled in Paper 1 and has many metal-line detections, but a higher redshift LLS (see Section A.1.7 for details) reduces the continuum near Ly $\alpha$  for this absorber to such a degree that we cannot reliably constrain the H I column. Thus, we do not attempt to model this absorber here.

#### A.3.7. SBS 1108+560/778 [—]

This absorber (System 25 in Table 3) was modeled in Paper 1 but we do not do so here for the reasons elaborated in Section A.3.6 above.

#### A.3.8. SBS 1122+594/1221 [B]

We have higher confidence in H I column density for this absorber (System 26 in Table 3) than the values of the previous two targeted absorbers because of its relatively simple Ly $\alpha$  profile. It has associated metal-line detections in C II, C IV, Si II, and Si IV, and stringent limits in Si II and N V. The CLOUDY model simultaneously reproduces the metal-line ratios inferred from all of these species and finds very similar values for the ionization parameter and absorber metallicity as the model of Paper 1. This absorber has the largest line-of-sight thickness and second-largest cloud mass of all the targeted absorbers that we are able to model, which may be related to its associated galaxy being a dwarf starburst (Keeney et al. 2006).

#### A.3.9. VII Zw 244/715 [B]

This absorber (System 27 in Table 3) also has a relatively simple Ly $\alpha$  profile, with a correspondingly higher confidence in the H I column density as compared to other targeted absorbers. It is detected in C II, C IV, Si II, Si III and Si IV, and has a stringent N V upper limit. Our updated

CLOUDY model is able to simultaneously accommodate all of the metal-line constraints with a single-phase solution. We assume a considerably lower H I column than in Paper 1 and thus find subsequently higher values for the ionization parameter and absorber metallicity than previously.

#### A.3.10. 3C 273/1585 [A]

This serendipitous absorber (System 102 in Table 3) has been studied extensively by various groups (see Section A.1.11 for details) and has an unusual ionization pattern in that it is detected in several ions (C II, Si II and Si III) with low ionization potentials but not in any species with intermediate or high ionization potentials (e.g., C III, C IV, Si IV, N V, O VI). Our updated CLOUDY model accommodates all of the metal-line constraints with a single-phase solution, although the C III upper limit that we adopt from Tilton et al. (2012) is somewhat incompatible with the C II column density we measure in the COS spectrum. Since we assume a smaller H I column than either Paper 1 or Tripp et al. (2002) we find a larger metallicity than they do but our ionization parameter is similar to theirs.

#### A.3.11. PG 0953+414/42664 [B]

This serendipitous absorber (System 115 in Table 3) is one of only two absorbers with  $N_{\text{HI}} < 10^{14} \text{ cm}^{-2}$  that we attempt to model. It is detected in C III and C IV, which we use to constrain our model, as well as N V and O VI, which we don't. This absorber was not modeled in Paper 1 because Danforth & Shull (2008) only lists associated C III and O VI; the C IV and N V are only detectable in the COS spectrum (see Figure 4).

#### A.3.12. PG 1116+215/41522 [A]

This absorber (System 123 in Table 3) is detected in many metal ions. We use the C II, Si II and Si III detections to constrain the model, along with the limits on O I and Fe III. The higher-ionization metal detections do not agree with the lower-ionization constraints, emphasizing the multi-phase nature of this absorber. We use a lower H I column than Paper 1 and find a somewhat higher ionization parameter and an entirely consistent absorber metallicity.

#### A.3.13. PG 1211+143/15321 [A]

This absorber (System 126 in Table 3) is also detected in many ions. We use the C II, Si II and Si III detections to constrain the model, but not the higher-ionization detections in C III, C IV, Si IV, N V, and O VI. We assume an H I column consistent with the value from Paper 1 and find consistent values of ionization parameter and metallicity for this multi-phase absorber.

#### A.3.14. PG 1211+143/19305 [B]

This absorber (System 130 in Table 3) is detected in Si III, C III, C IV, and O VI. We use all but the O VI to constrain our model and find a comparable ionization parameter and metallicity to Paper 1 using an H I column a bit larger than they assumed.

#### A.3.15. PG 1211+143/19481 [D]

This serendipitous absorber (System 132 in Table 3) has the lowest H I column of any we attempt to model here, and consequently the highest absorber metallicity. It is detected in only H I, C III and C IV, but our H I column is considerably smaller than the value assumed in Paper 1. This causes our ionization parameter and metallicity to differ more from the values in Paper 1 than any other absorber for which a comparison can be made. The poorly constrained values for H I column density and ionization parameter lead to this absorber being assigned grade D.

#### A.3.16. PG 1216+069/37049 [B]

This absorber (System 137 in Table 3) and the following were listed as a single system in Paper 1, where it was not modeled because Danforth & Shull (2008) list only Si II, C III and O VI at this redshift. The high-S/N COS spectrum (Figure 4) reveals that there are in fact two H I components here, along with another two  $\sim 300 \text{ km s}^{-1}$  redward, as well as metal-line absorption from Si III, Si IV, C IV, N V, and O VI. All of these species except for N V and O VI are used to constrain our model, along with C III from FUSE and stringent limits on C II and Si II.

#### A.3.17. PG 1216+069/37138 [B]

This absorber (System 138 in Table 3) was not modeled in Paper 1 for the reasons described in Section A.3.16. It is detected in the same ions as the absorber above and its model was constrained in the same way.

#### A.3.18. PG 1259+593/13825 [A]

This absorber (System 142 in Table 3) is detected in C III, C IV, Si III, Si IV, and O VI. All but the O VI are used to constrain our model, which assumes a nearly identical H I column as Paper 1 and predicts values for the ionization parameter and absorber metallicity that are consistent those of Paper 1, thanks to the rather large uncertainties quoted therein.

#### A.3.19. PG 1259+593/13914 [A]

This absorber (System 143 in Table 3) is detected in C III and C IV, which are used to constrain the model, and O VI, which is not. This model assumes a similar value of  $N_{\text{HI}}$  as Paper 1 and finds values of the ionization parameter and metallicity consistent with those quoted in Paper 1.

#### A.3.20. PHL 1811/22042 [—]

This absorber (System 148 in Table 3) was modeled in Paper 1 using Si III and Si IV column densities from Danforth & Shull (2008). The high-S/N COS spectrum (Figure 4) shows no indication of Si IV absorption, however, so we do not model this absorber here.

#### A.3.21. PHL 1811/23313 [A]

This absorber (System 149 in Table 3) has a peculiar ionization signature similar to the 3C 273 absorber we model in Section A.3.10 in so far as it is detected in Si II, Si III and C III but no higher-ionization species. Our updated model assumes a higher H I column than in Paper 1, and subsequently prefers a lower ionization parameter, but the two models find consistent metallicities.

A.3.22. *PHL 1811/24226 [C]*

This absorber (System 152 in Table 3) is detected in many metal species and has the largest  $N_{\text{HI}}$  value of any serendipitous absorber. It is also remarkable in its simple component structure for such a high column density system; all of the H I and metal-line detections have a single velocity component except for C IV, which has two. Our model finds evidence for a multi-phase absorber whose Si IV, C III and C IV detections do not match the solution preferred by the lower ions (detections in O I, C II, Si II, and Fe II, with a stringent limit on C I). We find a ionization parameter and metallicity values consistent with those of Paper 1.

A.3.23. *PHL 1811/39658 [D]*

This absorber (System 153 in Table 3) is detected only in C III and C IV, which we use to constrain our model, and O VI, which we don't. It was not modeled in Paper 1 because Danforth & Shull (2008) found only C III and O VI absorption at this redshift; the C IV only becomes apparent in the high-S/N COS spectrum (Figure 4). Due to its high ionization parameter and low metallicity this absorber has the largest line-of-sight thickness and mass of any absorber we attempt to model. However, due to its very weak metal-line detections and correspondingly large uncertainty in ionization parameter this model is grade D.

A.3.24. *PHL 1811/52933 [B]*

This absorber (System 157 in Table 3) is detected in C III, Si III and Si IV, and has stringent limits on C II, Si II, N V, and O VI. We find a single-phase solution that accommodates all of these constraints and is entirely consistent with the solution of Paper 1.

A.3.25. *PKS 0405–123/50059 [B]*

This absorber (System 170 in Table 3) was not modeled in Paper 1 because Danforth & Shull (2008) assumed a different component structure for this complex absorber than Savage et al. (2014). Our model assumes the Savage et al. (2014) values for H I and finds a multi-phase absorber whose C III and O VI detections are inconsistent with the solution that matches the C II, Si II and Si III detections.

A.3.26. *PKS 0405–123/50104 [B]*

This multi-phase absorber (System 171 in Table 3) is well-studied by several groups (see Section A.1.25 for details) and detected in many ions. As with the previous absorber, we adopt the H I component structure of Savage et al. (2014). Our model cannot simultaneously meet the constraints of the high- and low-ionization species, so we choose to model the low ion detections (C II, Si II, Si III, and Fe III). Our updated model finds a lower metallicity for this absorber than the value reported in Paper 1.

A.3.27. *PKS 1302–102/12655 [A]*

This is another multi-phase absorber (System 175 in Table 3) detected in many ions. Our model is entirely consistent with that of Paper 1 and uses the low- and intermediate-ionization detections (C II, C III, Si II, Si III) to constrain the model, but not the higher ionization species (C IV and O VI).

A.3.28. *PKS 1302–102/28439 [A]*

This is another absorber (System 178 in Table 3) seen mostly in low ions. In this regard it is similar to the 3C 273 absorber studied above (Section A.3.10) except that it does show O VI absorption, which we do not use to constrain the model. Our updated model simultaneously satisfies the constraints from C II, C III, Si II, and Si III detections, as well as limits from C IV, Si IV, O I, Fe III, and N V. Even though the updated absorber metallicity is higher than found in Paper 1, it is the lowest of any absorber we model here.

A.3.29. *Q 1230+011/23404 [C]*

Our updated model for this multi-phase absorber (System 187 in Table 3) is entirely consistent with the model of Paper 1, although we have less confidence in the H I column density than is the case for the typical serendipitous absorber. The Si III, Si IV and C III detections are used to constrain the model, along with the limits on Si II and C II, but not the higher-ionization detections of C IV and N V.

## B. GROUND-BASED GALAXY IMAGES

As discussed in Section 4, we endeavored to derive  $H\alpha$  SFRs from narrowband  $H\alpha$  images for all galaxies with recession velocities  $\leq 10000 \text{ km s}^{-1}$ , where spectroscopic aperture corrections are large and unreliable. All ten targeted galaxies are at these low redshifts, as well as eight of the serendipitous galaxies.  $H\alpha$  images were available in the literature for four of these galaxies: UGC 5470 (Kennicutt et al. 2008), M 108 (Kennicutt et al. 2008), NGC 6140 (Sánchez-Gallego et al. 2012), and NGC 4939 (Tsvetanov & Petrosian 1995). We obtained narrowband  $H\alpha$  images for 12 others, which are detailed in Table B1. Table B1 lists the following information by column: (1) galaxy name; (2) telescope where images were obtained; (3) instrument used to obtain images; (4) date of observation; (5) broadband and narrowband filters used for galaxy imaging; (6) exposure time per filter, in units of kiloseconds; and (7) the seeing in each filter, in units of arcseconds.

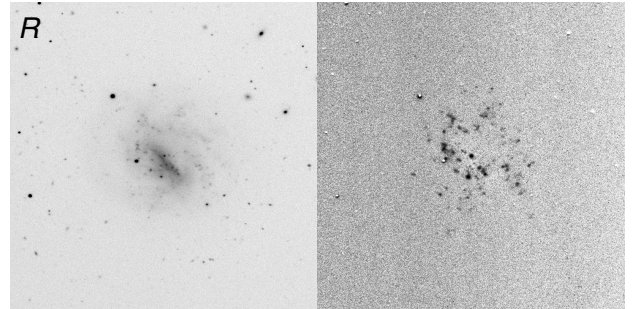


**Table B1.** Journal of H $\alpha$  Imaging Observations

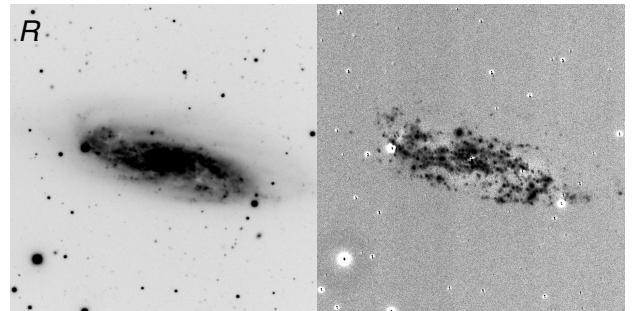
Galaxy	Telescope	Instrument	Date	Filters	Exposure (ksec)	Seeing (arcsec)
(1)	(2)	(3)	(4)	(5)	(6)	(7)
UGC 5478	KPNO 2.1-m	T2KA	2004 Apr 16	<i>B, R</i> , KP1563	0.6, 0.5, 2.4	0.9, 0.8, 1.0
ESO 157–49	CTIO 0.9-m	CFCCD	2003 Aug 22-23	<i>B, R</i> , 6600/75	3.0, 1.8, 9.0	2.3, 1.8, 1.5
ESO 157–50	CTIO 0.9-m	CFCCD	2003 Aug 24-25	<i>B, R</i> , 6649/75	1.8, 1.8, 10.8	2.8, 2.5, 1.6
NGC 2611	APO 3.5-m	SPIcam	2013 Mar 15	<i>r</i> , 645/10, 665/8	0.1, 2.7, 3.6	1.3, 1.3, 1.1
NGC 3511	KPNO 2.1-m	T2KA	2004 Apr 13	<i>B, R</i> , KP1563	0.6, 0.5, 2.4	2.0, 1.9, 2.0
IC 691	KPNO 2.1-m	T2KA	2003 Mar 4, 6	<i>B, R</i> , KP1565, KP1563	0.5, 1.7, 2.4, 2.4	1.5, 1.8, 1.5, 1.5
UGC 4527	KPNO 2.1-m	T2KA	2004 Apr 13-16	<i>B, R</i> , KP1563	0.9, 0.7, 2.4	1.1, 2.2, 1.6
SDSS J122815.96+014944.1	APO 3.5-m	SPIcam	2013 Mar 15	<i>r</i> , 657/8	0.1, 1.2	1.2, 1.2
SDSS J122950.57+020153.7	APO 3.5-m	SPIcam	2011 May 4	<i>R</i> , 661/8	1.8, 4.5	1.4, 1.2
SDSS J000529.16+201335.9	APO 3.5-m	ARCTIC	2016 Nov 1	<i>r</i> , 657/3, 660/3	0.1, 6.0, 6.0	0.9, 0.7, 0.6
IC 3061	APO 3.5-m	SPIcam	2009 Jan 20	645/10, 661/8	1.8, 2.4	2.2, 2.1
UGC 8146	APO 3.5-m	SPIcam	2008 Feb 2	645/10, 657/8	1.4, 1.8	1.0, 0.9

One complication that sometimes arises is a mismatch in seeing between the continuum image and the narrowband H $\alpha$  image. The narrowband image still contains some stellar continuum flux (i.e., it is not a pure emission-line image) that must be estimated from the off-band continuum image. We do this by scaling the sky level in the continuum image to match that of the narrowband image, then subtracting this scaled continuum image from the narrowband image to create a pure emission-line image, from which the galaxy’s H $\alpha$  SFR is derived. If the continuum image and the narrowband image have significantly different seeing (e.g., NGC 3511; see Figure B1), there will be residual artifacts in the emission-line image from point sources that are not cleanly subtracted due to mismatched point-spread functions. However, since the galaxies themselves are much larger on the sky than point sources at these very low redshifts, seeing differences do not have a significant effect on the estimated continuum flux distributions.

Figure B1 shows continuum and emission-line images for all galaxies listed in Table B1. These images are all oriented north-up, east-left, and have a field-of-view of  $25 \times 25$  kpc<sup>2</sup>, except for UGC 4527 and SDSS J122815.96+014944.1, which have a field-of-view of  $15 \times 15$  kpc<sup>2</sup>. The narrowband H $\alpha$  filters employed are all wide enough that the emission-line images (right-hand panels of Figure B1) include contributions from both H $\alpha$  and [N II]. We use optical spectra of the galaxy, where available, to estimate the contribution of [N II] to the emission-line image. These spectra cover the nuclear regions of the galaxy and do not allow us to account for any variations in H $\alpha$ /[N II] for other regions of the galaxy. If no galaxy spectrum is available, we use the procedure of Kennicutt et al. (2008) to statistically estimate the galaxy’s H $\alpha$ /[N II] ratio.



B1.1: Continuum and emission-line images for UGC 5478 (Section A.2.3).



B1.5: Continuum and emission-line images for NGC 3511 (Section A.2.7).

**Figure B1.** Continuum (left) and H $\alpha$  + [N II] (right) images of targeted and serendipitous galaxies. All images are oriented north-up, east-left and have a field-of-view of  $25 \times 25$  kpc<sup>2</sup> (except for UGC 4527 and SDSS J122815.96+014944.1, which have a field-of-view of  $15 \times 15$  kpc<sup>2</sup>). The name of the continuum filter for each galaxy is also labeled in the left-hand panel. Residual structure at the locations of point sources in the right-hand panel (e.g., white rings around black cores) are the result of seeing differences between the continuum and narrowband H $\alpha$  images. The complete figure set (12 images) is available in the online journal.

Some of our galaxies (e.g., NGC 2611) were observed through a narrow- or intermediate-width, off-band continuum filter that does not include any  $H\alpha$  + [N II] emission from the galaxy, while others (e.g., UGC 5478) used a broad off-band continuum filter that does include some contamination from the galaxy. Continuum subtraction in the former case is straightforward, but requires some care in the latter case; we use the procedure of Kennicutt et al. (2008) to statistically correct for any galaxy emission present in the continuum filter. The name of the off-band continuum filter used for each galaxy is labeled in that galaxy's continuum image (left-hand panel) in Figure B1.

The  $H\alpha$  SFR for the galaxy is derived from the emission-line images in Figure B1, corrected for [N II] emission in the narrowband filter as well as any  $H\alpha$  emission that is present in the continuum filter. The SFR is derived from the galaxy's

$H\alpha$  luminosity using the conversion of Hunter et al. (2010), and is listed in column 11 of Tables 6 and 7. The lower value in the tabulated SFR range is the value measured directly from the images, after correcting for Galactic foreground extinction, and the higher value employs a correction for internal extinction in the galaxy, as described in Section 4.

$H\alpha$  images for three of our galaxies have been previously published. The images for IC 691 were published in Keeney et al. (2006), and those for ESO 157–49 and ESO 157–50 were published in Keeney et al. (2013). We reproduce these images in Figure B1 for completeness but adopt the previously published SFR values, corrected to use the Hunter et al. (2010) SFR conversion when necessary for consistency with the rest of the sample.

### Fig. Set B1. Continuum and Emission-Line Images

## REFERENCES

- Adams, J. J., Uson, J. M., Hill, G. J., & MacQueen, P. J. 2011, *ApJ*, 728, 107
- Adelberger, K. L., Shapley, A. E., Steidel, C. C., et al. 2005, *ApJ*, 629, 636
- Aguirre, A., Schaye, J., Kim, T.-S., et al. 2004, *ApJ*, 602, 38
- Alam, S., Albareti, F. D., Allende Prieto, C., et al. 2015, *ApJS*, 219, 12
- Anderson, M. E. & Bregman, J. N. 2011, *ApJ*, 737, 22
- Armillotta, L., Werk, J. K., Prochaska, J. X., Fraternali, F., & Marinacci, F. 2016, *MNRAS*, submitted (arXiv:1608.05416)
- Asplund, M., Grevesse, N., Sauval, A. J., & Scott, P. 2009, *ARA&A*, 47, 481
- Binney, J. & Tremaine, S. *Galactic Dynamics* (Princeton: Princeton Univ. Press), pp. 567-575
- Bordoloi, R., Tumlinson, J., Werk, J. K., et al. 2014, *ApJ*, 796, 136
- Bouché, N., Hohensee, W., Vargas, R., et al. 2012, *MNRAS*, 426, 801
- Bowen, D. V., Chelouche, D., Jenkins, E. B., et al. 2016, *ApJ*, 826, 50
- Calzetti, D. 2001, *PASP*, 113, 1449
- Chen, H.-W. & Prochaska, J. X. 2000, *ApJ*, 543, L9
- Chen, H.-W., Lanzetta, K. M., Webb, J. K., & Barcons X. 2001, *ApJ*, 559, 654
- Chen, H.-W. & Mulchaey, J. S. 2009, *ApJ*, 701, 1219
- Chiappini, C., Matteucci, F. & Romano, D. 2001, *ApJ*, 554, 1044
- Chilingarian, I. V., Melchior, A.-L., & Zolotukhin, I. Y. 2010, *MNRAS*, 405, 1409
- Chilingarian, I. V. & Zolotukhin, I. Y. 2012, *MNRAS*, 419, 1727
- Chomiuk, L. & Povich, M. S. 2011, *AJ*, 142, 197
- Collins, J. A., Shull, J. M., & Giroux, M. L. 2004, *ApJ*, 605, 216
- Collins, J. A., Shull, J. M., & Giroux, M. L. 2009, *ApJ*, 705, 962
- Crighton, N. H. M., Morris, S. L., Bechtold, J., et al. 2010, *MNRAS*, 402, 1273
- Danforth, C. W. & Shull, J. M. 2005, *ApJ*, 625, 555
- Danforth, C. W. & Shull, J. M. 2008, *ApJ*, 679, 194
- Danforth, C. W., Keeney, B. A., Stocke, J. T., Shull, J. M., & Yao, Y. 2010, *ApJ*, 720, 976
- Danforth, C. W., Keeney, B. A., Tilton, E. M., et al. 2016, *ApJ*, 817, 111
- Davé, R., Oppenheimer, B. D., Katz, N., Kollmeier, J. A., & Weinberg, D. H. 2010, *MNRAS*, 408, 2051
- Davis, J. D., Keeney, B. A., Danforth, C. W., & Stocke, J. T. 2015, *ApJ*, 810, 92
- de Vaucouleurs, G., de Vaucouleurs, A., Corwin, H. G., Jr., et al. 1991, *Third Reference Catalogue of Bright Galaxies, Version 3.9*
- Diehl, R., Halloin, H., Kretschmer, K., et al. 2006, *Nature*, 439, 45
- Donahue, M., Aldering, G., & Stocke, J. T. 1995, *ApJ*, 450, L45
- D'Onghia, E. & Fox, A. J. 2016, *ARA&A*, 54, 363
- Driver, S. P., Popescu, C. C., Tuffs R. J., et al. 2008, *ApJL*, 678, L101
- Faerman, Y., Sternberg, A., & McKee, C. F. 2016, *ApJ*, submitted (arXiv:1602.00689)
- Faucher-Giguère, C.-A., Lidz, A., Zaldarriaga, M., & Hernquist, L. 2009, *ApJ*, 703, 1416
- Ferland, G. J., Korista, K. T., Verner, D. A., et al. 1998, *PASP*, 110, 761
- Fitzpatrick, E. L. 1999, *PASP*, 111, 63
- Fukugita, M., Shimasaku, K., & Ichikawa, T. 1995, *PASP*, 107, 945
- Fumagalli, M., Haardt, F., Theuns, T., et al. 2017, *MNRAS*, in press (arXiv:1702.04726)
- Garcia, A. M., Bottinelli, L., Garnier, R., Gouguenheim, L., & Paturel, G. 1992, *A&AS*, 96, 435
- Gaikwad, P., Srianand, R., Choudhury, T. R., & Khaire, V. 2016, *MNRAS*, submitted (arXiv:1610.06572)
- Giroux, M. L. & Shull, J. M. 1997, *AJ*, 113, 1505
- Green, J. C., Froning, C. S., Osterman, S. et al. 2012, *ApJ*, 744, 60
- Grevesse, N., Asplund, M., Sauval, A. J., & Scott, P. 2010, *Ap&SS*, 328, 179
- Gupta, A., Mathur, S., Krongold, Y., Nicastro, F., & Galeazzi, M. 2012, *ApJ*, 756, L8
- Haardt, F. & Madau, P. 1996, *ApJ*, 461, 20
- Haardt, F. & Madau, P. 2001, in *Clusters of Galaxies and the High Redshift Universe Observed in X-Rays*, ed. D. M. Neumann & J. T. V. Tran, 64
- Haardt, F. & Madau, P. 2005, unpublished spectra in 2005 August update to Haardt & Madau (2001) and included in the photo-ionization code CLOUDY
- Haardt, F. & Madau, P. 2012, *ApJ*, 746, 125
- Hao, C.-N., Kennicutt, R. C., Jr., Johnson, B. D., et al. 2011, *ApJ*, 741, 124
- Hinshaw, D., Larson, G., Komatsu, E., et al. 2013, *ApJS*, 208, 19
- Hunter, D. A., Elmegreen, B. G., & Ludka, B. C. 2010, *AJ*, 139, 447
- Iglesias-Páramo, J., Vílchez, J. M., Galbany, L., et al. 2013, *A&A*, 553, L7
- Jenkins, E. B., Bowen, D. V., Tripp, T. M., et al. 2003, *AJ*, 125, 2824
- Jester, S., Schneider, D. P., Richards, G. T., et al. 2005, *AJ*, 130, 873
- Johnson, S. D., Chen, H.-W., & Mulchaey, J. S. 2013, *MNRAS*, 434, 1765
- Jones, D. H., Saunders, W., Read, M., & Colless, M. 2005, *PASA*, 22, 277
- Karachentsev, I. D. & Nasonova, O. G. 2013, *MNRAS*, 429, 2677
- Keeney, B. A., Stocke, J. T., Rosenberg, J. L., Tumlinson, J., & York, D. G. 2006b, *AJ*, 132, 2496
- Keeney, B. A., Danforth, C. W., Stocke, J. T., France, K., & Green, J. C. 2012, *PASP*, 124, 830
- Keeney, B. A., Stocke, J. T., Rosenberg, J. L., et al. 2013, *ApJ*, 765, 27
- Keeney, B. A., Joeris, P., Stocke, J. T., Danforth, C. W., & Levesque, E. M. 2014, *AJ*, 148, 103
- Keeney, B. A., Stocke, J. T., Pratt, C., et al. 2017, in prep.
- Kennicutt, R. C., Jr., Lee, J. C., Funes, S. J. J. G., Sakai, S., & Akiyama, S. 2008, *ApJS*, 178, 247

- Kereš, D. & Hernquist, L. 2009, *ApJL*, 700, L1
- Kewley, L. J., Groves, B., Kauffmann, G., & Heckman, T. 2006, *MNRAS*, 372, 961
- Khaire, V. & Srianand, R. 2015, *MNRAS*, 451, L30
- Klypin, A., Kravtsov, A. V., Bullock, J. S. & Primack, J. R. 2001, *ApJ*, 554, 903
- Kollmeier, J. A., Weinberg, D. H., Oppenheimer, B. D., et al. 2014, *ApJ*, 789, L32
- Kriss, G. A. 2011, COS Instrument Science Report 2011-01(v1), Improved Medium Resolution Line Spread Functions for COS FUV Spectra (Baltimore: STScI)
- Larson, R. B. 1972, *MNRAS*, 157, 121
- Lee, H., Skillman, E. D., Cannon, J. M., et al. 2006, *ApJ*, 647, 970
- Lehner, N. & Howk, J. C. 2011, *Science*, 334, 955
- Lehner, N., Howk, J. C., & Wakker, B. P. 2015, *ApJ*, 804, 79
- Madau, P., Ferguson, H. C., Dickinson, M. E., et al. 1996, *MNRAS*, 283, 1388
- Madau, P. & Haardt, F. 2015, *ApJ*, 813, L8
- Martin, C. L., Dijkstra, M., Henry, A., et al. 2015, *ApJ*, 803, 6
- Masters, K. L., Nichol, R., Bamford, S., et al. 2010, *MNRAS*, 404, 792
- McGaugh, S. S., Schombert, J. M., Bothun, G. D., & de Blok, W. J. G. 2000, *ApJL*, 533, L99
- McLin, K. M. 2003, Ph.D. dissertation, Univ. of Colorado Boulder
- Meyer, M. J., Zwaan, M. A., Webster, R. L., et al. 2004, *MNRAS*, 350, 1195
- Montero-Dorta, A. D. & Prada, F. 2009, *MNRAS*, 399, 1106
- Moster, B. P., Naab, T. & White, S. D. M. 2013, *MNRAS*, 428, 3121
- Mulchaey, J. S. 2000, *ARA&A*, 38, 289
- Pachat, S., Narayanan, A., Muzahid, S., et al. 2016, *MNRAS*, 458, 733
- Peimbert, M., Luridiana, V., & Peimbert, A. 2007, *ApJ*, 666, 636
- Penton, S. V., Stocke, J. T., & Shull, J. M. 2004, *ApJS*, 152, 29
- Pettini, M. & Pagel, B. E. J. 2004, *MNRAS*, 348, L59
- Prochaska, J. X., Chen, H.-W., Howk, J. C., Weiner, B. J., & Mulchaey, J. 2004, *ApJ*, 617, 718
- Prochaska, J. X., Weiner, B., Chen, H.-W., Mulchaey, J., & Cooksey, K. 2011a, *ApJ*, 740, 91
- Prochaska, J. X., Weiner, B., Chen, H.-W., Cooksey, K., & Mulchaey, J. 2011b, *ApJS*, 193, 28
- Prochaska, J. X., Werk, J. K., Worseck, G., et al. 2017, *ApJ*, in press (arXiv:1702.02618)
- Robitaille, T. P. & Whitney, B. A. 2010, *ApJL*, 710, L11
- Rifatto, A., Longo, G., & Capaccioli, M. 1995, *A&AS*, 114, 527
- Rosenberg, J. L., Ganguly, R., Giroux, M. L., & Stocke, J. T. 2003, *ApJ*, 597, 677
- Rudie, G. C., Steidel, C. C., Shapley, A. E., & Pettini, M. 2013, *ApJ*, 769, 146
- Sánchez-Gallego, J. R., Knapen, J. H., Wilson, C. D., et al. 2012, *MNRAS*, 422, 3208
- Savage, B. D. & Sembach, K. R. 1991, *ApJ*, 379, 245
- Savage, B. D., Sembach, K. R., Tripp, T. M., & Richter, P. 2002, *ApJ*, 564, 631
- Savage, B. D., Narayanan, A., Wakker, B. P., et al. 2010, *ApJ*, 721, 960
- Savage, B. D., Kim, T.-S., Wakker, B. P., et al. 2014, *ApJS*, 212, 8
- Schaye, J., Aguirre, A., Kim, T.-S., et al. 2003, *ApJ*, 596, 768
- Schlafly, E. F. & Finkbeiner, D. P. 2011, *ApJ*, 737, 103
- Schneider, S. E., Thuan, T. X., Mangum, J. C., & Miller, J. 1992, *ApJS*, 81, 5
- Sembach, K. R., Savage, B. D., Lu, L., & Murphy, E. 1995, *ApJ*, 451, 616
- Sembach, K. R., Howk, J. C., Savage, B. D., Shull, J. M., & Oegerle, W. R. 2001, *ApJ*, 561, 573
- Sembach, K. R., Wakker, B. P., Savage, B. D., et al. 2003, *ApJS*, 146, 165
- Shull, J. M., Penton, S. V., Stocke, J. T., et al. 1998, *AJ*, 116, 2094
- Shull, J. M., Roberts, D., Giroux, M. L., Penton, S. V., & Fardal, M. A. 1999, *AJ*, 118, 1450
- Shull, J. M., Tumlinson, J., & Giroux, M. L. 2003, *ApJ*, 594, L107
- Shull, J. M., Jones, J. R., Danforth, C. W., & Collins, J. A. 2009, *ApJ*, 699, 754
- Shull, J. M., Stevans, M., Danforth, C., et al. 2011, *ApJ*, 739, 105
- Shull, J. M., Stevans, M. L., & Danforth, C. W. 2012, *ApJ*, 752, 162
- Shull, J. M. 2014, *ApJ*, 784, 142
- Shull, J. M., Moloney, J., Danforth, C. W., & Tilton, E. M. 2015, *ApJ*, 811, 3
- Simcoe, R. A., Sargent, W. L. W., & Rauch, M. 2004, *ApJ*, 606, 92
- Sorce, J. G., Tully, R. B., Courtois, H. M., et al. 2014, *MNRAS*, 444, 527
- Springob, C. M., Haynes, M. P., Giovanelli, R., & Kent, B. R. 2005, *ApJS*, 160, 149
- Steidel, C. C. 1995, in *QSO Absorption Lines*, ed. G. Meylan (Garching: Springer), 139
- Steidel, C. C., Adelberger, K. L., Giavalisco, M., Dickinson, M., & Pettini, M. 1999, *ApJ*, 519, 1
- Stern, J., Hennawi, J. F., Prochaska, J. X., & Werk, J. K. 2016, *ApJ*, 830, 87
- Stevans, M. L., Shull, J. M., Danforth, C. W., & Tilton, E. M. 2014, *ApJ*, 794, 75
- Stocke, J. T., Keeney, B. A., McLin, K. M., et al. 2004, *ApJ*, 609, 94
- Stocke, J. T., Penton, S. V., Danforth, C. W., et al. 2006, *ApJ*, 641, 217
- Stocke, J. T., Danforth, C. W., Shull, J. M., Penton, S. V., & Giroux, M. L. 2007, *ApJ*, 671, 146
- Stocke, J. T., Keeney, B. A., Danforth, C. W., et al. 2013, *ApJ*, 763, 148
- Stocke, J. T., Keeney, B. A., Danforth, C. W., et al. 2014, *ApJ*, 791, 128
- Taylor, E. N., Hopkins, A. M., Baldry, I. K., et al. 2011, *MNRAS*, 418, 1587
- Tepper-Garcia, T., Richter, P., Schaye, J., et al. 2012, *MNRAS*, 425, 1640
- Thom, C. & Chen, H.-W. 2008, *ApJS*, 179, 37
- Thom, C., Tumlinson, J., Werk, J. K., et al. 2012, *ApJ*, 758, L41
- Tilton, E. M., Danforth, C. W., Shull, J. M., & Ross, T. L. 2012, *ApJ*, 759, 112
- Tremonti, C. A., Heckman, T. M., Kauffmann, G., et al. 2004, *ApJ*, 613, 898
- Tripp, T. M., Lu, L., & Savage, B. D. 1998, *ApJ*, 508, 200
- Tripp, T. M., Giroux, M. L., Stocke, J. T., Tumlinson, J., & Oegerle, W. R. 2001, *ApJ*, 563, 724
- Tripp, T. M., Jenkins, E. B., Williger, G. M., et al. 2002, *ApJ*, 575, 697
- Tripp, T. M., Sembach, K. R., Bowen, D. V., et al. 2008, *ApJS*, 177, 39
- Tsvetanov, Z. I. & Petrosian, A. R. 1995, *ApJS*, 101, 287
- Tully, R. B., 1988, *Nearby Galaxies Catalog* (Cambridge: Cambridge)
- Tully, B. R., Rizzi, L., Shaya, E. J., et al. 2009, *AJ*, 138, 323
- Tumlinson, T., Shull, J. M., Giroux, M. L., Stocke, J. T. 2005, *ApJ*, 620, 95
- Tumlinson, J., Thom, C., Werk, J. K., et al. 2011, *Science*, 334, 948
- Tumlinson, J., Thom, C., Werk, J. K., et al. 2013, *ApJ*, 777, 59
- van Gorkom, J. H., Carilli, C. L., Stocke, J. T., Perlman, E. S., & Shull, J. M. 1996, *AJ*, 112, 1397
- Veilleux, S., Cecil, G., & Bland-Hawthorn, J. 2005, *ARA&A*, 43, 769
- Wakker, B. P., York, D. G., Howk, J. C., et al. 2007, *ApJ*, 670, L113
- Werk, J. K., Prochaska, J. X., Thom, C., et al. 2012, *ApJS*, 198, 3
- Werk, J. K., Prochaska, J. X., Thom, C., et al. 2013, *ApJS*, 204, 17
- Werk, J. K., Prochaska, J. X., Tumlinson, J., et al. 2014, *ApJ*, 792, 8
- Werk, J. K., Prochaska, J. X., Cantalupo, S., et al. 2016, *ApJ*, submitted (arXiv:1609.00012)
- Willick, J. A., Courteau, S., Faber, S. M., et al. 1997, *ApJS*, 109, 333
- Wolfe, A. M., Prochaska, J. X., & Gawiser, E. 2003a, *ApJ*, 593, 215
- Wolfe, A. M., Gawiser, E., & Prochaska, J. X. 2003b, *ApJ*, 593, 235
- Yao, Y., Wang, Q. D., Penton, S. V., et al. 2010, *ApJ*, 716, 1514
- Yoon, J. H., Putman, M. E., Thom, C., Chen, H.-W., & Bryan, G. L. 2012, *ApJ*, 754, 84
- Zahedy, F. S., Chen, H.-W., Rauch, M., Wilson, M. L., & Zabludoff, A. 2016, *MNRAS*, 458, 2423